Hydrography and flow in the axial valley of the Endeavour Segment: implications for larval dispersal

Irene Garcia Berdeal

A dissertation submitted in partial fulfillment of
the requirements for the degree of

Doctor of Philosophy

University of Washington

2006

Program Authorized to Offer Degree: Oceanography

University of Washington
Graduate School

This is to certify that I have examined this copy of a doctoral dissertation by

Irene Garcia Berdeal

and have found that it is complete and satisfactory in all respects,
and that any and all revisions required by the final
examining committee have been made.

Chair of the Supervisory Committee:

Susan L. Hautala

Reading Committee:

Susan L. Hautala

H. Paul Johnson

Eric Kunze

Date: 6/1/06

In presenting this dissertation in partial fulfillment of the requirements for the doctoral degree at the University of Washington, I agree that the Library shall make its copies freely available for inspection. I further agree that extensive copying of this dissertation is allowable only for scholarly purposes, consistent with "fair use" as prescribed in the U.S. Copyright Law. Requests for copying or reproduction of this dissertation may be referred to Proquest Information and Learning, 300 North Zeeb Road, Ann Arbor, MI 48106-1346, 1-800-521-0600, to whom the author has granted "the right to reproduce and sell (a) copies of the manuscript in microform and/or (b) printed copies of the manuscript made from microform."

Signature IRENE GARCÍA BERDEJA

Date 6/1/06

University of Washington

Abstract

Hydrography and flow in the axial valley of the Endeavour Segment: implications for larval dispersal

Irene Garcia Berdeal

Chair of the Supervisory Committee:
Associate Professor Susan L. Hautala
Oceanography

The axial valley of the Endeavour Segment (Juan de Fuca Ridge) is a region of intense hydrothermal activity that supports an exotic chemosynthetic ecosystem. Previous studies of circulation in the region have mostly focused on levels above the valley and near the rise height of high-temperature (>300°C) effluent from focused sources to obtain an integrated measure of heat and chemical fluxes into the deep ocean. However, it is thought that a large portion of hydrothermal heating is attributable to lower-temperature (5-50°C) buoyant fluid that emanates from diffuse hydrothermal sources and equilibrates at levels within the valley. Additionally, the largest concentrations of vent organisms and their larvae are found within the bottom meters of the axial valley.

The intent of this thesis is to characterize the flow and hydrography from the level of neutral buoyancy of the high temperature plumes, down through the axial valley and into the bottom boundary layer (BBL) and contribute to the understanding of transport processes that may be involved in the near-bottom dispersal of larvae or diffuse hydrothermal effluent. This is done primarily through analysis of several observational data sets consisting of point measurements of flow, temperature, and turbulent heat and momentum fluxes; timeseries of velocity profiles within the valley;

and high resolution cross/along valley sections of flow and hydrography that extend up to the level of neutral buoyancy.

Flow-topography interaction along with convective hydrothermal plumes yield a very dynamic environment. Within the BBL, currents are spatially heterogeneous and turbulence is generated by a combination of shear and buoyancy that depends on the phase of the tide and the relative distance from buoyancy sources. Above the BBL, within the valley, and at a site away from hydrothermal vents, subinertial flows are intensified and re-aligned along valley towards the bottom. This is consistent with solutions from a quasianalytic model for subinertial motions, which shows attenuation of cross-valley flow with depth. Beneath the level of neutral buoyancy, sections of hydrography and velocity reveal structures related to rising high-temperature plumes superposed on across and along valley density gradients that are thought to play a role in driving along-valley currents.

TABLE OF CONTENTS

LIST OF FIGURES

LIST OF TABLES

ACKNOWLEDGMENTS

This thesis has benefited from the time and effort of many individuals. At the risk of unintentionally leaving somebody out (for which I profusely apologize in advance) I would like to extend my heartfelt gratitude to all who contributed in some way or another. I would first and foremost like to thank my graduate advisor Susan Hautala, who has been a constant inspiration to me not only as a scientist but also as a person, and an absolute joy to work with. She offered me a magnificient opportunity to delve into the mysteries of the deep in the first place, but most importantly an opportunity to learn from and with her. I am thankful to my committee members Paul Johnson, Eric Kunze and Andrea Ogston, for their constant support, interest, suggestions and editing of this dissertation. Paul in particular, co-wrote with Susan the NSF grant that originally funded this research, and as chief-scientist of our research cruises, he always ensured that the graduate students obtained the data they needed for their theses, for which I am very grateful. I would also like to extend my gratitude to everyone in the School of Oceanography at the University of Washington, for their support and making my graduate experience wonderful. The following people contributed with ideas and discussions to this thesis: Matt Pruis, fellow graduate student with whom I shared long days calibrating instruments and who was a real pleasure to work with; Leif Thomas, who was incredibly helpful and supportive all along; and Bill Lavelle, who kindly provided a numerical model of buoyant plumes that aided in the interpretation of observations. I would also like to extend my gratitude to the entire science parties of the Thermal Grid 2000/2001 and LExEn 2002/2003 field programs at Juan de Fuca Ridge, the Woods Hole Deep Submergence Lab group and crews

of the *R/V Thompson* and *R/V Atlantis* for their hard work deploying instruments and collecting the data. Assistance with the instruments was provided by Sandy Williams, Tod Morrison and Dan Shaaf of Nobska and by RD Instruments. Finally, a word of recognition to all those who kindly make their software and algorithms publicly available thereby making our work a little (or a lot) easier, among them Rich Signell, Mike Foreman, Zhigang Xu, Rich Pawlowicz, the OSU tidal data inversion group, and a long etcetera. This research was funded by NSF grants OCE9911523 and OCE0318566, with supplementary funding from the University of Washington's Royalty Research Fund and the UW School of Oceanography.

Chapter 1

INTRODUCTION

Since their discovery some three decades ago, hydrothermal vent systems have attracted much interest and attention among scientists of various disciplines for their novel and startling biology, chemistry, and geology. Physical processes in the water column near hydrothermally active ridges are also quite unique and complex. Examples of such physical processes include flow-topography interactions (e.g. Allen and Thomson, 1993), internal tides (e.g. Lavelle et al., 2004), mixing (e.g Thurnherr et al., 2002), hydraulic flows (e.g. Thurnherr and Richards, 2001), and other phenomena directly related to the buoyant influx of hydrothermal vents such as convective plumes (e.g. Speer and Rona, 1989), entrainment (e.g. Lupton et al., 1985), plume vortices (e.g. Helfrich and Battisti, 1991), and basin-scale beta-plumes (e.g. Hautala and Riser, 1993). Knowledge of these processes can also be applied to important cross-disciplinary problems related to the transport of heat and chemical and biological species in the deep ocean.

Most existing studies of the circulation in the vicinity of hydrothermal vent systems have addressed flow on the regional- to basin-scale near the equilibration depth for high temperature hydrothermal effluent ($> 300^\circ$ C). At Endeavour Segment in the Juan de Fuca Ridge, the equilibrium plume is found above the axial valley, some 200 meters above the bottom. This dissertation examines the currents, hydrography, and physical processes in the bottom 300 meters over a 3-km long section of the axial valley that includes several active hydrothermal vent fields. Particular attention is given to levels within the axial valley and in the bottom boundary layer. These depth

ranges have been less explored, yet are important for several reasons. First, it is speculated that a significant fraction of the heat emitted from hydrothermal systems is attributable to low-temperature ($5 - 30^\circ$ C) effluent from diffuse sources that rises only to a few tens of meters off the bottom (which at the Endeavour Segment is in the confines of the axial valley). Therefore, characterizing the properties of these diffuse plumes requires observations in the proximity of the bottom. In addition, the seafloor surrounding hydrothermal vents is often the habitat of large abundances of vent organisms. The hydrodynamic environment in the near-bottom water column is likely to play a role in important aspects of the biology of these organisms such as the delivery of nutrients or chemicals, reproduction, or dispersal and retention of their larvae, which tend to be concentrated near the bottom. This dissertation is particularly concerned with improving our understanding of the physical constraints on near-bottom larval dispersal, although many of the results that will be presented are also applicable to the transport of heat, chemical species, and hydrothermal effluent in general.

This thesis is organized as follows. Chapter 2 is concerned with the flow and turbulence in the bottom boundary layer near diffuse vents. In Chapter 3, the vertical structure of currents within the axial valley is examined. Chapter 4 investigates the along- and across-valley structure of the currents and hydrography for levels at and beneath the equilibration depth. Chapter 5 concludes this thesis. Before delving into these specific topics, and to provide some background to the unfamiliar reader, a general overview on the geographic, geological and hydrodynamical settings for the study area is presented, and the problem of larval dispersal at hydrothermal vents is introduced.

1.1 Geographic and geological setting

Located 400-500 km off the coast of Oregon, Washington and British Columbia, lies a submarine mountain range, known as the Juan de Fuca Ridge. The ridge is 400

km long, has an orientation 20° east of north and is centered along the divergent boundary between the Pacific and Juan de Fuca plates (see Figure 2.1). As the plates spread apart at a intermediate rate (60 mm yr^{-1}), magma from the Earth's mantle flows upward to form new oceanic crust along the axial valley that splits much of the ridge crest. Cold (2° C) bottom ocean water percolates into the fractured crust where, in the process know as hydrothermal circulation, it is heated and chemically altered before venting out in the axial valley, much like hot springs or geysers on land.

The high temperature fluid, that can reach temperatures of 400° C, is loaded with particles, giving it an aspect of smoke (these vents are called "smokers"). As it exits the seafloor, some of the minerals within this hot effluent may precipitate in contact with the cold seawater, and form mineral deposits (appropriately called chimneys) that can reach several meters in height. Low temperature (5-30° C) effluent is thought to originate from subsurface mixing of hydrothermal fluid with ambient seawater. The clear warm shimmering effluent emanating through cracks and fissures in the rocks, porous sediments or mounds of tubeworms is referred to as diffuse venting (as opposed to the high temperature, focused fluid venting out of chimneys). Hydrothermal vents of one or more kinds are typically clustered in vent fields that range in size from tens to a couple of hundred meters in diameter.

The Juan de Fuca Ridge is broken into several nearly linear offset segments. The data used in this study were collected from the central section of the Endeavour Segment, at the northern end of the Juan de Fuca Ridge. Here, the 10 km wide ridge rises to 2100 m at its crest from a base depth of 2400 m, and the axial valley is ∼1 km wide and 100 m deep. The study area spans a 3.5 km section of the axial valley that comprises the vent fields of High Rise, Clam Bed, Raven, Main Endeavour Field, and Beach. Main Endeavour and High Rise are large fields, each containing multiple high-temperature hydrothermal vents. Raven (e.g. Johnson et al., 2002) and Clam Bed are smaller fields, each containing a single high-temperature vent and broad areas of diffuse flow. Beach is a primarily diffuse flow field, though several weakly venting

sulfide edifices are found in the area.

1.2 Hydrodynamic environment

1.2.1 High temperature and low temperature plumes

The hot fluid discharged from vents rises buoyantly and, as it does so, it entrains important volumes of background seawater and dilutes by factors of 10^4-10^5 (Lupton, 1995), thereby increasing its density. The mixture ascends to a level of neutral buoyancy, where it spreads laterally due to an unbalanced pressure gradient and background mean currents. In a quiescent flow, the rise height of a point-source plume scales as $z^* \sim B_o^{1/4}\ N^{-3/4}$, where B_o is the source buoyancy flux and N is the background buoyancy frequency, whereas in the presence of a background flow U, it is reduced if the velocity scale in the rising plume $(B_o N)^{1/4} < U$ (Speer and Marshall, 1995) in which case $z^* \sim (B_o/UN^2)^{1/3}$ (Turner, 1973).

At the Endeavour Segment a 200-m thick neutrally buoyant plume has been mapped centered at 150-200 mab (meters above the bottom) that is characterized by a temperature anomaly of up to 0.1° C and decreased light attenuation (Baker and Massoth, 1987; Thomson et al., 1990). In the absence of horizontal flows, the lateral spreading would be limited to the Rossby radius of deformation based on plume rise height $l = Nz^*/f$, where f is Coriolis parameter. For typical values at this site ($N = 10^{-3}$ s^{-1} and $f = 10^{-4}$ s^{-1}), $l = 1.5 - 2$ km. However, the prevailing current at the neutrally buoyant level generally advects the 1-2 km wide plume SSW along the ridge axis and it can be traced > 5 km downstream (Baker and Massoth, 1987; Thomson et al., 1990). This is quite a different situation from slow-rate spreading centers where the neutrally buoyant plume remains within the confines of the deep median axial valley as in the Mid Atlantic Ridge.

Low temperature hydrothermal fluid forms the so-called diffuse plumes that do not rise as high on account of the lower source buoyancy flux, which moreover makes them

more susceptible to background flows, according to the scaling argument presented above. Trivett and Williams (1994) observed diffuse plumes centered at 10-40 mab in the southern Juan de Fuca Ridge. Rona and Trivett (1992) obtained rise heights of diffuse plumes of 18-46 m using a numerical model designed to simulate buoyant plumes in a horizontal flow field with input parameters based on observations of diffuse vents at Axial Volcano, on the central Juan de Fuca Ridge.

1.2.2 Mean flows

Across the southern Juan de Fuca Ridge (south of Axial Volcano) Cannon and Pashinski (1990) observed plunging isopycnals on each side of the ridge and suggested an anticyclonic circulation above the ridge (northward along the west side and southward along the east side) that was later corroborated with current meter data (Cannon and Pashinski, 1997). In contrast, a hydrographic section across the northern Juan de Fuca Ridge suggested southward geostrophic flow on both sides of the ridge (Cannon and Pashinski, 1990) and, while only made over the ridge crest, direct observations have shown SSW flow with record-mean speeds of 1-5 cm s^{-1} (Thomson et al., 1990; Veirs et al., 1999).

In the axial valley, the record-averaged flows from current meters at the Main Endeavour field and Clam Bed are northward along the valley with a mean speed of 1-5 cm s^{-1} (Thomson et al., 2003). It has been suggested that this mean could be dynamically analogous to a pressure-driven sea-breeze circulation (Thomson et al., 2005).

1.2.3 Flow variability

In this region the current variability is dominated by tidal, inertial and low frequency (4-8 days) currents. This broad spectral band (a.k.a. "weather-band") has been associated with ridge-trapped subinertial waves generated by storm systems (Thomson et al., 1990; Cannon and Thomson, 1996; Allen and Thomson, 1993; Lavelle and

Cannon, 2001). Above the ridge near-inertial and semi-diurnal tidal currents are comparable in magnitude and are stronger than subinertial ("weather-band" and diurnal tidal) currents (Thomson et al., 1990; Allen and Thomson, 1993). Subinertial motions are trapped to the ridge and experience an amplification of their clockwise rotary component that Allen and Thomson (1993) attribute to the generation of anticyclonic vorticity by vortex squashing over the ridge. Within the axial valley, presumably too narrow to support rotary motion, inertial currents are dampened; diurnal tidal currents become weaker too, whereas semidiurnal tidal flows are less affected (Thomson et al., 1990). Below the ridge crest, components of current variability not only shift in relative amplitude but also become more rectilinear and parallel to the ridge axis in the valley (Thomson et al., 1990).

1.3 Larval dispersal at hydrothermal vents

Hydrothermal vents have been described as the oases of the deep ocean. Hot water rich in chemicals and minerals gushes or seeps through newly formed oceanic crust at vents and supports a rich and unique chemosynthetically-based ecosystem. Hydrothermal vents are short-lived, isolated, highly variable and unpredictable systems and vent species are faced with the challenge of being able to colonize new habitats as the old ones disappear, in order to maintain their populations through evolutionary time and become increasingly diverse. However, many vent organisms are sessile or have limited mobility so that dispersal is probably only possible during their larval stages. Larvae are typically poor swimmers and it is thought they rely heavily on the currents to transport them to new habitats. Among the vent species found in the Juan de Fuca Ridge is the abundant vestimentiferan worm *Ridgeia piscesae* (commonly called tubeworm), gastropods such as *Depressigyra globulus*, *Provanna variabilis* or the limpet *Lepetodrilus fucensis*, the clam *Calyptogena cf. pacifica* and the polychaetes *Paralvinella sulfincola* and *P. palmiformis*.

The ability of vent larvae to disperse depends, among other factors, on the life-span

of the larval stage (i.e., how long they remain viable in the plankton) and whether they have any swimming capabilities or can otherwise regulate their vertical position in the water column (by being buoyant, for example) so as to take advantage of the vertically-sheared flows in the region. Unfortunately, basic knowledge of vent species biology and ecology is limited due to the inherent difficulty in accessing hydrothermal ecosystems and their relative recent discovery. Only recently have scientists successfully grown embryos of a vent species in the lab under the conditions of temperature and pressure found at the ocean bottom (Marsh et al., 2001) and many inferences regarding the physiology and behavior of vent larvae still have to be made by comparison with their related shallow water taxonomic groups.

It is thought some vent species produce large numbers of planktotrophic larvae (that can feed in the water column), which makes them highly dispersive, yet it appears that most vent species produce fewer lecitotrophic larvae (non-feeding and surviving off their yolk sack) and some do not even have a larval stage but still manage to disperse from vent to vent (Mullineaux and France, 1995). While eggs are buoyant due to their high lipid content (and could potentially reach higher levels in the water column before they hatch), larvae are generally regarded as negatively buoyant, although lecitotrophic larvae could be buoyant at least during their early stages. This fact, coupled with the finding that these non-feeding larvae may undergo a developmental arrest (of about 38 days for the tubeworm *Riftia pachyptila*, Marsh et al. (2001)) by virtue of the low temperatures of the deep ocean, may increase their potential for dispersal.

Little is known about behaviors of vent larvae but, among larvae of shallow-water invertebrates, specific behaviors, for instance, to settlement cues upon approaching a suitable habitat, are common. Proposed cues range from chemicals to turbulence, while the responses induced involve swimming cessation and sinking by, for example, retracting a velum or dive-bombing (e.g. Finelli and Wethey, 2003; Hadfield and Koehl, 2004; Fuchs et al., 2004). What seems clear is that there probably is a variety

of larval physiologies and behaviors among vent species that, combined with physical constraints, result in different dispersal mechanisms.

1.3.1 Upper-level dispersal

The most commonly suggested pathway for larval dispersal is entrainment of larvae into the high temperature plume (Kim et al., 1994) where they can be transported upward to the neutrally buoyant level. Once there, they will be exposed to mean flows associated with the ridge as discussed in section 1.2.2, and can be advected distances of $\mathcal{O}$(100 km) (Marsh et al., 2001; Chevaldonne et al., 1997). But the neutrally buoyant plume is not only advected by the ambient flow; on account of rotation, the spreading plume acquires an anticyclonic circulation. Laboratory experiments have shown that this plume vortex becomes unstable when its radius is approximately one Rossby radius (l) and breaks up into vortex pairs that propagate away from the source region (Helfrich and Battisti, 1991). These eddies are long-lived, coherent structures that retain diluted hydrothermal fluid where larvae may reside for extended periods of time and be transported long distances. An extreme case of these vortices are "megaplumes", with diameters > 10 km and rise heights > 1000 m, that result from the discharge of large amounts of hydrothermal fluid during volcanic eruptions (Baker et al., 1989).

1.3.2 Lower-level dispersal

As suggested by Kim and Mullineaux (1998), entrainment into the high temperature plume may not be the dominant larval pathway except in periods of slack tides. Instead, transport in near-bottom currents (within 15 mab) is a more prevalent larval dispersal mechanism (occurring $> 74\%$ of the time, according to these authors) and can lead to high fluxes of biomass on account of the elevated concentrations of larvae closest to the bottom (Mullineaux et al., 2005). In addition, although larvae could potentially disperse over longer distances at upper levels, this path is also more risky

because of sustained intervals of cross-ridge flow that may transport the larvae off-axis (Marsh et al., 2001) and decrease their chance to colonize a new vent field. At the Juan de Fuca Ridge, near bottom currents are dominated by semidiurnal flows. The tidal excursion for a semidiurnal tidal flow of 5 cm s^{-1} is $\sim$350 m, which would not suffice to transport a larva in between vent fields at this location. In addition, a purely oscillatory, spatially uniform, tidal flow would not result in a net transport over a tidal cycle. Therefore mean flows, episodic events, and/or spatial variability are required for net displacement of larvae.

However, there are advantages to being lifted a few meters into the water column: first, to avoid topographic barriers to dispersal; and second, to access stronger horizontal flows. Negatively buoyant larvae lacking any swimming capability can take advantage of buoyant, rising plumes, or bottom turbulence to reach higher levels. Areas of diffuse flow can be quite extensive in the axial valley and generally provide a habitat for vent organisms whose larvae can be entrained in the diffuse plumes and rise a few tens of meters. The diffuse plumes themselves may be entrained in high temperature plumes and act as a link between lower and upper level dispersal.

Chapter 2

VARIABILITY OF CURRENTS AND TURBULENCE IN THE BOTTOM BOUNDARY LAYER OF THE AXIAL VALLEY

2.1 Introduction

Endeavour Segment is located in the northern end of the Juan de Fuca Ridge, approximately 500 km west of Vancouver Island, Canada. Here, the ridge is split at its summit by a 100-m deep, 1-km wide axial valley where several active hydrothermal vent fields can be found. This chapter presents measurements of flow, temperature and turbulence taken in the bottom meter of the axial valley, many of them at sites of diffuse hydrothermal venting. The study area covers a 3-km long section of the valley that includes two large vent fields (Main Endeavour and High Rise) and several smaller ones. Past observations of currents in this region have focused on depths above the crest of the ridge, where the hydrothermal fluid reaches its maximum height and spreads laterally, with less attention being paid to flows within the axial valley (Thomson et al., 1990; Allen and Thomson, 1993; Thomson et al., 2003).

Boundary layer currents have not been well documented at ridge axes, and to our knowledge, this field program was the first comprehensive attempt to not only measure vertical heat flux at diffuse hydrothermal vents (Pruis, 2004), but also to characterize flows in the near-bottom boundary layer at Endeavour Segment. Despite the previous lack of attention, the boundary layer is where a substantial amount of low-temperature diffuse hydrothermal fluid is being advected laterally, and where the largest abundances of larvae from vent organisms are found (Kim et al., 1994; Mullineaux et al., 2005). Therefore, characterizing the physical flow regime in the

near-bottom of the axial valley is fundamental in understanding the dispersion of larvae and diffuse hydrothermal vent fluid in such a dynamic and turbulent environment.

In some previous work at diffuse vents, concerned with the effect of currents on temperature, bottom water velocities have needed to be inferred from a model or taken from non-local current meter data (Little et al., 1988; Tivey et al., 2002). Flows in the boundary layer were measured directly by Trivett and Williams (1994) in the southern Juan de Fuca Ridge. For their investigation, bottom current measurements were taken downstream and at some distance from the diffuse vent to determine horizontal advective heat flux and entrainment into the diffuse plume.

For the present study, synchronous and co-located measurements of velocity and temperature were recorded within the bottom meter of the axial valley, both directly above and at some distance from diffuse vents. Long time-series measurements spanning 8-11 months and short time-series measurements of a few days at high temporal resolution were collected to characterize the low-frequency and turbulent flows in the near-bottom boundary layer. These data also allowed direct measurements of Reynolds stress and buoyancy production.

From the point of view of turbulent boundary layers, a hydrothermally active axial valley is a very unique environment, quite different from a typical deep oceanic boundary layer (e.g., Gross and Nowell (1985)) in that bottom roughness is quite large and thermal buoyancy contributes to the turbulent kinetic energy. It is also different from convective oceanic surface layers, such as observed under ice leads (McPhee and Stanton, 1996; McPhee, 1998), in that the source of buoyancy is hydrothermal heating instead of brine rejection or cooling. In this sense, the boundary layer observed over diffuse vents more closely resembles the boundary layer of the atmosphere heated from below, although modulated by tidal currents.

This chapter is organized as follows: Section 2.2 details the specifics of the data collection and processing; Sections 2.3 and 2.4 describe the temporal and spatial variability of near-bottom boundary layer flows, respectively; Section 2.5 describes

turbulent properties in the bottom boundary layer; Section 2.6 considers implications for the vertical and horizontal near-bottom transport of larvae; and Section 2.7 concludes the chapter.

2.2 Data collection and processing

Currents and water temperature were measured in the near-bottom boundary layer (< 1 meter above the bottom, abbreviated mab) at 33 sites in the axial valley of Endeavour Segment, in the northern Juan de Fuca Ridge (Figure 2.1). The study area is comprised of several active hydrothermal vent fields along a 3-km stretch of axial valley. Main Endeavour (Delaney et al., 1992) and High Rise (Robigou et al., 1993) are large fields, each containing multiple high-temperature hydrothermal vents. Raven (Johnson et al., 2002) and Clam Bed are smaller fields, each containing a single high-temperature vent and broad areas of diffuse flow. Beach is a primarily diffuse flow field, though several small sulfide edifices are found in the area. Most instruments were deployed at or nearby diffuse hydrothermal venting since a primary goal of the research program was to map and measure the diffuse heat flux in this portion of the axial valley (Pruis, 2004). Exceptions to near-vent locations are: CV, deployed in the middle of the valley, at some distance from vent fields; CB7 and MF5, deployed next to the elevators on which the instruments were lowered to the seafloor; HR3, deployed on a sediment patch nearby a black smoker; and CB5 and MF1, deployed in regions where the small temperature increase detected by the CTD on Jason was later traced back to a non-local source.

A total of 23 short-term records (2-9 days, except MF14 which is 29 days long) and 10 long-term records (180-324 days) were obtained in the years 2000-2003 (table 2.1), most of them as part of the Thermal Grid field program in 2000/01 (Johnson et al., 2002).

Water velocities were measured at 0.5 mab using the MAVS-3 (Nobska, Inc.), an acoustic three-axis differential travel-time current meter designed to measure bound-

Figure 2.1: Swath bathymetry map of the study area in the Endeavour Segment of the Juan de Fuca Ridge (adapted from Johnson et al. (2002)). Horizontal and vertical resolutions are 1.5 m and 0.1 m, respectively. Indicated on the map are the vent fields of High Rise (HR), Clam Bed (CB), Raven (R), Main Endeavour (MF) and Beach (B), as well as the locations where the MAVS where deployed in the year 2000 (in black), 2001 (in red), 2002 (in blue) and 2003 (in pink). Deployment names correspond to those listed in table 2.2. The colorbar shows the depth (m) and the axes are in Universal Transverse Mercator (UTM) coordinates (m). Inset shows location of Endeavour Segment on map.

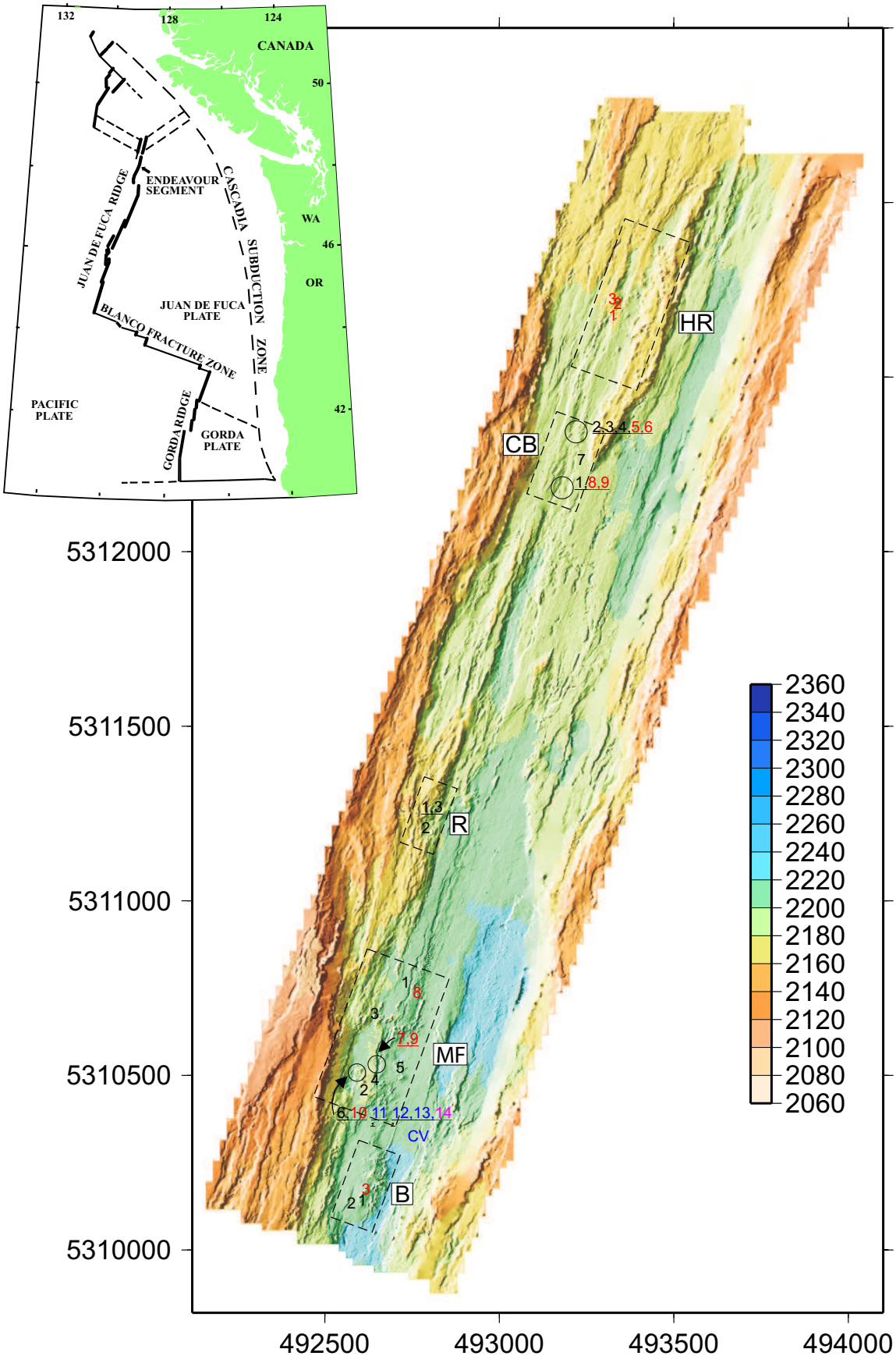
132
128
124
CANADA
50
ENDEAVOUR SEGMENT
JUAN DE FUCA RIDGE
CASCADIA SUBDUCTION ZONE
WA
46
OR
JUAN DE FUCA PLATE
BLANCO FRACTURE ZONE
PACIFIC PLATE
GORDA RIDGE
GORDA PLATE
42
HR
CB
R
MF
B
CV
5312000
5311500
5311000
5310500
5310000
492500
493000
493500
494000
2360
2340
2320
2300
2280
2260
2240
2220
2200
2180
2160
2140
2120
2100
2080
2060

Table 2.1: Deployment periods and locations of the MAVS in the Main Field (MF), Beach (B), Clambed (CB), High Rise (HR) and the central valley (CV). Start and end times are in year day and UTM coordinates and depth are in meters.

Depl.	Year	Start	End	Location	UTM X	UTM Y	Depth
MF1	2000	274.27	278.20	West Hulk	492718	5310773	2200
MF2	2000	274.56	278.32	Milli-Q,MEF	492600	5310466	2199
MF3	2000	274.59	278.24	Grotto,MEF	492630	5310684	2193
B1	2000	274.72	278.06	Beach	492594	5310149	2203
MF4	2000	274.87	282.14	S&M,MEF	492632	5310495	2194
MF5	2000	275.11	281.03	East MEF	492704	5310529	2214
MF6	2000/1	274.15	160.44	Easter Isl.	492573	5310525	2198
B2	2000/1	274.78	157.15	Beach	492564	5310142	2198
CB1	2000/1	279.36	171.65	Clam Bed	493162	5312185	2186
CB2	2000/1	279.72	164.38	Clam Bed	493231	5312326	2183
CB3	2000/1	279.85	165.22	Clam Bed	493229	5312356	2183
CB4	2000/1	279.86	166.15	Clam Bed	493213	5312356	2183
CB5	2001	172.86	177.07	Clam Bed	493212	5312345	2184
CB6	2001	172.92	177.08	Clam Bed	493193	5312330	2180
CB7	2001	173.04	182.22	Clam Bed	493223	5312272	2177
CB8	2001	173.14	175.95	Clam Bed	493163	5312198	2183
HR1	2001	173.36	179.14	High Rise	493313	5312685	2180
CB9	2001	173.59	179.50	Clam Bed	493175	5312183	2181
MF7	2001	174.01	180.22	S&M,MEF	492630	5310547	2192
MF8	2001	174.13	175.91	Hulk,MEF	492752	5310746	2198
B3	2001	174.40	180.12	Beach	492605	5310181	2198
R1	2001	174.63	180.77	Raven	492776	5311236	2179
R2	2001	174.93	180.42	Raven	492777	5311216	2184
HR2	2001	179.28	182.08	High Rise	493327	5312719	2167
HR3	2001	179.28	182.08	High Rise	493312	5312731	2168
MF9	2001/2	180.76	138.81	S&M,MEF	492637	5310538	2193
R3	2001/2	181.29	96.08	Raven	492788	5311236	2182
MF10	2001/2	181.55	44.30	Easter Isl.	492576	5310521	2194
CV	2002	260.54	263.58	Central Valley	492737	5310335	2192
MF11	2002	261.05	263.41	Easter Isl.	492576	5310521	2194
MF12	2002	261.40	263.37	Easter Isl.	492574	5310523	2193
MF13	2002/3	261.41	75.91	Easter Isl.	492576	5310524	2197
MF14	2003	194.30	223.25	Easter Isl.	492575	5310523	2198

ary layer currents in low-flow, deep-ocean benthic environments with few scatterers (Thwaites and Williams, 1996; Williams, 2002). Current meter accuracy is 0.3 cm/s and the resolution is 0.03 cm/s. The MAVS were equipped with a thermistor string that was attached near to the velocity sensor and measured temperature at the sea floor, 0.5 mab and 0.8 mab. Thermistors have a measurement range of -5 to 45 °C, an accuracy of 0.02°C and a resolution of 0.01°C. The MAVS-3 instrument was mounted on a PVC cilindrical stand with a bean bag base so it could be folded in during ascent/descent for protection and easily deployed on irregular terrain (for a schematic, see Pruis et al. (2006)).

Short-term deployments acquired data continuously at 2 Hz (5 Hz in 2002), except for MF5 that recorded in bursts of 180 samples every hour. In 2003, MF14 sampled at 2 Hz in 10-minute bursts every hour. Long-term deployments recorded in bursts of 180-320 samples every hour at 2 Hz. A zero-velocity laboratory calibration was conducted in still water prior and subsequent to the deployment of the MAVS. Zero-offset drifts upon the first exposure of the velocity sensors to salt water under high pressure were large, but remained relatively stable and small thereafter, with typical values of 0.3 cm/s (Williams, 2001). Velocity data were recorded in acoustic axes coordinates, flagged for outliers (> 8000 counts), corrected using post-deployment zero-offsets and rotated to Earth's coordinates using tilt and heading values. One of the long-term deployments (CB3) was recovered with abundant bacterial floc invading the space in between the sensor rings, which might have affected the velocity measurements. The instrument's orientation was visually estimated from the Jason gyrocompass since it was virtually impossible to account for the effects of nearby strongly magnetic rocks on the MAVS compass. Heading data was subsequently corrected where needed (table A.1 in the appendix). Calibration of the thermistors were conducted pre- and post-deployment using a well-stirred ice-bath that was progressively heated to 40°C. The calibrations were verified by examining self-consistency within the thermistor strings during descent and ascent of the deployment elevator. A 300-kHz ADCP was

deployed on the seafloor next to the MAVS at site CV to concurrently measure velocity every 4 m from 6.5 to 78.5 mab. The ADCP sampled continuously every 3 s for a total of 4.2 days.

Harmonic analysis was performed on short-term MAVS records using the Tidal Analysis Toolbox (Pawlowicz et al., 2002). A Butterworth filter with a cut-off frequency of 0.5 hr was applied to the records prior to the analysis except for MF5 and and MF14 that were simply burst-averaged. A total of eight (three fundamental and five "shallow water") tidal constituents were used in the fit, in accordance with the Rayleigh criterion. Confidence limits on ellipse parameters were calculated with a bootstrap method. Long-term data were burst-averaged before proceeding with further analysis. Spectral analysis was performed on the de-meaned time series of long-term records with frequency averaging (over 11-16 frequencies, depending on the length of the time series) to yield a bandwidth of $\sim 2 \times 10^{-3}$ cycles per hour (cph).

2.3 Temporal variability of the flow

In this region, current variability is dominated by tidal, inertial ($\sim$ 16 hours) and low frequency (3-8 days) currents. The latter broad spectral band (also called "weather band") has been associated with ridge-trapped subinertial waves generated by storm systems (Cannon and Thomson, 1996; Cannon et al., 1991). Above the ridge, near-inertial and semidiurnal tidal currents are comparable in magnitude and slightly stronger than diurnal currents (Thomson et al., 1990; Allen and Thomson, 1993). Subinertial motions are trapped to the ridge and experience an amplification of their clockwise rotary component (Allen and Thomson, 1993; Lavelle and Cannon, 2001). Near-inertial motions are also intensified immediately above the ridge crest, but are strongly damped within the valley (Thomson et al., 1990). Subinertial currents are attenuated and become more rectilinear in the valley with respect to those measured immediately above the ridge, while semidiurnal flows are less affected by the bathymetry (Thomson et al., 2003; Garcia Berdeal et al., 2006).

Flows measured in the near-bottom boundary layer of the axial valley show the general trends of current variability observed at other depths within the valley. As shown in the rotary spectra for the long-term record MF9 (figure 2.2), the dominant temporal variation is associated with the semidiurnal tide, followed by the 4-day spectral band and the diurnal tide. Although the record showcased (MF9) does have

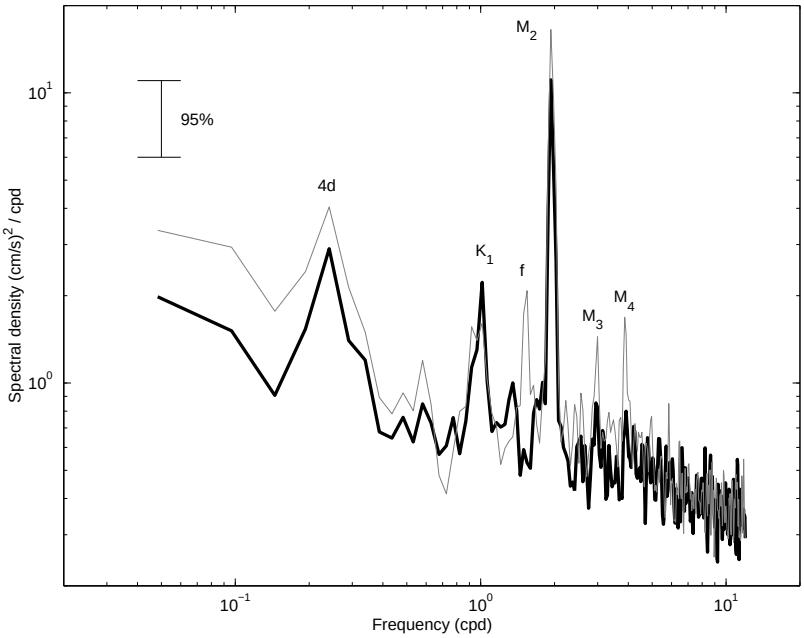

Figure 2.2: Rotary current spectra for 11-month deployment MF9. The thick (thin) line corresponds to the counterclockwise (clockwise) spectrum. Spectra shown were calculated by averaging together spectra from 20-day overlapping segments. The segments were previously detrended and a Hanning window was applied. Rotary components were calculated from the autospectra and quadrature spectra following Gonella (1972). 95% confidence interval is shown and significant peaks are labeled.

a significant peak at the inertial frequency, few other long-term records do (see table 2.2).

Table 2.2: Record-mean statistics and current ellipse parameters for the long-term MAVS deployments: record-mean speed and direction (dir); semimajor (M), semiminor (m) axes and inclination of the variance ellipse and the 4-day, K_1, inertial and M_2 current ellipses. Current ellipses at these frequencies were calculated from autospectra and co-spectra of the long-term velocity time-series, which were averaged over 11-16 frequencies (depending on length of time series) to yield a frequency resolution of $\sim 2 \times 10^{-3}$ cph. Velocities are measured in cm s^{-1} and direction in degrees clockwise from north. The minus sign in m indicates clockwise rotation. Significant values are shown in bold. CB3 was recovered with biological growth between the velocity sensor rings, that may have affected the flow measurements.

Deployment	Mean		Variance			4d			K_1			f			M_2		
	speed	dir	M	m	θ	M	m	θ	M	m	θ	M	m	θ	M	m	θ
CB1	0.8	279	1.3	0.8	264	**0.3**	**0.2**	**36**	**0.2**	**0.2**	**83**	0.2	0.1	87	**0.5**	**0.3**	**6**
CB2	0.8	258	2.2	0.8	240	**0.7**	**0.1**	**56**	**0.5**	**0.1**	**59**	0.4	-0.1	53	**1.6**	**-0.1**	**57**
CB3	0.4	81	1.1	0.7	260	**0.2**	**0.2**	**105**	**0.2**	**0.1**	**90**	0.2	-0.1	83	**0.4**	**-0.1**	**108**
CB4	1.8	262	2.2	1.1	16	**0.8**	**-0.2**	**12**	**0.5**	**0.2**	**10**	**0.4**	**0.2**	**19**	**1.5**	**0.2**	**14**
R3	3.1	248	1.5	1.0	21	**0.4**	**-0.1**	**20**	**0.4**	**0.1**	**24**	0.2	0.1	25	**0.9**	**0.2**	**19**
MF6	0.9	326	2.2	0.8	4	0.5	0.1	4	0.3	-0.1	5	0.3	0.1	15	**2.4**	**-0.5**	**8**
MF9	2.1	27	3.6	2.1	39	**1.3**	**-0.2**	**50**	**0.7**	**0.6**	**52**	**0.7**	**-0.4**	**34**	**2.7**	**-0.4**	**43**
MF10	1.2	65	2.7	1.0	42	**1.1**	**0.1**	**41**	**0.6**	**-0.1**	**44**	**0.5**	**-0.2**	**37**	**2.5**	**0.1**	**41**
MF13	0.9	136	2.2	0.9	254	**0.7**	**-0.2**	**68**	0.6	-0.2	66	0.3	-0.1	81	**1.7**	**-0.4**	**63**
B2	2.4	11	0.8	0.7	267	0.1	0.1	348	**0.2**	**0.1**	**62**	0.2	-0.1	106	**0.4**	**0.2**	**64**

Similar to other depths within the valley, current ellipses corresponding to significant spectral peaks in the bottom boundary layer are typically strongly polarized although they do not necessarily align with the axis of the valley, suggesting a strong topographic influence. A significant peak at twice the M_2 frequency (M_4) is not uncommon in the long-term records and probably arises from nonlinear interaction between waves of the fundamental frequency, similar to observations by Mihaly et al. (1998) at 350 mab of Endeavour Segment. A peak at the compound frequency fM_2 is not significant in any of the near-bottom records since inertial flows are damped, while the shallow water constituent M_3 only appears in the spectra for MF9.

2.4 Spatial variability of the flow

Within the bottom meter of the axial valley, spatial variability in currents is strongly controlled by local topographic and buoyancy effects. Vertical velocities range from -2 cm/s at sites where flows follow the sloping bottom to +5 cm/s in areas of vigorous diffuse venting. The extraordinary spatial variability in the orientation and strength of horizontal velocities is illustrated in the current vector plots for the 2001 short-term records (figure 2.3), which show little correspondence from one location to another, even within the same vent field. In contrast to the 1-5 cm/s along-axis prevailing flow observed at about 15 mab in the valley (Thomson et al., 2003), the record-means measured in the bottom meter range enormously in magnitude and direction. Current ellipses for oscillatory flows (tables 2.2 and 2.3) also show a randomized orientation but are similar to flows within the valley in the predominance of the semidiurnal tide.

The reasons for this lateral inhomogeneity of near-bottom flows are numerous. Topographic features as small as one meter in height can deflect, realign or block horizontal currents as well as shed eddies, affecting the flows measured at 0.5 mab. In areas of hydrothermal venting, velocities may also be influenced by buoyant plumes and the entrainment circulation patterns that are set up around them.

Table 2.3: Record-mean statistics and tidal current ellipse parameters for the short-term MAVS deployments: record-mean speed (sp) and direction (dir); semimajor (M), semiminor (m) axes and inclination of the variance ellipse and the K_1, M_2, and M_4 tidal current ellipses. Velocities are measured in cm s^{-1} and direction in degrees clockwise from north. The minus sign in m indicates clockwise rotation. Only significant values (signal/noise>1) are shown. The last column lists the percentage of the variance (of the filtered record) explained by the fit. Values in bold indicate errors less than 25% in the axes and less than 15° in the inclination.

Dep.	Mean		Variance			K_1			M_2			M_4			%
	sp.	dir	M	m	θ	M	m	θ	M	m	θ	M	m	θ	var
HR1	2.6	79	1.0	0.9	28	0.2±0.2	0.1±0.1	42±44	0.6±0.2	0.1±0.3	348±34	0.3±0.2	0.2±0.2	303±95	23
HR2	7.8	208	5.9	2.7	42	**2.0±0.2**	0.3±0.7	1±23	**5.6±0.6**	0.0±0.7	**18±7**	2.0±0.7	0.1±0.5	**41±15**	50
HR3	5.7	181	2.5	1.0	22	0.7±0.3	-0.1±0.4	37±34	**2.6±0.3**	0.1±0.4	**20±9**	0.8±0.3	0.0±0.3	49±27	55
CB5	0.8	212	0.8	0.2	56	0.3±0.1	0.0±0.0	**350±8**	0.1±0.0	0.0±0.1	28±30	0.2±0.1	0.0±0.1	355±19	22
CB6	2.7	143	2.4	1.2	9	**1.0±0.1**	0.4±0.3	20±22	**2.4±0.1**	-0.1±0.3	**13±9**	0.3±0.3	-0.1±0.1	64±21	57
CB7	3.0	9	2.9	1.2	15				2.3±1.2	-0.1±0.4	**8±11**	0.9±0.4	-0.2±0.3	15±19	36
CB8	1.4	176	1.2	0.8	58	**0.8±0.2**	0.1±0.2	**319±14**	**0.9±0.2**	-0.1±0.2	**311±12**	0.3±0.2	-0.1±0.2	36±47	49
CB9	3.3	330	1.3	0.6	9	0.6±0.2	0.0±0.1	**304±14**	0.7±0.2	0.0±0.1	**307±10**	0.3±0.1	0.0±0.1	311±39	54
R1	4.2	323	1.7	1.2	12	0.5±0.4	0.1±0.4	233±60	1.0±0.5	0.2±0.4	275±21	0.4±0.4	-0.1±0.3	231±58	18
R2	2.3	281	0.9	0.6	271				**0.6±0.1**	0.0±0.2	354±30	0.2±0.2	0.0±0.1	79±53	20
MF1	3.8	331	3.6	1.2	333				**4.0±0.9**	-0.1±0.5	**335±9**	0.8±0.5	0.5±0.3	334±40	68
MF2	3.0	321	1.6	1.0	248	0.4±0.3	0.0±0.4	18±58	0.7±0.3	-0.5±0.3	353±76	0.5±0.1	0.2±0.3	344±44	30
MF3	2.5	20	1.7	1.3	299				**1.2±0.3**	-0.1±0.3	**61±11**	**1.1±0.2**	0.1±0.5	335±27	39
MF4	2.7	11	2.9	1.4	333	0.6±0.4	0.0±0.4	13±40	2.1±0.7	0.4±0.7	304±20	1.1±0.6	0.1±0.6	294±33	36
MF5[a]	3.1	225	1.7	0.8	250	1.2±0.6	0.0±0.6	36±32	**1.1±0.2**	0.0±0.2	**26±11**				44
MF7	3.5	32	2.7	1.8	9				2.1±0.6	-0.4±0.3	**10±8**	1.1±0.4	-0.7±0.3	358±28	46
MF8	5.7	298	2.3	1.5	303	0.6±0.6	-0.5±0.5	333±115	**2.0±0.5**	0.3±0.9	344±23	1.0±0.7	0.3±0.5	90±40	58
MF11	2.8	12	1.9	0.8	20	0.4±0.3	0.2±0.4	68±97	1.9±0.6	-0.1±0.2	**14±6**				61
MF12	2.6	59	2.3	0.8	235	0.7±0.5	0.2±0.2	313±24	**2.4±0.6**	-0.2±0.2	**122±5**				60
MF14[a]	0.8	131	2.2	0.9	265				**1.2±0.3**	-0.2±0.1	**89±5**				30
CV	3.3	10	1.8	0.8	208	**1.6±0.3**	-0.3±0.2	**98±8**	**1.3±0.2**	0.4±0.3	**89±13**	0.4±0.2	-0.3±0.2	328±72	68
B1	2.3	46	1.1	0.7	248	0.5±0.5	0.0±0.3	285±29	0.5±0.4	0.1±0.3	275±29	0.4±0.3	0.2±0.3	38±61	41
B3	1.1	180	1.1	0.6	265	0.4±0.2	-0.1±0.2	68±27							19

[a]Sampling is not continuous

Given these constraints, flows in the bottom meter can be expected to not only vary laterally but be quite different from overlying currents at higher altitudes within the valley. Figure 2.3 includes predicted currents derived from harmonic analysis of current data collected at 25 mab and $\sim$ 100 m to the northeast of the MEF in 1995 (H. Mofjeld, pers. comm.). Even though the current data from the MAVS shown in the figure are not de-meaned, it is quite apparent that the predicted current at 25 mab is not a good representation of the flows measured at 0.5 mab. In areas with no hydrothermal and little topographic influence, near-bottom currents are still affected by friction. Figure 2.4 shows velocity profiles up to 80 mab measured by an ADCP deployed next to the MAVS at the central valley (CV), a site away from hydrothermal venting and characterized by relatively smooth topography. The bottom turbulent Ekman layer thickness at this location estimated from friction velocities (see Chapter 3; Garcia Berdeal et al. (2006)) is $\sim$ 15 m, which agrees well with the vertical structure observed in the figure. The flow measured by the MAVS in this case is more representative of flows above, although generally weaker in magnitude. As seen in the velocity profiles, flows within the valley can also present significant shear above the bottom boundary layer. This vertical shear can be larger (both in magnitude and direction) near hydrothermal vents or the valley walls as will be seen in Chapter 3. For this situation, it can be misleading to infer characteristics of near-bottom flows from currents measured at tens of meters above the bottom.

For locations where bottom velocities are predominantly tidal and with a clear principal component, an inverse barotropic tidal model for the region[1] (Egbert et al., 1994; Egbert and Erofeeva, 2002) can be helpful to predict slack and peak tides. Figure 2.5 compares the de-meaned velocities measured by the MAVS at MF1 with the tidal prediction and the tidal model. In this example, there is a reasonable agreement in phasing between the north-south (v) components of the velocity measured by the

[1]Available at www.coas.oregonstate.edu/research/po/research/tide/region.html

Figure 2.3: Thirty-minute averages of vector velocities for the 2001 short-term deployments. North is upward. Top row corresponds to a tidal prediction derived from harmonic analysis of current meter data collected at 25 mab and northeast of MEF (H. Mofjeld, pers. comm.). Scale is in cm/s. Year day 174 corresponds to June 23, 2001.

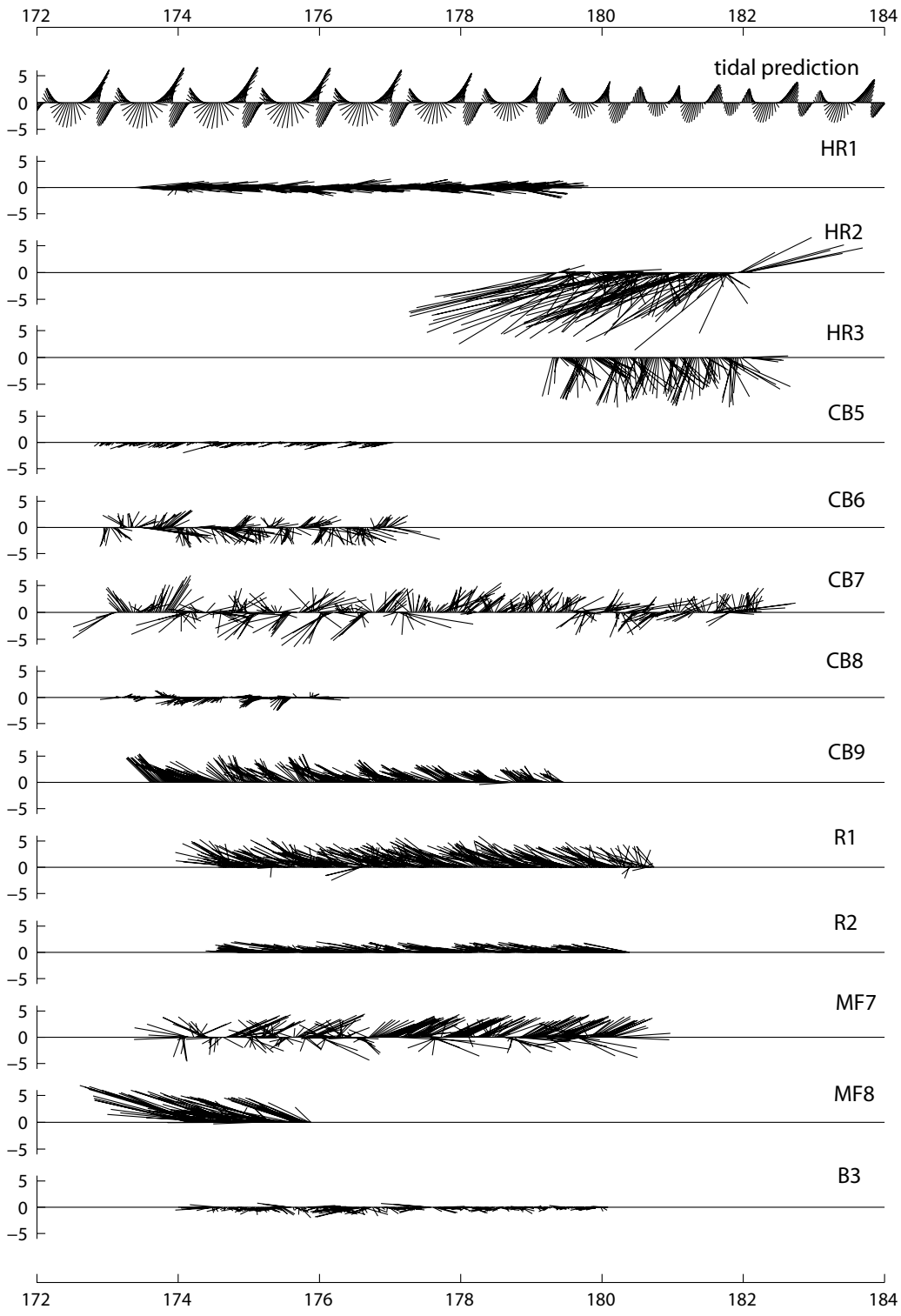
172
174
176
178
180
182
184
tidal prediction
HR1
HR2
HR3
CB5
CB6
CB7
CB8
CB9
R1
R2
MF7
MF8
B3
5
0
−5
Year day 2001

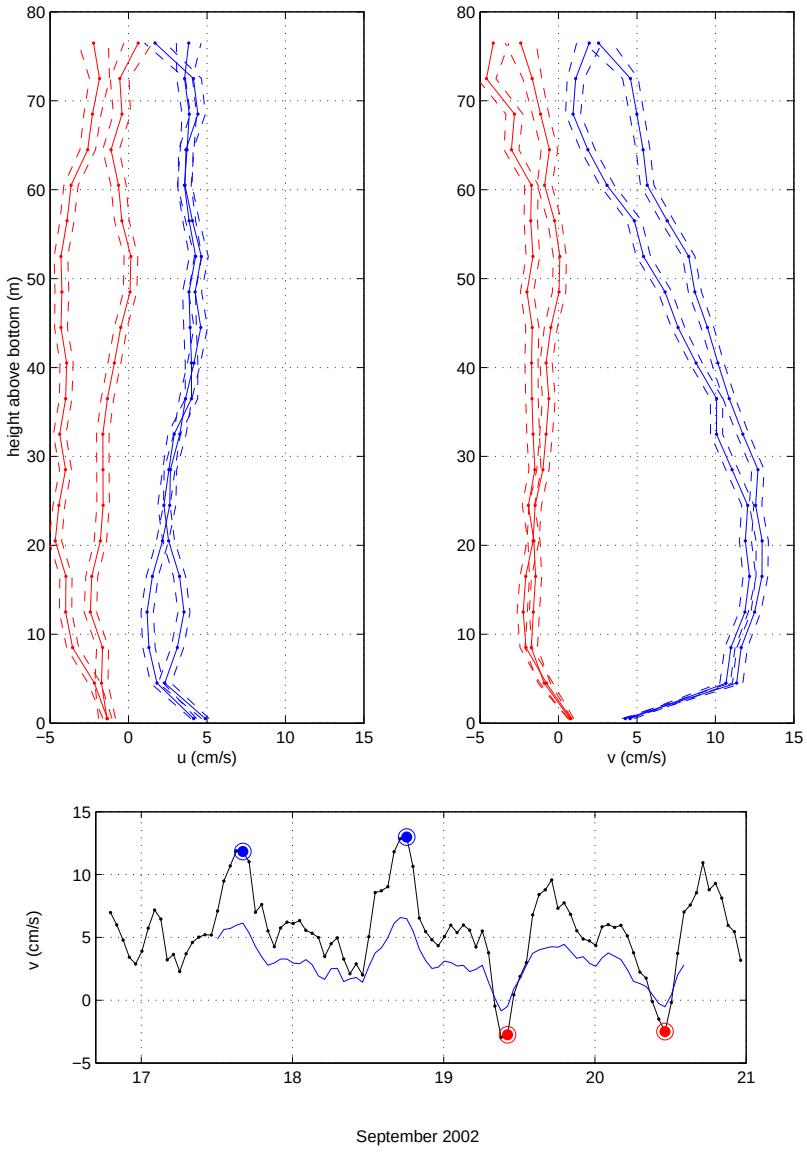

Figure 2.4: (Top) Profiles of east-west (top left) and north-south (top right) velocity components measured at CV at peak northward tide (blue) and peak southward tide (red). (Bottom) Time series of north-south velocity measured at 12 mab by ADCP (black) and at 0.5 mab by MAVS (blue). Peak tide times shown on top panels are marked.

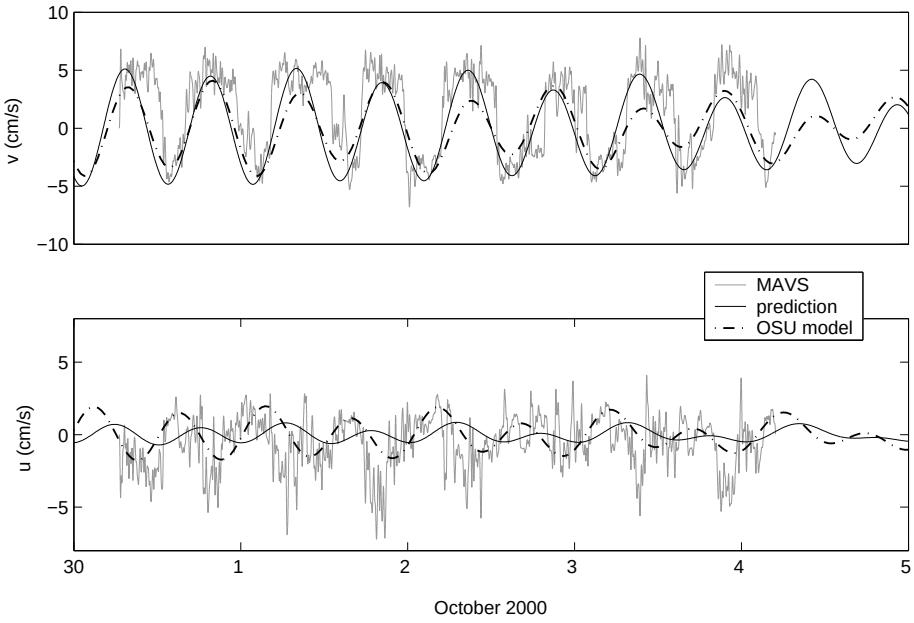

Figure 2.5: North-south (top panel) and east-west (bottom) components of currents measured at MF1 (gray), from a tidal prediction based on velocity data taken at 25 mab and to the northeast of MEF (black line), and from a barotropic tidal model (dot-dashed).

MAVS, from the tidal prediction, and from the model. The square-wave nature of the record at 0.5 mab is evidence of the presence of higher harmonics (see table 2.3), as mentioned in the previous section. In cases where instead of a predominant north-south direction the bottom velocity record shows a predominant east-west direction, then u rather than v will be in phase with the v from the model and the prediction. In the figure, there is a phase lag between u of the model and the data-based prediction. This is not surprising since the currents from the inverse barotropic tidal model follow the direction of the Kelvin wave, i.e., parallel to the coastline, with a principal component 25° west of north, whereas the predicted currents follow the direction of the ridge axis (20° east of north). While the phase of the principal component of near-bottom flows may be predicted from the model, their magnitude and orientation are, as discussed previously, more difficult to determine other than with direct measurements.

2.5 Variability in the bottom boundary layer turbulence field

Reynolds stress and turbulent heat fluxes were calculated using a direct correlation method from the short-term velocity and temperature MAVS records. The friction velocity was estimated from the Reynolds stress via

$$u_* = \left[\left(\overline{u'w'}\right)^2 + \left(\overline{v'w'}\right)^2 \right]^{1/4}, \tag{2.1}$$

where the primes indicate deviations from the 17-minute mean. Buoyancy fluxes (B) were obtained assuming that temperature was the dominant contributor to the buoyancy (b'):

$$B = \overline{w'b'} = \alpha g \overline{w'T'}, \tag{2.2}$$

where α is the thermal expansion coefficient and g is the acceleration of gravity. The correlations in (2.1) and (2.2) were calculated over 17-minute intervals, a time period long enough to obtain robust statistics in the turbulence, yet short enough to ensure that the turbulence is stationary. To quantify the sources and sinks of turbulent

kinetic energy (TKE), besides the buoyancy flux given in (2.2), the production of TKE by shear

$$S = \frac{u_*^3}{\kappa z}\Phi_m \tag{2.3}$$

and the loss of TKE by dissipation ϵ were estimated. The mixing length used in (2.3) differs from the product of the height above the bottom z and von Karman's constant $\kappa = 0.4$ in regions of non-zero buoyancy flux as determined by the empirically derived stability function

$$\Phi_m = \begin{cases} \left(1 - 16\frac{z}{L}\right)^{-1/4} & \frac{z}{L} < 0 \\ \left(1 + 5\frac{z}{L}\right) & \frac{z}{L} > 0 \end{cases} \tag{2.4}$$

where L is the Monin-Obukov length scale

$$L = -\frac{u_*^3}{\kappa \overline{w'b'}} \tag{2.5}$$

(Dyer, 1974). The turbulent dissipation rate ϵ was calculated from the wave number spectra of the vertical velocity w using the inertial dissipation method (Gross and Nowell, 1985; Thwaites and Williams, 2001) for the time intervals that comply with Taylor's frozen turbulence criterion (that is, the standard deviation of velocity is less than half the mean velocity (Thwaites and Williams, 2001)). For the details of this calculation see Pruis (2004).

Selected time series of u_*, B, S and ϵ are presented in figures 2.6-2.9 along with the mean horizontal and vertical velocities and temperature averaged over the 17-minute intervals to investigate how the turbulent properties depend on the "mean" flow and temperature. The records shown are representative of the variety of conditions found in the bottom boundary layer, which range from predominantly shear-driven turbulence to predominantly buoyancy-driven convection. The discussion that follows for each case focuses on the temporal variability of turbulence parameters and production terms on tidal scales. For a discussion of the record-mean turbulent heat flux, production and dissipation see Pruis et al. (2006).

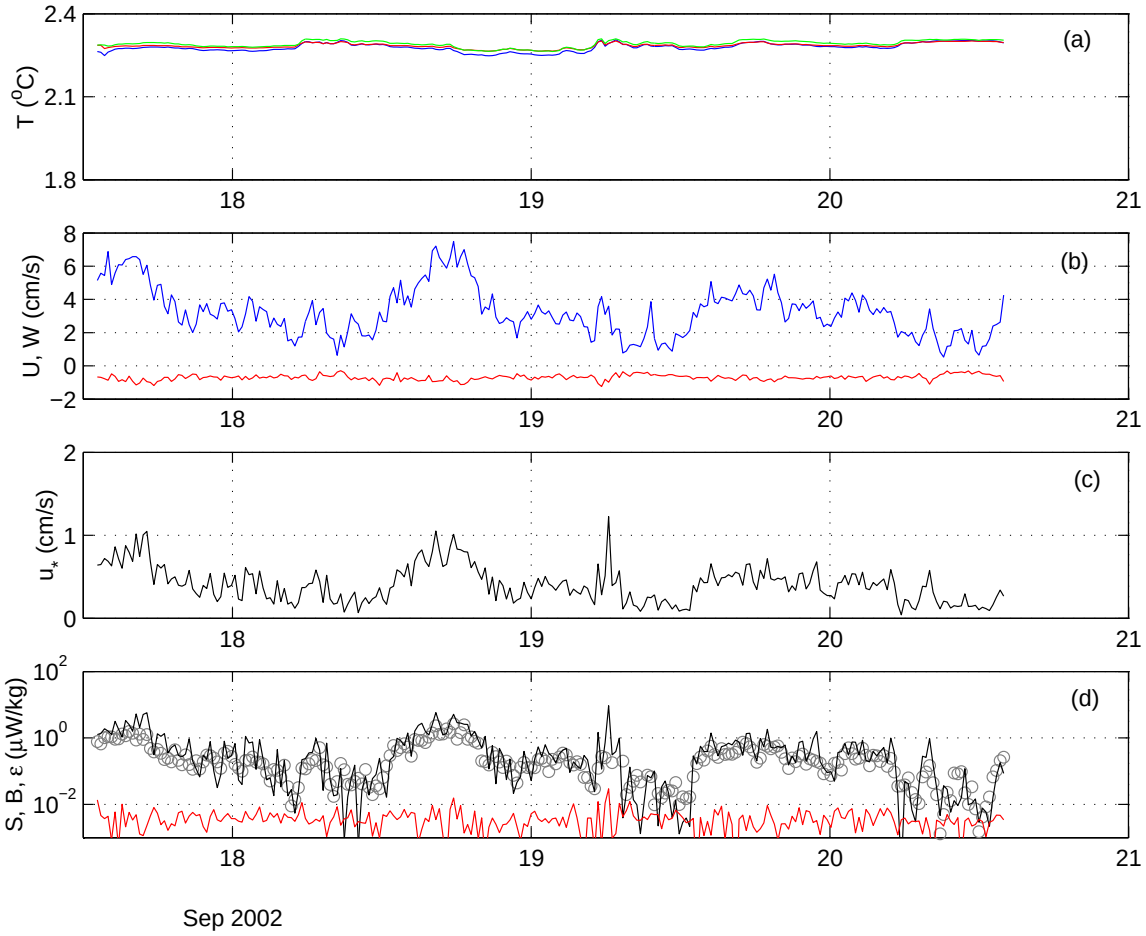

Figure 2.6: Time series of turbulent quantities for deployment CV. (a) Temperature at the top (blue), middle (red), and bottom (green) thermistors. (b) Speed of the horizontal velocity (blue) and vertical velocity (red). (c) Friction velocity. (d) Shear production (black), buoyancy production (red), and dissipation (circles).

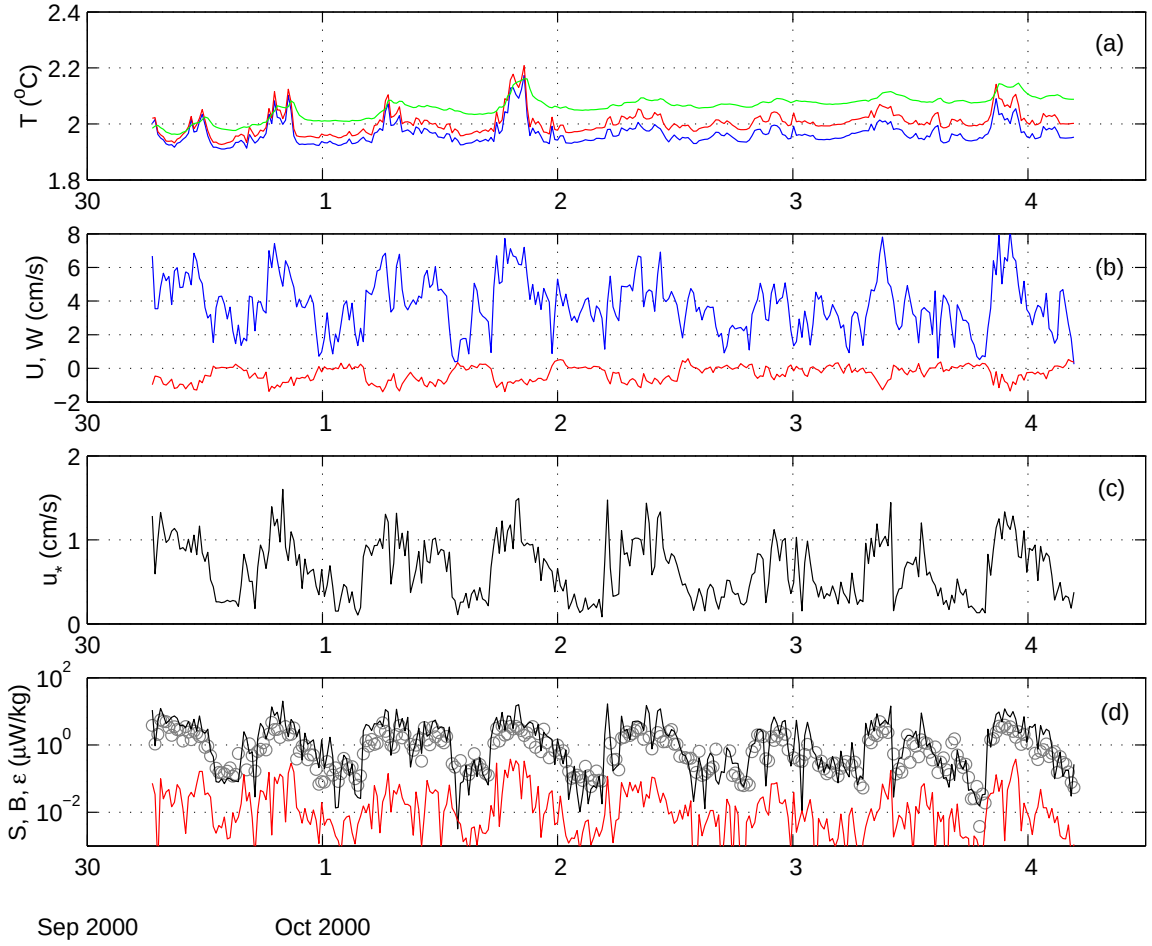

Figure 2.7: Same as in Figure 2.6 but for deployment MF1.

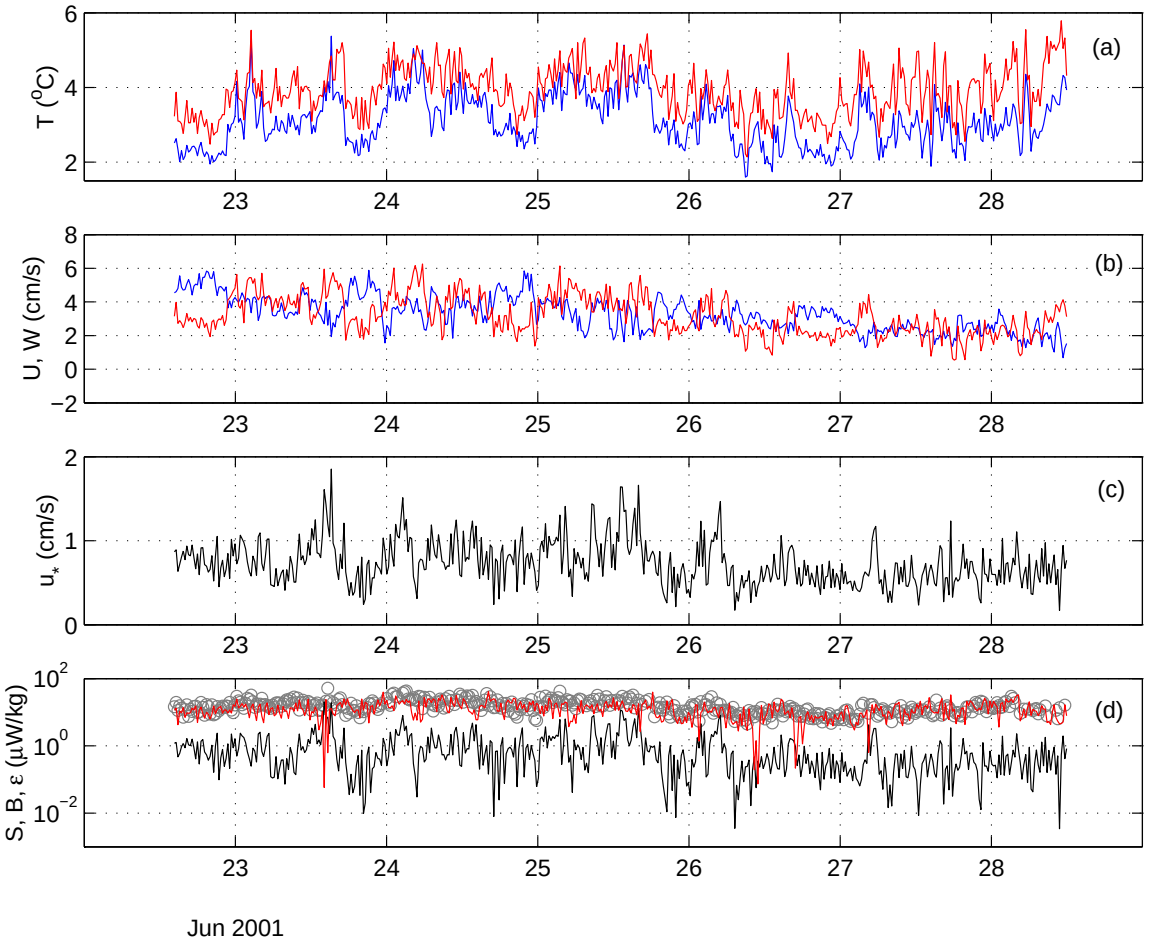

Figure 2.8: Same as in Figure 2.6 but for deployment CB9. The temperature from the bottom thermistor is off-scale ($> 40°$C) and is not shown.

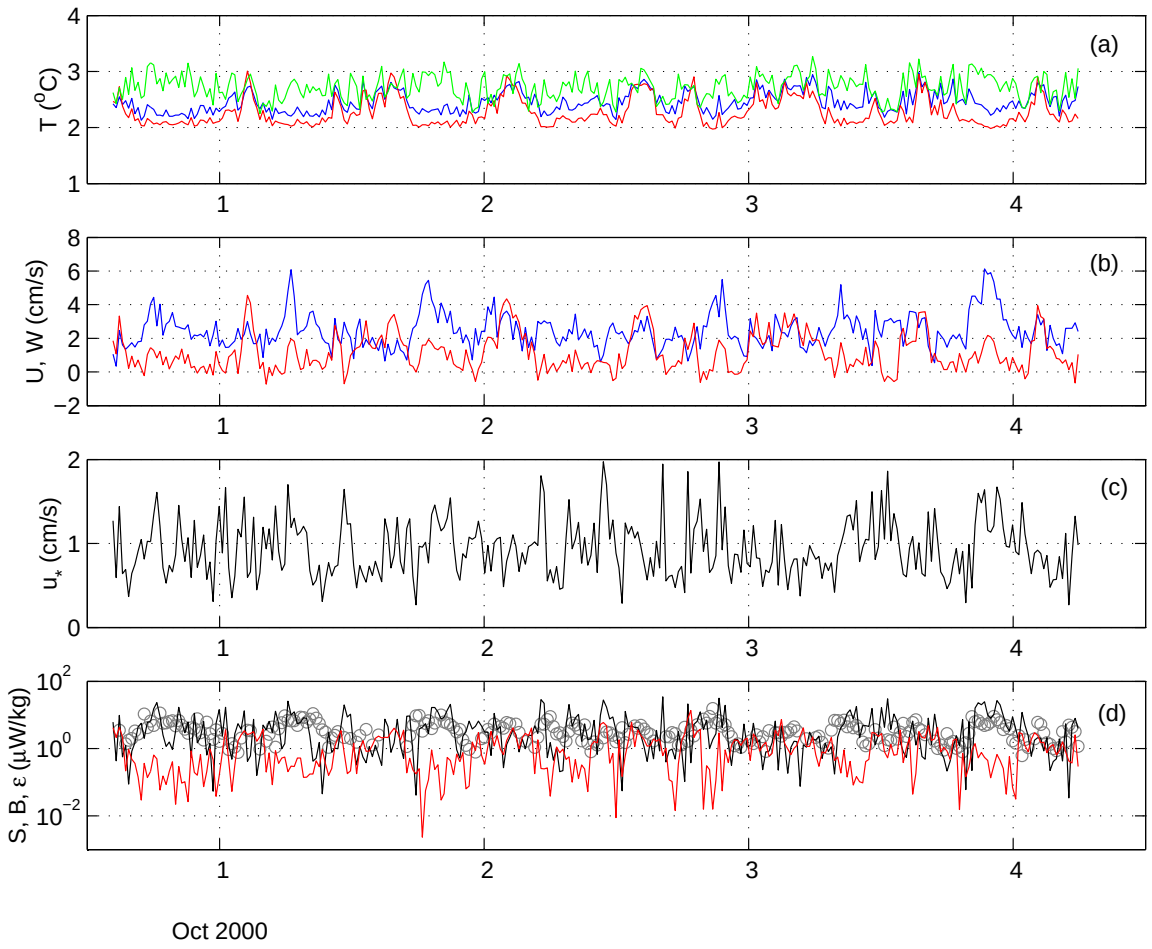

Figure 2.9: Same as in Figure 2.6 but for deployment MF3. For this deployment, due to a bent thermistor chain, the top thermistor (blue) is below the middle thermistor (red).

Figures 2.6 and 2.7 correspond to records from years 2002 and 2000 respectively, where shear-driven stress dominated the production of TKE in the bottom boundary layer. CV was deployed in the central valley several hundred meters away from active hydrothermal venting, in an essentially unstratified boundary layer, as reflected in the temperature records (figure 2.6(a)), and away from large topographic structures. On the other hand, MF1 was deployed west of high temperature vent known as Hulk (in the MEF) in a pocket of warm sediment within lobate lavas, about 5 m to the northwest of a crack venting low temperature hydrothermal fluid. The corresponding temperature record (figure 2.7(a)) shows temporal variability superposed on a weakly unstable boundary layer. Both records are dominated by tidal flows, but while CV shows a predominant diurnal variability, MF1 is strongly semidiurnal (figures 2.6(b) and 2.7(b)). On tidal timescales, vertical velocities are strongly correlated with horizontal velocities suggesting that vertical flows are generated by tidal currents following the local sloping topography. On turbulent timescales though, the flow is not constrained to follow the bottom, so this should not affect calculation of Reynolds stress and friction velocities. The tidal variability is also reflected in the time series of friction velocities (figures 2.6(c) and 2.7(c)), which show excursions as large as the mean value. Both records show that production of TKE by shear is several orders of magnitude greater than production of buoyancy and is nearly balanced by dissipation (figures 2.6(d) and 2.7(d)). For the central valley record, the buoyant production is negligible (since the measured buoyancy flux is below the level of accuracy, $10^{-2}\mu$W/kg of the instrument) illustrating a case of standard shear-driven turbulence. For MF1, although the buoyancy production does not dominate the TKE budget, it does show some temporal variability, with maxima at peak tide that rise above the noise floor and coincide with an increase of the temperature in the boundary layer and northwestward flow. We interpret these periods of warming and enhanced TKE production as a consequence of a turbulent plume of hydrothermal fluid possibly advected from the nearby diffuse vent.

In contrast to the two cases discussed above, record CB9 is an example where buoyancy dominates the production of TKE (figure 2.8). This MAVS was deployed in Clam Bed next to a mound of the tube worm *Ridgeia piscesae* in its "lush" (short and thick) morphology. Below the velocity sensors, the bottom temperature measured with Jason's probe reached 150°C (while it is unclear whether the upper-end temperature calibration of the probe was valid, the bottom below this instrument was hot enough to melt the bottom thermistor and burn the bean-bag base of the MAVS case) and vertical flow was visually obvious. The average heat flux at this vent was 34000 W/m^2, resulting in buoyancy production of TKE nearly an order of magnitude larger than shear production (figure 2.8(d)). Positive vertical velocities of magnitude comparable to the horizontal velocities accompany the large heat flux. Temporal variability in the mean and friction velocities is not as strongly tidal as in the shear-driven cases, but instead appears to be linked to changes in the buoyancy flux. After day 26, the buoyancy production drops by nearly a factor of two. This drop is reflected in a weakening of W, U and u_* and suggests that the buoyancy flux is not only important for generating turbulence, but also for driving a mean flow in the immediate vicinity of this vent. The dependence of u_* (hence the shear-production) on the buoyancy production is also noted by Pruis et al. (2006) from the analysis of the record-mean turbulence properties. The dissipation in this record is largely balanced by buoyancy production, except during short ($\sim$ 1 hour) periods when B drops but ϵ persists. A similar prolongation of the dissipation following cessation of buoyancy production has been observed in the oceanic surface layer (Brainerd and Gregg, 1993).

Figure 2.9 corresponds to record MF3 where both shear and buoyancy feed the turbulence in the bottom boundary layer. This instrument was positioned in shimmering water, west of the vent Grotto in MEF and near a mound of tubeworms at the center of which the temperature reached about 40°C. The thermal boundary layer at this site alternates between periods of unstable stratification and periods when it

is homogeneized at the bottom temperature (for example, shortly after Oct 1). The latter coincide with periods of slack tide, when horizontal and vertical velocities are of the same magnitude and the buoyancy and shear production are nearly equal. Between these periods, shear production dominates and is approximately balanced by dissipation. The strength of the friction velocity is quite large but its temporal variability is not clearly tidal (cf. CV and MF1).

The records described above illustrate that the sources of TKE in the bottom boundary layer of the axial valley can range from purely mechanical to dominantly buoyant. The critical parameter that quantifies the relative importance of the two TKE sources is the stability parameter, z/L (Large and Pond, 1981). This ratio is tabulated in table 2.4 for all the short-term records. Since most of the short-term deployments were over or in close proximity to diffuse vents, z/L is negative as expected from a destabilizing buoyancy flux. When $z/L < -1$ buoyancy dominates while when $z/L > -1$ mechanical turbulence dominates. In the record-mean sense only one record corresponds to a free convective regime, while in eight others the turbulence is dominantly driven by shear. In the majority of the cases both buoyancy and shear contribute nearly equally to the production of TKE in the record-means. However, significant temporal variability is found in tidal time scales as illustrated in figure 2.9.

This variability in the turbulent properties of the boundary layer is reflected in the large standard deviations (25-55% of the mean) listed for u_*. Along with record-mean speed and u_*, table 2.4 also lists C_{D100}, calculated from

$$C_{D100} = \left(\frac{u_*}{U_{100}} \right)^2$$

where the mean speed at 1 mab, U_{100}, has been extrapolated from 0.5 mab using the "law of the wall". Since the friction velocities are a significant fraction of the mean speed, the drag coefficients inferred are relatively large (even disregarding the considerable scatter present which seems related to the tidal phase) compared to the

Table 2.4: Record-mean turbulent properties for the short-term MAVS deployments. The turbulent heat flux is calculated as $Q = \rho c_p \overline{w'T'} = (\rho c_p / g\alpha)B$. The stability parameter (z/L) is calculated as $-\langle B \rangle / \langle S \rangle$, where $\langle\rangle$ indicates a record-mean. N/A applies to those records where the thermistors failed, while N/S applies to heat fluxes that are not significant since they lie below the level of accuracy of the instrument (10 W/m^2).

DEP.	Speed (cm/s)	Mean u_* (cm/s)	SD u_* (cm/s)	C_{D100} ($\times 10^{-2}$)	Q (W/m^2)	z/L
HR1	2.86	0.55	0.28	2.2	N/A	N/A
HR2	8.00	0.68	0.33	1.3	210	-0.03
HR3	5.79	0.55	0.21	0.8	N/A	N/A
CB5	1.04	0.29	0.16	3.9	N/S	N/S
CB6	3.12	0.80	0.34	3.2	480	-0.02
CB7	3.17	0.44	0.21	1.6	N/A	N/A
CB8	1.66	0.49	0.17	4.0	N/A	N/A
CB9	3.68	0.73	0.27	2.4	34000	-11.82
R1	4.84	1.02	0.46	2.6	34000	-2.50
R2	2.64	0.64	0.22	3.1	3500	-1.00
MF1	4.02	0.65	0.34	1.7	40	-0.01
MF2	3.27	0.64	0.28	2.2	700	-0.13
MF3	3.13	0.94	0.34	4.1	3400	-0.22
MF4	3.64	1.19	0.42	4.9	19000	-0.96
MF7	4.49	1.89	0.48	6.0	150000	-3.05
MF8	6.23	1.41	0.42	3.1	42000	-1.31
MF11	3.19	0.68	0.25	2.9	4200	-1.00
MF12	3.17	0.89	0.26	4.0	12000	-1.75
MF14	2.61	0.53	0.22	2.8	140	-0.04
CV	3.33	0.41	0.22	1.1	N/S	N/S
B1	2.54	0.49	0.14	2.4	990	-0.62
B3	1.80	0.95	0.32	7.8	19000	-1.94

canonical value of 10^{-3} for sandy seabeds. The values obtained at sites with little or no venting are comparable to ranges obtained over extreme bottom roughness (e.g., Reidenbach et al. (2005) finds C_{D100} of 0.009 to 0.016 over coral reefs). Our measurements were taken over bottoms characterized by complex bedforms (e.g., fragmented basalt, pillow lavas, mounds of tube worms) and bathymetry (e.g., sulfide structures, faults). In addition, in areas with diffuse venting, destabilizing buoyancy fluxes could enhance the drag coefficients as observed in the atmospheric surface layer by Mahrt et al. (2001). An enhancement of the stress in an unstable atmospheric boundary layer has also been observed by Chelton et al. (2001) and is thought to be due to downward mixing of momentum by convection (Wallace et al., 1989).

2.6 Implications for the dispersal of vent larvae

From hydrodynamical considerations, the dispersal of larvae involves horizontal and vertical transport processes. Vertical processes are especially important both in the initial stages of dispersal, when the larvae drifts away from the spawning grounds, and in the final stages when the competent larvae settle and colonize new habitats. Vertical fluxes of larvae (Φ) can be modeled as set by the turbulent diffusivity ($A_v = \kappa u_* z$ in the constant stress layer), the mean vertical velocity of the fluid ($\bar{w}$), and the fall velocity of the larvae (w_f)

$$\Phi = -A_v \frac{\partial C}{\partial z} + \bar{w}C + w_f C \tag{2.6}$$

where C is the larval concentration (modified from Gross et al. (1992)). The last term in (2.6) is a function of the larva's physiology and behavior, while the first two terms depend on the flow in the bottom boundary layer and hence, their relative importance to Φ may be inferred from the characteristics of near-bottom flow described in the previous section. Clearly, the enhanced turbulence observed in the axial valley due to bottom roughness and sources of buoyancy, as well as the buoyant plumes themselves, will affect this vertical exchange between the water column and the benthos of tracers

in general, and of larvae in particular. It is important to note that the vertical coordinate in (2.6) is normal to the bottom while the vertical velocities shown in figures 2.6-2.9 may have a component parallel to the ocean floor that is correlated with the horizontal currents on tidal timescales and would not contribute to $\bar{w}$.

For negatively buoyant larvae ($w_f < 0$) and away from buoyant sources ($\bar{w} = 0$), fluxes due to larval sinking and turbulent diffusion oppose. The steady-state balance between these two terms results in a larval concentration profile of the form

$$C(z) = C(z_o)\left(\frac{z_o}{z}\right)^{Ro} \tag{2.7}$$

where the Rouse number

$$Ro = \frac{|w_f|}{\kappa u_*}$$

is a measure of the relatively strengths of these opposing fluxes. For $Ro \ll 1$ larval concentrations are well-mixed in the boundary layer, while for $Ro \gg 1$ larvae are concentrated in the bottom of the boundary layer (Gross et al., 1992). Larvae may be able to influence their sinking velocity, depending on their stage of development. The fall velocity (w_f) not only depends on the larval species, but also on its developmental stage, as this determines the weight and size of the larvae or whether they have behavioral capabilities such as swimming. Sinking velocities of vent larvae are, like many other aspects of their physiology and behavior, not well known and often have to be inferred by comparison with those of related shallow water taxonomic groups, which range from 0.01-1 cm/s (Butman, 1996). Taking a typical fall velocity for a larva of a coastal bivalve, $w_f = 0.25$ cm s^{-1} (Grassle et al., 1993), then using the record-mean u_* from table 2.4, Rouse numbers in the bottom boundary layer of the axial valley are of order one. This would mean that at 2 mab, the larval concentration would be 25% of that at 0.5 mab (2.7). However, because of the large temporal variability of u_*, the Rouse number may show significant modulations over a tidal period, fluctuating between values less than one during peak tide and greater than one during slack tide. This suggests that, from hydrodynamical considerations

alone, at locations like the central valley site (figure 2.6) larvae may preferentially settle to the seabed during slack tide (Gross et al., 1992) and be mixed vertically in the bottom boundary layer with stronger flows.

In areas of diffuse venting, where slack tide is a period of enhanced convective activity (as in figure 2.9), the upward mean larval flux associated with the buoyant plumes, $\bar{w}$, could exceed the downward flux associated with w_f. In this case, larvae might not settle out during slack, but instead leave the benthic boundary layer to enter the water column. During periods of larger tidal flows over diffuse vents, when mechanical production of turbulence exceeds buoyant production, $\bar{w}$ may be reduced such that $|w_f| > \bar{w}$, and the flux equation (2.6) would be dominated by a Rouse-type balance. However, over areas of strong venting, an upward transport would be favored for all times, not just slack tide (e.g., CB9).

The temporal and spatial variability of the bottom boundary layer physics favor a wide range of conditions for settlement and vertical redistribution that larvae could exploit to their advantage. But hydrodynamical considerations alone might not predict the vertical fluxes of larvae as would be expected from purely passive tracers (Gross et al., 1992; Crimaldi et al., 2002). As mentioned previously, the falling velocity w_f can be modified by larval behavior, for example, by active upward swimming, which can make the larvae nearly neutrally buoyant. Adding complexity to the picture, it is thought that turbulence may play a role in triggering these behavioral changes. For example, there is evidence that competent larvae of a coastal gastropod modify their behavior to sink in turbulent conditions (Fuchs et al., 2004). As turbulence intensifies, larval movement is more dominated by the flow and, in very strong turbulence, any active larval swimming is overwhelmed by turbulent mixing (Koehl and Powell, 1994). The degree to which turbulence may influence larval behavior, if at all, would be specific to the species and developmental stage of the larva. In any case, behavioral aspects more likely modify larval dispersal rather than control it and ultimately, a passive dispersal of the larvae is a good first-order constraint on

the problem (Mullineaux and France, 1995).

The importance of vertical motion in larval dispersal is clear: by being able to change their vertical position, they can (1) take advantage of sheared flows in the valley (2.4; Chapter 3) or above the ridge, where large velocities result in maximum dispersal potential, and (2) avoid topographic barriers. Larvae can be entrained in high temperature plumes as well as low-temperature diffuse vent fluid rising 10-40 mab. However, entrainment in rising plumes is only favored during slack tide (Kim et al., 1994), and transport in near-bottom currents (within 15 m of the seafloor) is thought to be a more prevalent dispersal mechanism (Kim and Mullineaux, 1998). Certainly, dispersal at lower levels within the axial valley seems a less risky pathway than at levels above the ridge, where larvae can be exposed to episodes of cross-axis flows that could transport them away from areas of hydrothermal activity.

Near-bottom flows are dominated by semidiurnal tidal currents of up to 5 cm/s (table 2.3). Maximum horizontal tidal excursions expected for the M_2 tidal component would be 350 m, a distance sufficient to transport larvae within a vent field but not in between two fields ($\sim$ 2-km apart) in the axial valley. However, while a purely oscillatory, spatially uniform, tidal flow would not result in a net transport over a tidal cycle, the presence of mean flows, episodic events, and/or spatial variability can all lead to a net displacement of larvae. The progressive vector diagram (PVD) calculated from concurrent velocity data measured at sites within a 30 m radius in Clam Bed (figure 2.10) suggests a potential for lateral displacements in the bottom boundary layer of up to 12 km over 4 days. However, from the extraordinary spatial variability seen in the plot, it is clear that Eulerian and Lagrangian flows diverge near topography and therefore the PVDs are a poor representation of the actual trajectories of fluid parcels. Lateral inhomogeneities exist not only in the prevailing current, but also in tidal flows (table 2.3). A horizontally varying tidal flow will induce a net displacement by virtue of a Stokes drift. The strength of this drift depends on the magnitude of the variation of the tidal flow over the tidal excursion. For an M_2

tidal flow of 2 cm/s, the tidal excursion is 140 m. For the records CB5-CB9, at sites separated by 60 m at the most, variations in the semidiurnal tidal flow of 1 cm/s occur over a distance shorter than the tidal excursion, resulting in a maximum Stokes drift of 1 cm/s. Such strong spatial variability in tidal flows is not specific to the Clam Bed area but is observed everywhere in the valley (table 2.3). This suggests that significant Stokes drifts resulting in near-bottom net displacements of larvae can be expected in the axial valley. Convergences and divergences of the Stokes drift field throughout the valley likely result in areas of larval concentration.

The highly dynamic and turbulent environment observed in the near-bottom of the axial valley, will not only affect the dispersal of vent organisms, but also many other aspects of their biology. For example, nutrients and chemical cues for settlement can be advected in many directions in the bottom boundary layer, expanding the grounds suitable for settlement, while turbulence can influence feeding and reproduction by increasing the rate of encounters.

2.7 Summary and Conclusions

Temporal variability of flows in the near-bottom boundary layer of the axial valley at Endeavour Ridge is similiar to what is observed at other depths within the valley. Flows are dominated by semidiurnal tidal (typically 2-3 cm/s) and 4-day frequencies. Diurnal tidal and, especially, inertial currents present a weaker variability, while non-linear wave interactions, resulting in harmonics of the fundamental tidal frequencies such as M_4, are often significant.

Flows in the bottom meter of the axial valley are strongly controlled by both small-scale local topography and hydrothermal buoyant plumes, which result in an extraordinary spatial variability of both horizontal and vertical velocities. Mean near-bottom horizontal flows are generally 1-3 cm/s and their direction is not necessarily along-ridge, in contrast to flows observed at higher altitudes in the valley. The orientation of current ellipses of oscillatory motions is also highly randomized. Vertical

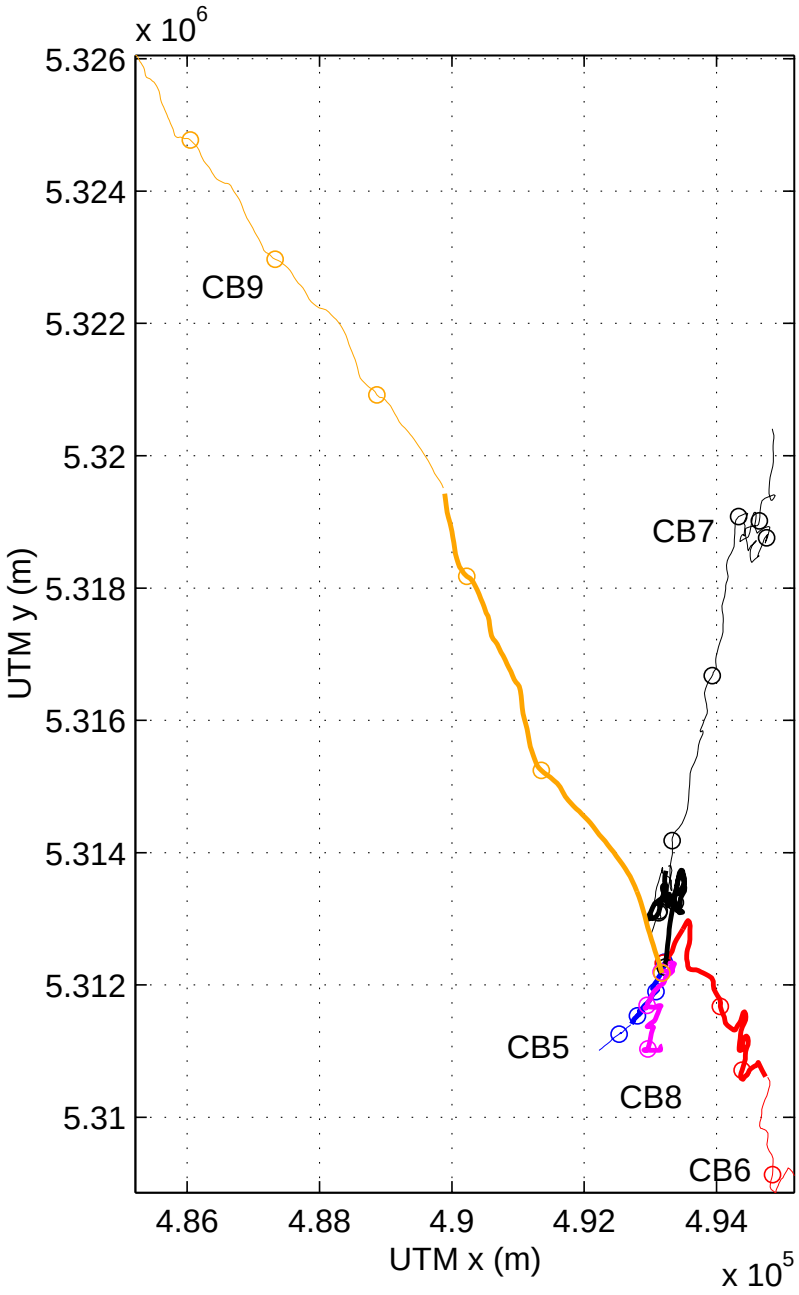

Figure 2.10: Progressive vector diagram (PVD) calculated from the 2001 short-term velocity records in Clam Bed (CB5-CB9). The starting points of the PVD at day 173.6 correspond to the locations of the MAVS, that are within a 30 m radius. The PVD is integrated from year day 173.6 to 176 (thick line) and continued to the end of each record (thin line). The circles mark 1-day intervals.

velocities range from -2 cm/s over regions with a sloping bottom to +5 cm/s over vigorous diffuse venting. Spatial variability exists both laterally and in the vertical, therefore flows measured in the bottom meter at a particular location will not necessarily be representative of the currents observed at several meters of distance or height off the bottom. In spite of this observation, a barotropic tidal model is generally useful to predict the tidal phase and periods of slack or peak tides close to the bottom.

Turbulence in the bottom boundary layer is enhanced because of extreme bottom roughness and the contribution of buoyancy to the production of turbulent kinetic energy in areas of diffuse venting. Here, dissipation values can reach 10 $\mu W/kg$, levels typically observed in tidal channels and estuaries (Gross and Nowell, 1985). In these cases dissipation balances buoyancy production generated by buoyancy fluxes that are one to two orders of magnitude larger than those resulting from the strongest cooling of the ocean surface layer (Marshall and Schott, 1999). Direct estimation of Reynolds stresses yields record-mean friction velocities of order 1 cm/s, although substantial temporal variability exists. Tidal flows modulate the turbulent thermal boundary layer, which over venting is unstably stratified. This often leads to alternation of periods of forced convection (during stronger flows) and free convection (during weaker flows).

The lowest several meters is where the largest abundance of vent organisms and their larvae are found. It is also where a large part of low-temperature hydrothermal vent fluid spreads laterally and this fluid is thought to contribute to the heat flux as much as high-temperature focused sources because of its extensive area coverage. Therefore the hydrodynamical conditions in the bottom boundary layer are key to understanding the dispersion of diffuse hydrothermal fluid and larvae. Flows and turbulent properties in the near-bottom boundary layer will be especially crucial in the early stages of dispersal and final settlement of larvae.

Chapter 3

VERTICAL STRUCTURE OF FLOW IN THE AXIAL VALLEY

3.1 Introduction

The Juan de Fuca Ridge lies along the divergent boundary between the Pacific and Juan de Fuca plates, approximately 400-500 km off the coasts of Washington and Oregon (Figure 3.1). This 400-km long submarine mountain range is oriented 20° east of north (020°N) and is divided into several linear offset segments. The present study focuses on the central portion of the Endeavour Segment, in the northern Juan de Fuca Ridge. Here, the 10-km wide axial ridge rises to a depth of $\sim$ 2100 m at its crest above the regional baseline depth of $\sim$ 2400 m. A 1-km wide median rift valley with an average depth of 100 m dissects the axial ridge crest lengthwise. Several major hydrothermal vent fields lie along this axial valley, among them the well-studied Main Endeavour Field (MEF), at 47° 57'N, 129° 6'W (Tivey and Delaney, 1986, 1985; Delaney et al., 1992; Johnson and Holmes, 1989).

Ridge axis hydrothermal systems have been the subject of numerous investigations over the last two decades, in part motivated by the presence of a rich and diverse ecosystem thriving under extreme environmental conditions, and the potentially important contribution of hydrothermal fluid to the heat and chemical budgets of the deep ocean. A major component of understanding these unique systems requires characterizing near-bottom currents at mid-ocean ridges and determining the flux of heat and the dispersal of biological/chemical species associated with hydrothermal fluid.

Certain aspects of currents near the Juan de Fuca Ridge have been well-studied by a considerable number of observational efforts mostly focused on flow above the

ridge crest (e.g., Thomson et al. (1990); Cannon et al. (1991); Cannon and Pashinski (1997)), specifically, at the level of the neutrally-buoyant plume, approximately 200 meters above bottom (Baker and Massoth, 1987; Thomson et al., 1992). At the Endeavour Segment, mean flows above the ridge crest are about 5 cm s^{-1} and generally directed southward, although significant variability of the cross-axis component exists (Thomson et al., 2003; Veirs, 2003). Current variability is dominated by semidiurnal tidal, inertial ($\sim$ 16 hours), diurnal tidal (which at this latitude is subinertial), and low-frequency (4-8 days) flows. The latter broad spectral band (also known as the "weather band") has been associated with ridge-trapped subinertial waves generated by storm systems (Cannon and Thomson, 1996). Above the ridge, near-inertial and semidiurnal current variations are comparable in magnitude and slightly more intense than subinertial currents (Allen and Thomson, 1993; Thomson et al., 1990). Subinertial motions are trapped to the ridge and experience an amplification of their clockwise rotary component that Allen and Thomson (1993) attribute to the generation of anticyclonic vorticity by vortex squashing over the ridge. Near-inertial currents are also intensified immediately above the ridge (Thomson et al., 1990).

Currents within the axial valley are not as well-documented as flows above the ridge crest. However, the few observations that do exist agree that currents above the ridge are not representative of motions within the valley (Allen and Thomson, 1993; Franks, 1992; Thomson et al., 1990). Mean flows within the valley are typically northward with speeds of 1-5 cm s^{-1} (Thomson et al., 2003; Veirs, 2003). Superimposed on these mean flows are predominantly along-valley oscillatory motions. Semidiurnal tidal flows of several cm s^{-1} dominate, while diurnal and 4-day oscillations are weaker (Thomson et al., 2003). Inertial currents are particularly damped within the valley, presumably too narrow to support rotary motions (Thomson et al., 1990). These previous conclusions were based on single-point current meter data and therefore were inadequate to describe the vertical structure of currents within the valley.

Knowledge of the vertical structure of currents within the axial valley of Endeavour

Ridge is critical for several reasons, including determining the fate of hydrothermal vent fluid, not only because the majority of hydrothermal venting occurs in the axial valley, but also because a significant part of hydrothermal fluid and heat is released in the form of low-temperature diffuse plumes that rise 10-50 meters above the bottom (mab) (Trivett and Williams, 1994; Rona and Trivett, 1992), so remain within the confines of the valley. The vertical structure of flows within the valley also has important implications for the transport of vent larvae by bottom currents. Given that the largest abundances of vent larvae are found close to the bottom and to their vent source communities (Mullineaux and France, 1995), transport by bottom currents may be a predominant dispersal mechanism.

This study presents measurements of currents in the bottom 80 meters of the Endeavour axial valley made at much higher vertical resolution (4 meters) than previous studies. These observations are interpreted in the context of an idealized model for subinertial oscillations within a ridge-valley. This model contrasts with previous theoretical (Allen and Thomson, 1993) and numerical (Lavelle and Cannon, 2001) models for subinertial oscillatory flows over a ridge crest in that it includes valley topography. Unlike Allen and Thomson (1993), continuous stratification is incorporated into the analytical solution. The model is two-dimensional, linear, inviscid and quasianalytic, yet able to capture the basic vertical structure seen in the observations. The model and observations allow speculation as to the fate of larvae within the axial valley.

3.2 Observations in the central valley and in the MEF

A 300-kHz broadband RDI Workhorse Sentinel ADCP was deployed on the seafloor in the axial valley of the Endeavour Segment for periods of 4.2 and 4.8 days during the summers of 2002 and 2003, respectively. The first deployment, located in the central valley at 47° 56.8'N, 129° 5.8'W and 2217-m depth, recorded from 1837 UTC 16 September 2002 to 0003 UTC 21 September 2002. This deployment site was chosen for its smooth topography and distance from hydrothermal vents. The second

deployment site was located 10 m north of Easter Island vent in the southern MEF at 47° 56.9'N, 129° 6'W and 2202-m depth, roughly 250 m northwest of the central valley deployment (Figure 3.1). This location is quite close to a steep valley wall on its west and is surrounded by more complex topography than the central valley site, as well as sources of buoyant hydrothermal fluid. Easter Island is composed of several low-temperature hydrothermal fluid diffuse sources, one of which appeared to be evolving toward higher temperatures over the period 2002-2003. Other high temperature "black smoker" sites are only 30-60 meters distant. Data acquisition at the Easter Island site spanned 0344 UTC 13 July 2003 to 2345 UTC 17 July 2003.

At both sites, the ADCP recorded continuously at a sampling rate of 3 s. The instrument was mounted on a PVC and titanium base that slightly elevated the first measurement bin to 6.5 mab. Other measurement bins were separated by 4 m up to bin 19 (at 78.5 mab), beyond which correlation values of the measurements dropped below usable levels due to a lack of acoustic scatterers in the deep water. While the western valley wall extends up to 2105-2110 m, the eastern wall (not completely defined in the bathymetry of Figure 3.1) only reaches 2125 m. All bins of ADCP data collected lie therefore within the axial valley.

A Nobska MAVS-3 (Modular Acoustic Velocity Sensor) was deployed immediately adjacent to the ADCP in the central valley, to concurrently measure flow in the bottom boundary layer. The MAVS recorded velocities at 0.5 mab with a 5-Hz sampling rate for approximately 3 days. Friction velocity was calculated from both turbulent stresses and the inertial dissipation method (Thwaites and Williams, 2001; Gross and Nowell, 1985). The record-mean friction velocity at the central valley site is in the range $u_\star = 0.36 - 0.40 \times 10^{-3}$ m s^{-1}, depending on the method applied. The thickness of the steady bottom Ekman layer is thus estimated as $\delta = 0.4u_\star/f = 14 - 16$ m, following Weatherly et al. (1980).

Both the ADCP and MAVS data were corrected for a heading offset (that was visually estimated from the ROV gyrocompass) and then averaged over 30-minute

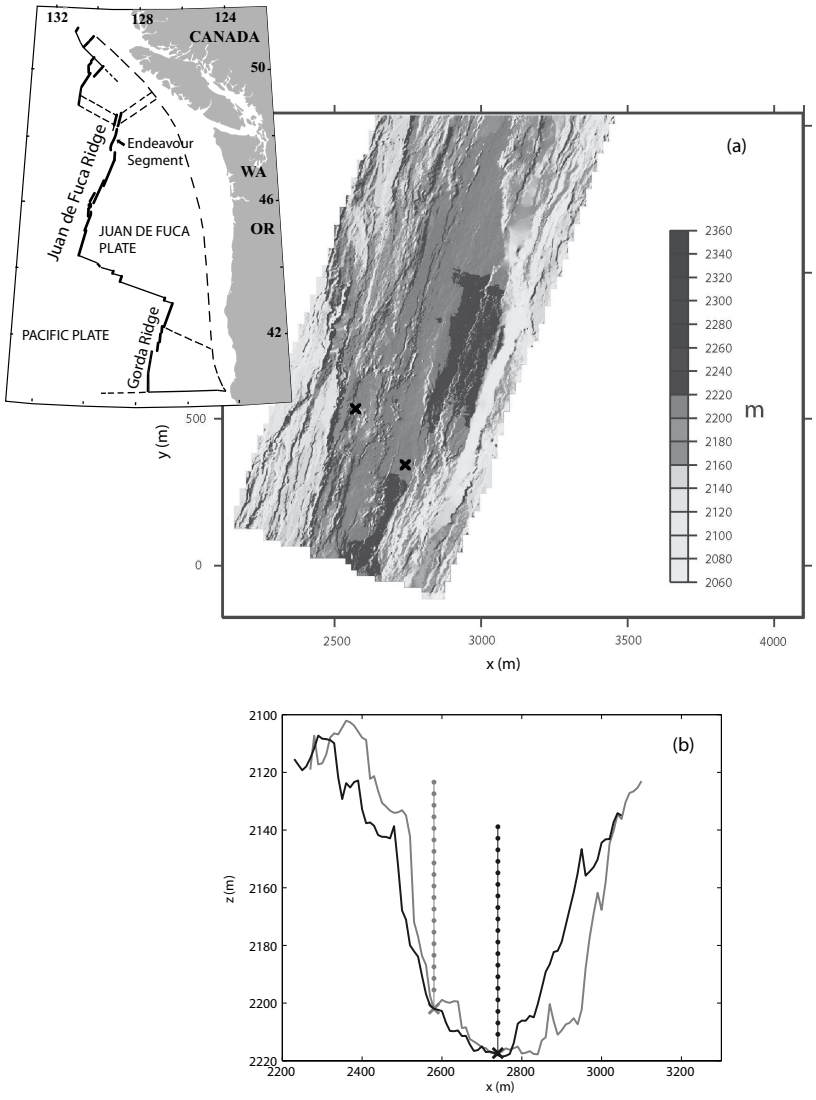

Figure 3.1: (a) Bathymetric map of a portion of the axial valley at Endeavour (adapted from Johnson et al. (2002)). Locations of ADCP deployment sites are marked by x. Inset shows location of Endeavour Segment on map. (b) Two cross sections of the axial valley in the Endeavour Segment at the locations of the ADCP deployments (x) and ADCP bins (4 m intervals in dots). The black (gray) symbols and lines correspond to the 2002 record in the central valley (2003 record in Easter Island, Main Endeavour Field).

periods before calculating the tidal harmonics. The harmonic analysis and calculation of ellipse parameters for the M_2 and K_1 frequencies, and their associated errors were performed using a Matlab version of the Foreman (1978) tidal-analysis package as discussed in Pawlowicz et al. (2002). At all levels, the M_2 and K_1 tidal constituents had a signal-to-noise ratio larger than 2.

3.2.1 Diurnal tidal flow

The tidal current ellipses at both deployment locations are presented in Figure 3.2 for the K_1 frequency (top panels) at several depths within the axial valley. At the central valley site, all diurnal tidal ellipses are clockwise rotary. Figure 3.2(a) shows both a gradual decrease in the eccentricity of the ellipses and an amplification of the major axis with increasing depth down to 15 mab, at the central valley site. In addition, the orientation of the major axis of the ellipses rotates counterclockwise with increasing depth (except at the bottom-most level, at 0.5 mab, where it turns clockwise) and aligns with the along the valley direction. Figure 3.2(b) shows the diurnal tidal current ellipses corresponding to the Easter Island record. At this location, the higher ellipses tend to be clockwise rotary and the deeper ones, counterclockwise, although they are all rather rectilinear. The major axes of the K_1 ellipses at Easter Island (2-4 cm s^{-1}) are larger than those from the central valley record (2-3 cm s^{-1}) and do not undergo a progressive trend with depth, but instead show a maximum amplitude near 50 mab. The ellipse orientation rotates clockwise with increasing depth, and becomes aligned along the valley.

3.2.2 Semidiurnal tidal flow

Current ellipses for semidiurnal tidal flows are also shown in Figure 3.2 (lower panels). At the central valley site, measured semidiurnal flows are very rectilinear high in the valley, and become more rotary and aligned with the valley at increasing depth. The major axes are comparable to diurnal flows at this site and decrease gradually in

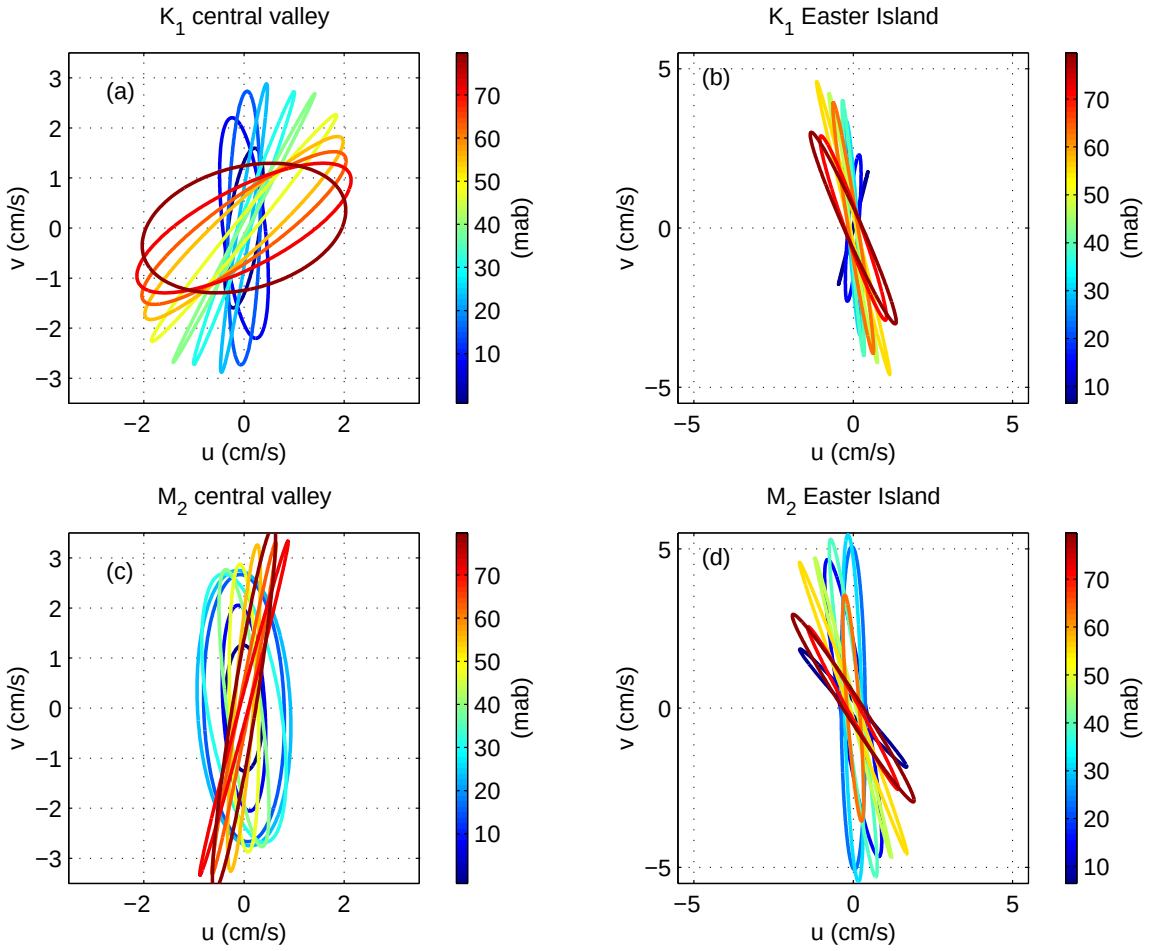

Figure 3.2: Observed tidal current ellipses in *across-* (u) and *along-valley* (v) coordinates for the diurnal (top panels) and semi-diurnal (bottom panels) frequencies from the central valley (a), (c) and Easter Island (b), (d) records. Ellipses are plotted at 6.5-78.5 mab, in intervals of 8 m. The central valley record also includes an ellipse at 0.5 mab from the MAVS data. Blue corresponds to levels closer to the bottom. Note change of scale in (b) and (d).

magnitude with increasing depth, and more rapidly in the bottom 15 meters. At Easter Island, the ellipses are rectilinear and predominantly aligned with the axis of the valley at depth. At this location, the semidiurnal flows are somewhat stronger (2-5 cm s^{-1}) than at the central valley site (2-4 cm s^{-1}).

A quantitative summary of vertical trends in the along- and across-valley flow at

the central valley site is shown in Table 3.1. A significant increase of the along-valley component and a significant decrease of the across-valley component with increasing depth is apparent for the diurnal tidal ellipses. In contrast, the along- and across-valley components of the major axes of the semidiurnal current ellipses at this site do not show a decrease or increase with depth within the measurement error.

Table 3.1: Along- and across-valley components of the major axis of tidal current ellipses in cm s^{-1} in the central valley site at two heights (mab) above the bottom. The errors are based on linear estimates at the 95% confidence level.

	K_1		M_2	
mab	Along	Across	Along	Across
78.5	0.5 ± 0.6	2.0 ± 0.4	3.7 ± 1.1	0.6 ± 1.1
22.5	2.9 ± 1.0	0.5 ± 0.7	2.8 ± 0.6	0.1 ± 0.4

3.2.3 Record-mean flow

Record-means of velocity were calculated by averaging the detided time-series over the length of the record (4.2 days for the central valley site, and 4.8 days for Easter Island). Standard (95% confidence level) errors of the mean Cartesian velocities were estimated using the number of independent samples or effective degrees of freedom obtained by dividing the length of the record by the autocorrelation timescale, as discussed in Emery and Thomson (1998). These values were then propagated to yield errors for mean speed and direction. Errors estimated in this manner from both 30- and 5-minute ensemble-averaged, detided time-series were essentially the same. The record-mean speed and direction at the central valley site are shown in Figure 3.3. The magnitude of the mean flow intensifies with depth down to 15 mab, reaching a maximum speed of $\sim$ 5 cm s^{-1}; below this level, it decreases. The orientation of the mean velocity vector becomes more along-valley with depth although only

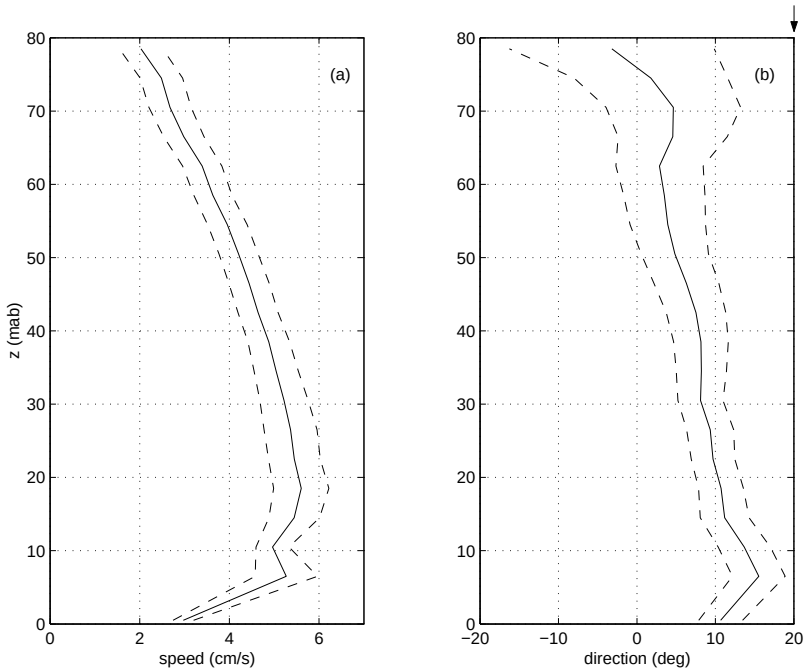

Figure 3.3: Profiles of the (a) speed and (b) direction (measured clockwise from north) of the record-mean velocity vector in the central valley. Dashed lines are the error bars at the 95% confidence level. The record at 0.5 mab corresponds to the MAVS deployment. Ridge axis strikes 020°N (marked by the arrow at the top).

marginally. In contrast, at the Easter Island site (Figure 3.4), record-mean speeds are in general smaller than at the central valley, and they decrease to ~ 1 cm s^{-1} with depth for heights greater than 20 mab. Below this level, mean speeds are amplified rapidly, reaching ~ 4 cm s^{-1} at 7 mab. The orientation of the mean flow changes dramatically with depth, being parallel to the valley below 20 mab and rapidly turning 120° clockwise with height to a predominantly across-valley orientation.

3.3 Is the diurnal velocity spiraling due to bottom friction?

The spiraling of the diurnal ellipses (counterclockwise with depth) for the central valley record (Figure 3.2(a)) seems, in principle, consistent with time-dependent Ekman dynamics where flow turns in the direction of the pressure gradient force. If this were

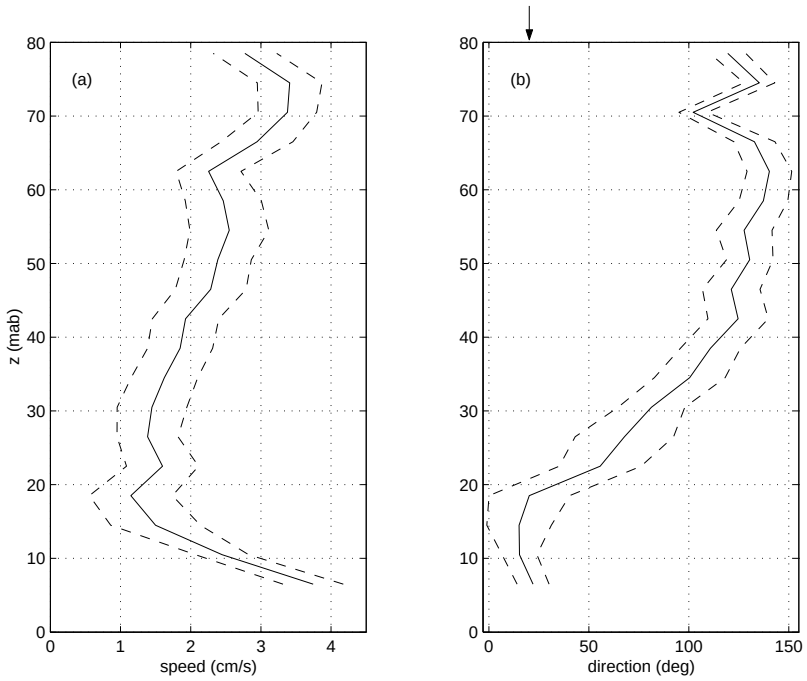

Figure 3.4: Profiles of the (a) speed and (b) direction (measured clockwise from north) of the record-mean velocity vector in Easter Island (MEF). Dashed lines are the error bars at the 95% confidence level. Ridge axis strikes 020°N (marked by the arrow at the top).

the case with our data, the tidal ellipses would begin veering where the flow feels the frictional boundary layer. Although a thickness of about 15 m has been assigned to the Ekman layer, it should be noted this applies to the steady case. An Ekman layer in an oscillating flow, has a different thickness for the clockwise and counterclockwise rotary components of the flow (Weatherly et al., 1980), the larger being the clockwise, $\delta_+ = 0.4u_{\star+}/|\omega - f|$, where $u_{\star+}$ is the friction velocity associated with the rotary tidal current. However, for this Ekman layer to be 80-m thick, the value of $u_{\star+}$ would have to be 0.9×10^{-3} m s^{-1}, much larger than the measured $u_\star$, 0.4×10^{-3} m s^{-1}. Furthermore, a simple Ekman layer model with constant eddy viscosity shows tidal ellipses decreasing in size with depth, as expected for flow decelerated by friction (Weatherly et al., 1980). Contrary to this model, the observed diurnal tidal flow at the central valley does not decrease in magnitude with depth until 20 mab, more consistent with the estimated Ekman-layer thickness. Therefore, a frictional model does not explain the turning of the diurnal tidal ellipses observed above 20 mab, which motivates the use of an inviscid model described in the next section to interpret the observations.

3.4 Model of baroclinic subinertial flows in the axial valley

3.4.1 Model equations

An oscillating barotropic flow encountering topography in a stratified fluid will drive baroclinic motion by inducing a vertical velocity and displacing isopycnals. For superinertial frequencies, internal gravity waves that radiate from topography dominate the response; for subinertial frequencies, baroclinic wave motions are trapped to the topography (Gill, 1982). In this section, a model is presented that captures the dynamics of baroclinic subinertial flow in an idealized axial valley.

In the model, an oscillatory rectilinear barotropic background flow is imposed with

across- (U) and along-valley (V) components

$$\begin{aligned} U &= \Re\left[-A\sin\theta e^{i\omega t}\right] \\ V &= \Re\left[A\cos\theta e^{i\omega t}\right], \end{aligned} \tag{3.1}$$

where $\omega < f$ is the frequency of the oscillation, A the amplitude of the background current and θ the angle of the barotropic flow direction relative to the orientation of the idealized valley (measured positive counterclockwise from the axis of the valley). In the model, the y-axis (x-axis) is directed *along-valley* (*across-valley*). Following Lavelle and Cannon (2001), the barotropic flow is maintained by imposing a spatially uniform, barotropic, oscillatory force with components

$$\begin{aligned} F_x &= \Re\left[\left(-i\omega A\sin\theta - fA\cos\theta\right)e^{i\omega t}\right] \\ F_y &= \Re\left[\left(i\omega A\cos\theta - fA\sin\theta\right)e^{i\omega t}\right], \end{aligned} \tag{3.2}$$

designed to counteract the Coriolis force in order to keep the imposed barotropic flow rectilinear. It is assumed that the axial valley bathymetry defined by $z = -h(x)$ varies only in the cross-axis direction. The water column is stratified with a laterally invariant, background density field $\bar{\rho}(z)$ characterized by a buoyancy frequency $N^2(z) = -(g/\rho_o)d\bar{\rho}/dz$ (where g is the gravitational acceleration and ρ_o is a reference density). Parameter values are chosen to represent the environment at Endeavour Ridge at 48° N. The N^2 profile used in the model is based on a density profile from a CTD cast taken 18 km west of Endeavour Ridge and best fit in the depth range of 1200-2400 m with the linear function $N^2(z) = \alpha z + \beta$, where $\alpha = 3.9 \times 10^{-9}$ s^{-2}m^{-1} and $\beta = 9.7 \times 10^{-6}$ s^{-2}. The Coriolis frequency used in the model is $f = 1 \times 10^{-4}$ s^{-1}.

The model is linear, inviscid, and hydrostatic, with governing equations:

$$\frac{\partial}{\partial t}(U+u) - f(V+v) = -\frac{1}{\rho_o}\frac{\partial p}{\partial x} + F_x \tag{3.3}$$

$$\frac{\partial}{\partial t}(V+v) + f(U+u) = F_y \tag{3.4}$$

$$0 = -\frac{1}{\rho_o}\frac{\partial p}{\partial z} + b \tag{3.5}$$

$$\frac{\partial b}{\partial t} + N^2 w = 0 \tag{3.6}$$

$$\frac{\partial u}{\partial x} + \frac{\partial w}{\partial z} = 0 \tag{3.7}$$

where (u, v) are the components of the baroclinic velocity, p is the baroclinic pressure field, $b = -g\rho'/\rho_o$ is the buoyancy ($\rho' = \rho - \bar{\rho}$), and baroclinic variables are assumed not to vary in the y-direction. Combining equations 3.3-3.6, and introducing a streamfunction

$$\psi = \tilde{\psi}(x, z)e^{i\omega t}, \tag{3.8}$$

a single equation for the baroclinic flow in the across-valley, vertical plane ($u = \partial\psi/\partial z, w = -\partial\psi/\partial x$) can be derived, yielding

$$(f^2 - \omega^2)\frac{\partial^2\tilde{\psi}}{\partial z^2} + N^2\frac{\partial^2\tilde{\psi}}{\partial x^2} = 0. \tag{3.9}$$

The driving of the baroclinic flow by the barotropic current is a consequence of the no-normal flow boundary condition at $z = -h(x)$:

$$\frac{\partial\psi}{\partial x} = \left(U + \frac{\partial\psi}{\partial z}\right)\frac{dh}{dx} \quad \text{at} \quad z = -h(x). \tag{3.10}$$

Equation 3.9 is solved numerically subject to boundary conditions (3.10) and $\partial\psi/\partial x = 0$ at $z = 0$, the details of which are outlined in the appendix. The baroclinic, along-valley velocity can be derived from (3.4)

$$v = \Re\left[i\left(\frac{f}{\omega}\right)\frac{\partial\psi}{\partial z}\right]. \tag{3.11}$$

In the next section, the solution to (3.9) will be analyzed for an idealized bathymetry corresponding to a ridge with a rift valley that splits the crest.

3.4.2 Ridge with a rift valley configuration

The ridge with a rift valley is defined by the bathymetry

$$h = H - \left(h_r - \Delta h \exp\left[- \left(\frac{x}{L_v} \right)^2 \right] \right) \exp\left[- \left(\frac{x}{l} \right)^2 \right],$$

where $H = 2400$ m, $h_r = 335$ m, and $l = 3000$ m are the base depth, height, and half-width of the ridge, respectively; and $\Delta h = 135$ m and $L_v = 500$ m are the nominal depth and half-width of the valley, respectively. These parameter values result in a bathymetry that is an idealized, yet reasonable representation of the Endeavour ridge and valley. The model solution for a barotropic flow of amplitude $A = 0.02$ m s^{-1}, $\theta = 50°$, and oscillating at the diurnal frequency is discussed in this section. This flow is based on the observations of depth-independent diurnal tidal currents measured away from the ridge (Allen and Thomson, 1993) and barotropic tides from the OSU regional tidal inverse model (Egbert et al., 1994; Egbert and Erofeeva, 2002) for the deployment period of the central valley site ADCP. When the barotropic flow encounters topography, vertical velocity is induced that displaces isopycnals as shown in Figure 3.5. This figure illustrates how a westward flow causes upwelling (downwelling) on the eastern (western) flank of the ridge, tilting isopycnals downward to the west at some height above the ridge crest. In the valley the situation is reversed: downwelling (upwelling) occurs on the eastern (western) wall, resulting in isopycnal slopes of different sign to those above the ridge crest. For subinertial motions, the across-valley tilt of isopycnals results in an along-valley flow in near-geostrophic balance. In this way, the evolution of the along-valley flow is ultimately determined by the across-valley flow. The amplitudes of the across- and along-valley flows are shown in Figure 3.6.

Above the ridge (Figures 3.6(a) and (b)) the amplitude of both along- and across-valley flow is intensified as the ridge crest is approached, but for different reasons. The across-valley flow is intensified as a result of the compression of streamlines (ψ) directly above the ridge crests. As discussed in Lavelle and Cannon (2001), the

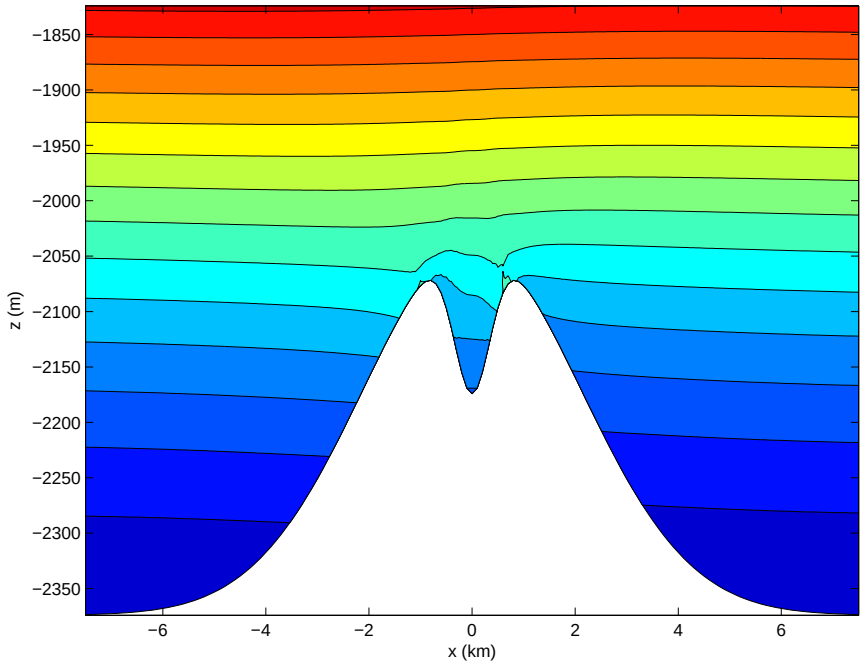

Figure 3.5: Isopycnal surfaces at a time of maximum vertical displacement after a period of westward flow associated with a barotropic diurnal oscillation with $A = 2$ cm s^{-1} and $\theta = 50°$. The contour interval is 4.5×10^{-3} kg m^{-3}.

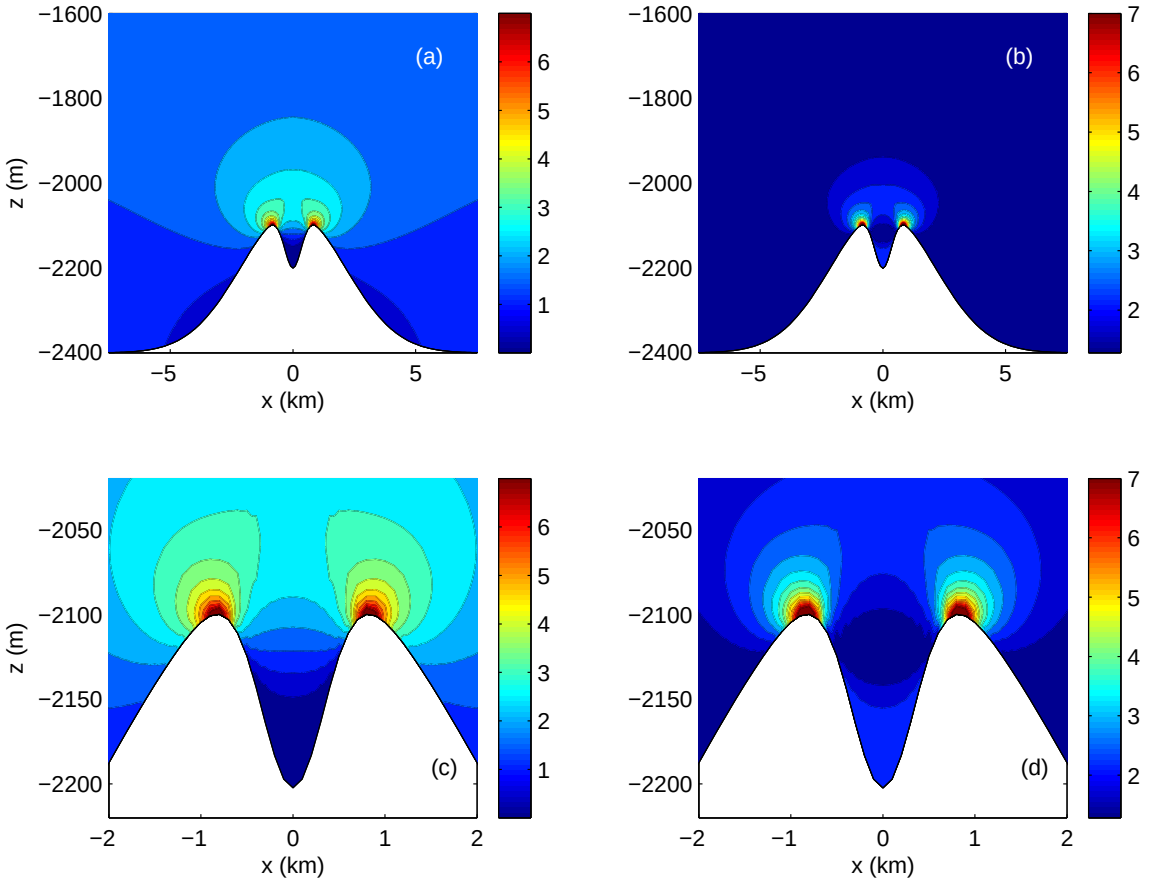

Figure 3.6: Amplitude of the across- (a),(c) and along-valley (b),(d) flow (in cm s^{-1}) forced by a diurnal barotropic flow with amplitude $A = 2$ cm s^{-1} directed at an angle $\theta = 50°$. The bottom panels are magnified versions of (a) and (b).

along-valley flow intensification is a consequence of the geostrophic shear associated with the baroclinic pressure-gradient caused by distortion of isopycnals over the ridge crests, shown in Figure 3.5. Within the axial valley, the amplitude of the across-valley component decreases with depth (Figure 3.6(c)) as the streamlines increase their separation in the valley. The amplitude of the along-valley flow (Figure 3.6(d)) shows a minimum in the axial valley at the level where the baroclinic pressure-gradient changes sign, a consequence of the effect the opposite signs of the ridge and valley slopes have on isopycnal displacement. The height of this level is determined by the relative slopes of the ridge and valley bathymetries. Below this level, the along-valley flow intensifies, reflecting the geostrophic shear of the reversed isopycnal tilt within the valley. In general, the vertical scale of a subinertial flow is determined by the Prandtl depth $\delta_P = \sqrt{f^2 - \omega^2}L/N$, where L is the characteristic horizontal length scale of the flow (Gill, 1982). For example, for lower forcing frequencies, the penetration height of the intensified flow over the ridge is increased (as seen in the numerical model of Lavelle and Cannon (2001)), whereas for stronger stratification it is more confined in the vertical. It can also be shown that the strength of the across-valley flow increases with decreasing Prandtl depth. Therefore, for higher stratification, flow intensification over the ridge is more pronounced, in agreement with the findings of Allen and Thomson (1993). In addition, while the strength of the across-valley flow depends on ω, this dependence is weaker for lower frequencies of oscillation, consistent with the results of Lavelle and Cannon (2001).

The correlation of the along- and across-valley flows is demonstrated by current ellipses shown in Figure 3.7. Above the ridge, diurnal current ellipses are amplified and become more clockwise rotary with proximity to the crest (Figure 3.7(a)), in agreement with the $1\frac{1}{2}$-layer analytical model of Allen and Thomson (1993) and the numerical model of Lavelle and Cannon (2001). Within the valley, the eccentricity of the ellipses decreases with depth until the level at which the baroclinic pressure-gradient equals zero and the flow reverts to the imposed rectilinear barotropic current

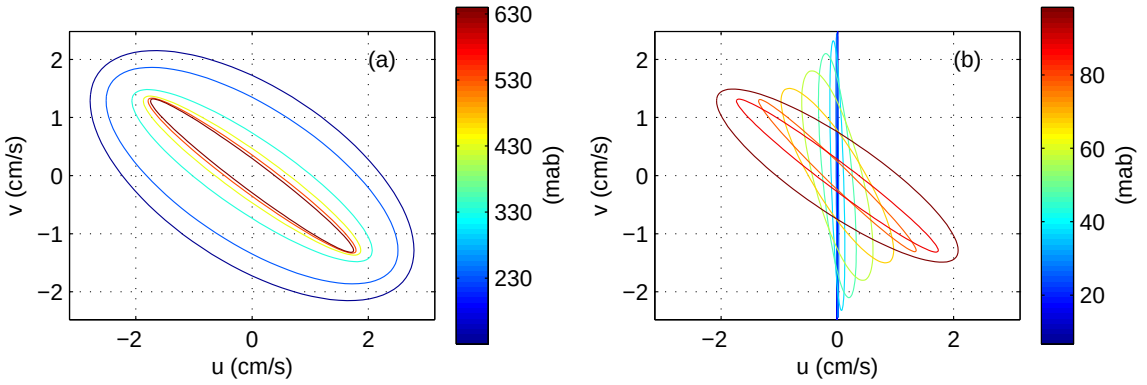

Figure 3.7: Current ellipses associated with the solution shown in Figure 3.6 at $x = 0$ for depths (a) above the valley , i.e. 130-630 mab, in increments of 100 m; and (b) within the valley, i.e. 7-97 mab, in increments of 10 m. Blue corresponds to greater depths.

(Figure 3.7(b)). Below this level, the across-valley flow continues to decrease, while the along-valley flow intensifies, as described above, and the ellipses become counter-clockwise rotary, consistent with the vortex stretching argument posed by Allen and Thomson (1993) if a valley, rather than a ridge topography, is considered.

The dependence of the solution on the orientation angle θ and frequency of forcing of the barotropic flow is illustrated in Figure 3.8. For all values of these parameters, current ellipses become more elongated and aligned with the valley as they approach the bottom. This behavior results from the two opposing tendencies of the across- and along-valley flows within the valley described above. While the across-valley flow decreases with depth, the along-valley flow is intensified near the bottom, below the level where the baroclinic pressure-gradient is annulled. The sense of rotation of the major axis of the ellipse with depth depends on θ. For $0° < \theta < 90°$, the major axis rotates clockwise with depth while, for $90° < \theta < 180°$, it rotates counterclockwise. The orientation angle also affects the degree of intensification; the more perpendicular the direction of the barotropic flow is to the axis of the valley, the greater the intensification. In addition, decreasing the forcing frequency lengthens the time over which

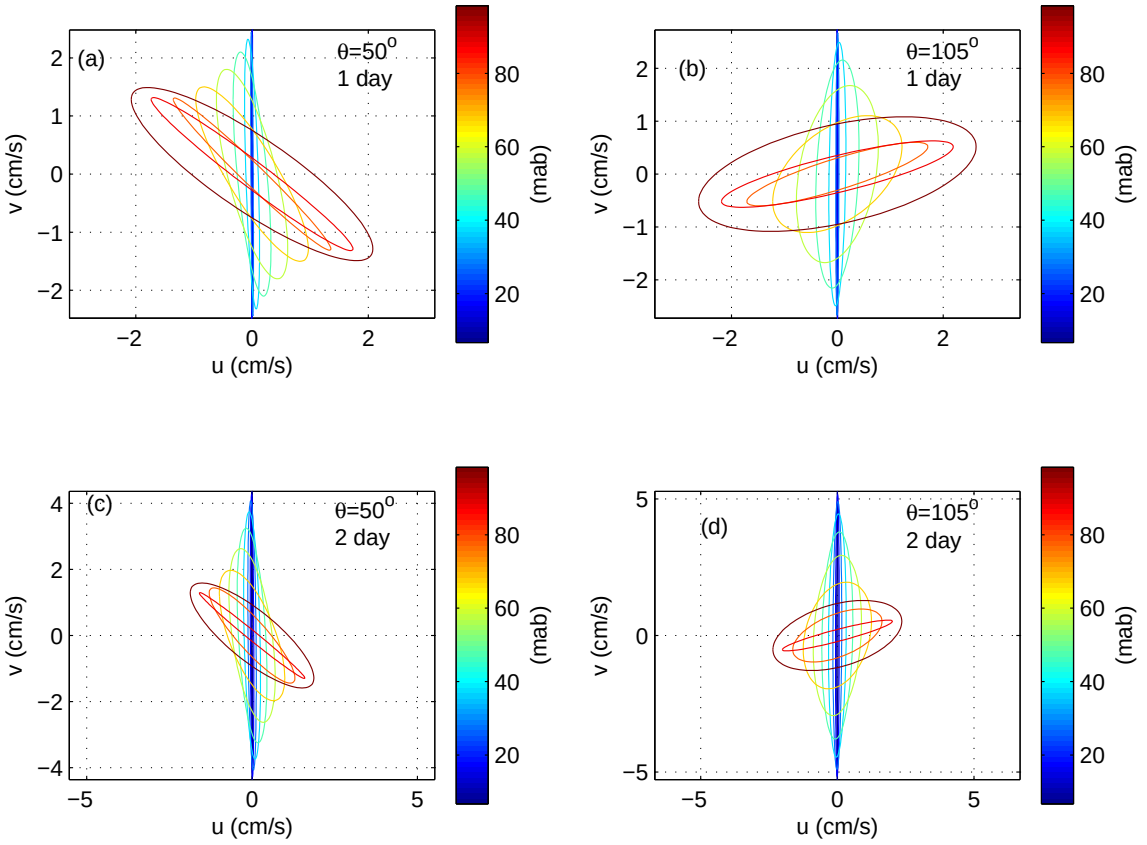

Figure 3.8: Current ellipses at $x = 0$ for a barotropic flow directed at an angle $\theta = 50°$,(a) and (c), and $\theta = 105°$, (b) and (d), relative to the valley axis, and oscillating at frequencies corresponding to one, (a) and (b), and two days, (c) and (d). The ellipses are shown at vertical levels from 7 (dark blue) to 97 mab in intervals of 10 m.

isopycnals are displaced and hence results in stronger along-valley near-geostrophic flows (Figure 3.8). The described dependence of the degree of flow intensification on angle of incidence and period of the forcing was also seen by Lavelle and Cannon (2001) for the case of a ridge without an axial valley.

3.4.3 Across-valley flow within the valley

In order to further explore the characteristics of the across-valley flow for depths within the valley a simple bathymetry of a valley is chosen of the form

$$h = H + \Delta h \exp\left[-\left(\frac{x}{L_v}\right)^2\right],$$

where Δh and L_v are the depth and half-width of the valley. The choice of a topography without a ridge is necessary to isolate the effect of the valley width on the solution while keeping the other parameters constant. The model solution for a barotropic flow of amplitude $A = 0.02$ m s^{-1}, $\theta = 50°$, and oscillating at the diurnal frequency is shown in Figure 3.9 for two valleys with the same depth, $\Delta h = 100$ m, and different widths. The most outstanding features of the solution are the larger penetration depth of the across-valley flow for the wider valley (consistent with the Prandtl depth scaling discussed above) and its decreased magnitude in the valley. Stagnation of the across-valley flow is more pronounced in the narrow valley, and, in general, is most pronounced when the valley width is smaller than the internal radius of deformation. For oscillating flows this is $L_r = N\Delta h/\sqrt{(f^2 - \omega^2)}$, a result derived from the scaling of the relative strengths of the baroclinic and barotropic flows, i.e. $u/U \sim \Delta h/\delta_P = L_r/L_v$. For this example, $L_r \sim 1800$ m, substantially larger than the width of the valley for the topography shown in (a), which is more representative of the axial valley at Endeavour. It should be noted that a reduction of the stratification, a decrease in the frequency of oscillation of the flow and conversely, an increase in the Coriolis frequency, would make the valley less of a shadow zone for cross-flow. As a result of the stagnation of the across-valley flow, the along-valley

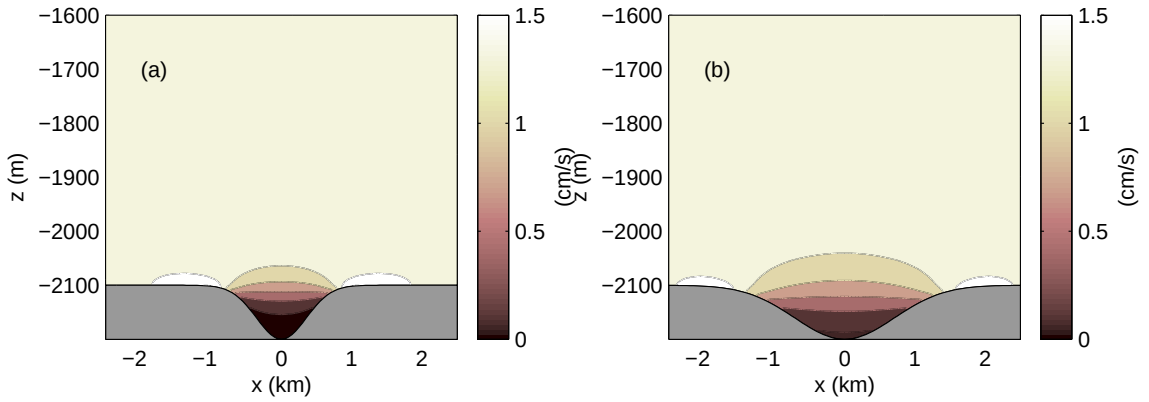

Figure 3.9: Amplitude of the across-valley current, i.e. $|\partial\tilde{\psi}/\partial z|$, driven by a barotropic flow oscillating at the diurnal frequency for two valley widths, (a) $L_v = 500$ and (b) 1000 m. The contour interval is 0.3 cm s^{-1}.

component of the Coriolis force is weakened in the shadow zone and cannot balance the along-valley barotropic force F_y or any along-valley pressure gradient that may exist (and not included in this two-dimensional model). Hence, an along-valley flow is accelerated.

3.5 Discussion

3.5.1 Further considerations of diurnal currents within the axial valley

Flow measurements taken in the middle of the axial valley of the Endeavour Ridge with fine vertical resolution over the bottom 80 meters show that the diurnal tidal currents intensify and become parallel to the axis of the valley with depth (Figure 3.2(a), Table 3.1). On the other hand, semidiurnal tidal currents generally become more aligned with the valley at depth, but are not amplified (Figure 3.2(c), Table 3.1). Although our measurements are relatively short (4-5 days), these observations are consistent with another set of longer records taken in the summer of 2000 (Veirs, 2003), albeit only at a single depth within the axial valley. These previous measurements include one current meter (FM-N15) deployed 1 km north of MEF at 15 mab (2161-

m depth) that recorded for 4.5 months; and another one (FM-S50) deployed 1 km south of MEF at 50 mab (2142-m depth) that recorded for 2.5 months. Veirs (2003) notes, from velocity power spectra, that FM-N15 has enhanced diurnal energy relative to FM-S50, which he believes could be a consequence of the greater topographic constriction of the valley at the northern site. However, he also notes that both records have equivalent semidiurnal energy, which raises the question of why the semidiurnal flows are not affected by the lateral valley constriction. It is possible that this is another observation of intensified diurnal tidal current closer to the bottom. Further, Cannon and Pashinski (1990) note a bottom intensification of the diurnal and 4-day currents within the rift valley at the southern Juan de Fuca Ridge and, in particular, in the topographically confined Axial Sill, although the latter could be evidence of hydraulic control, as described by Thurnherr and Richards (2001) at Rainbow Sill.

A two-dimensional model of subinertial oscillations over a valley explains the two basic features of the diurnal tidal flows measured at the central valley site: (a) intensification of along-valley flow and (b) attenuation of across-valley flow with depth. In agreement with our observations, current ellipses of the model solution have high eccentricity above the valley and low eccentricity deep within the valley. However, there are differences between model and observations. For example, the uppermost level observed by the ADCP (approximately 80 mab) is oriented at 105° counterclockwise from along-valley, instead of at the expected 50° value of the barotropic tide. In addition, while observed ellipses are clockwise rotary, the model yields counterclockwise rotary ellipses in the valley below the level where they revert to the imposed barotropic flow. However, it is important to note that the rotary sense becomes more uncertain as the ellipses become more rectilinear. The observed counterclockwise rotation of the principal axis with depth is consistent with the model physics acting upon this uppermost diurnal current (Figure 3.8(b)). Nevertheless, it is apparent that additional forcing mechanisms exist to drive diurnal oscillations apart from the presumed

barotropic force used in the model. The most likely additional forcing mechanism that is not captured by the two-dimensional model is a baroclinic pressure-gradient in the along-valley direction. An along-valley baroclinic pressure gradient oscillating at the diurnal period could result from along-valley variations in topography or from advection by diurnal flows of an inhomogeneous along-valley density field. The model also neglects diapycnal mixing. Bottom intensified dissipation has been observed to vary with the tidal cycle over the Mid-Atlantic Ridge flanks (e.g., St. Laurent et al., 2001). Vortex stretching/squashing associated with diapycnal upwelling/downwelling could affect the rotary character of the current ellipses. Finally, the observed tidal diurnal velocities also decrease rapidly in the bottom 15 meters, which is not captured by the inviscid model, but is consistent with the Ekman-layer thickness based on bottom boundary-layer turbulence measurements. Neglecting bottom friction did not significantly affect the solution in the model by Lavelle and Cannon (2001) except for the bottom-most levels, as to be expected here too.

3.5.2 Additional considerations for lower frequency flows

It has been proposed with this study that the valley is a shadow zone for subinertial across-valley flows, owing to the valley's small width relative to the internal Rossby radius. This has important implications for the dynamics of steady currents. Stagnation of the across-valley flow implies that any existing along-valley pressure-gradient cannot be balanced geostrophically, resulting in a direct acceleration of the along-valley flow. The model predicts a more pronounced stagnation deeper in the valley, and consequently, an intensification of the along-valley flow with depth. Record-mean velocities at the central valley site are characterized by weak across-valley flows and along-valley flows that become stronger with depth (with the exception of the bottom 15 m or bottom frictional layer), in agreement with the proposed model. Although these observations were made over a short period of 4 days and therefore could reflect an episodic event, point measurements of mean flow within the valley by Veirs

(2003) and Thomson et al. (2003) spanning the summer of 2000 and 2001, respectively, support a prevailing flow that is predominantly oriented along the valley and is also intensified with depth.

With the model physics in mind, the observations of flow within the valley suggest that there exists an along-valley pressure-gradient that drives the prevailing flow. This is an analogous situation to that found in the equatorial and coastal undercurrents, where the presence of the equator and coastline, respectively, results in a weak Coriolis force that is unable to balance a downstream pressure-gradient (Tomczak and Godfrey, 1994). The downstream pressure gradients that drive the equatorial and coastal undercurrents are associated with sloping of isopycnal surfaces in the downstream direction (Philander, 1990; McCreary, 1981). Hydrographic surveys in the axial valley of the Endeavour Ridge (not concurrent with the observations of flow presented here), between the Main Endeavour and High Rise vent fields, indicate that isopycnals slope downwards from south to north along the valley (see Section 4.3). The baroclinic pressure-gradient associated with this isopycnal tilt is in the right sense to drive the bottom-intensified northward mean flow. Downstream velocities in equatorial and coastal undercurrents are also in geostrophic balance with the cross-stream baroclinic pressure-gradient. In the valley, the record-mean flow is more intense near the bottom. Such vertical shear implies that, if the along-valley mean currents were geostrophic, water should be denser on the eastern wall of the valley, as is observed in across-valley hydrographic sections (see Section 4.3).

While the flow associated with the diurnal along-valley pressure gradient is halted and reversed by a driving force of the opposite sign, a much lower frequency along-valley pressure gradient would need to be balanced by a retarding force. Studies of the Equatorial Undercurrent attribute the retarding force to the cumulative effect of four terms: friction associated with the vertical turbulent fluxes of momentum, horizontal and vertical advection of momentum by mean flows, and horizontal eddy flux of momentum (Dillon et al., 1989). Friction opposing the equatorial undercurrent

is provided by the wind-stress and is the dominant retarding force (Yu and McPhaden, 1999). In our case of an axial valley, an external retarding force results from bottom stress. From bottom turbulence measurements, the frictional force (per unit mass) can be estimated as $\tau_b/\rho_o H \sim u_\star^2/H \sim 3\times10^{-7}$ m s^{-2} (τ_b is the bottom stress, $u_\star = 0.004$ m s^{-1} is the friction velocity, and $H = 50$ m is the vertical length scale of the flow). The along-valley density-gradient from hydrographic sections is $\partial\rho/\partial y \sim 5\times10^{-6}$ kg m^{-4}. A rough estimate for the pressure-gradient force associated with this density-gradient is $(g/\rho_o)(\partial\rho/\partial y)H \sim 2\times10^{-6}$ m s^{-2}, about an order of magnitude stronger than bottom friction. Therefore, additional mechanisms should be counteracting the along-valley baroclinic pressure-gradient force.

The unique characteristics of the axial valley that distinguish it from equatorial and coastal regions, namely, the presence of hydrothermal vents and confining valley sidewalls that constrain the currents, may provide some insight into the physical mechanisms responsible for balancing the pressure-gradient. Buoyant plumes result in an upward flux of mass and enhanced turbulence. Mixing of momentum by this buoyancy-driven turbulence may provide a frictional force to slow down the mean flow. In addition, the upward mass flux concentrated in the rising plumes may be returned in a larger-scale flow pattern of subsidence (Speer, 1989). As the momentum of the mean flow decreases with height in the valley, advection of low momentum downwards by the subsidence could also play a role in the balance. Drag associated with the valley sidewalls may also slow down the mean flow; however it needs to be transmitted to the center of the valley somehow, perhaps through lateral eddy fluxes of momentum. Finally, tidal interaction with topography and billowing rising plumes, are likely to generate internal waves, which, upon breaking, mix momentum, resulting in a frictional force. It is clear that further measurements in the axial valley are needed to elucidate which of these or other mechanisms can balance the along-valley pressure-gradient.

3.5.3 Currents near a high-temperature vent field

If the currents at the central valley site provide some clues about the dynamics of subinertial flows in a valley, the flows measured at Easter Island hydrothermal vent site may reflect how these dynamics can be altered or superseded by buoyant and/or local topographic effects. Both records correspond to periods in which the diurnal inequality was more pronounced during the first half (and slightly more so for Easter Island). Based on results from an inverse tidal model (Egbert et al., 1994), tidal flows were stronger during the period of the Easter Island deployment, which may explain the larger velocities at that site. But rather than attribute the discrepancy in these two records to a difference in tidal cycles, it is more likely related to the quite different settings of the deployment locations. While the central valley site lay at some distance from topographic or buoyant flow disturbances, the deployment location at Easter Island was in close proximity to both active hydrothermal vents (buoyant plumes and sulfide structures) and to the western valley wall. It is not surprising therefore that the subinertial and mean flows observed at Easter Island are not completely consistent with the model results presented in section 4. Tidal flows at Easter Island are very rectilinear at all depths within the valley, and oriented mostly along-valley (except at the top of the valley), likely a consequence of the nearby topographic constraints. The amplitude of the tidal flow does not intensify with depth. The record-mean ($\sim$ 5 days) velocity at Easter Island does show an intensification in the bottom 15-20 m, with a predominant along-valley direction. However, above 20 m, the record-mean speed decreases with depth and the direction exhibits a rapid spiraling going from a south-east orientation at the top to an along-valley orientation at depth (Figure 3.4). Vent structures in this area are up to 20-m high, with an average height of 7$\pm$2 m, according to Veirs (2003). It is possible that the behavior of the record-mean flow above 20 mab is influenced by buoyancy-forced circulation in the near-field of plumes located south to southeast of the deployment site or by the sulfide edifices themselves.

There is also a step on the western valley wall that coincides with that level (Figure 3.1).

Alternatively, if the flow has a predominant geostrophic component, from a thermodynamic perspective, a spiraling velocity field is associated with the horizontal advection of density

$$\vec{u}_g \cdot \nabla\rho = -\left(\frac{\rho_o f}{g}\right) U_g^2 \frac{\partial\theta_g}{\partial z},$$

where U_g and θ_g are the speed and direction (measured counterclockwise from east) of the geostrophic flow $\vec{u}_g$ (Bryden, 1976). This horizontal advection of density can be balanced by the local rate of change of density as in the case of an eddy passing by the point of observation (e.g. Bryden (1976)), by mixing of buoyancy and/or by vertical advection of density (Schott and Stommel, 1978). Although diurnal tidal currents are expected to have a strong contribution from local acceleration as in the model, lower-frequency flows are expected to be increasingly geostrophic, even within the confines of the axial valley. A frictional ageostrophic component may also be present, as in the undercurrent balance discussed previously. If it is assumed that the record-mean currents shown in Figure 3.4 are predominantly geostrophic, the clockwise rotation of the currents with height over the bottom 60 m would result in a reduction of density at a rate of 1×10^{-7} kg m^{-3} s^{-1}. This rate of change of density is equivalent to the convergence of a heat-flux of $\sim$ 100 W m^{-2} over the bottom 60 m, which would be strong enough to increase water temperatures by 0.04 °C in one day. Spiraling flows have also been observed above the ridge (Franks, 1992; Veirs, 2003). This spiraling may be an indication of horizontal advection of heat, perhaps by anticyclonic eddies that are shed from the neutrally-buoyant plume as demonstrated in laboratory experiments (Helfrich and Battisti, 1991). If this is indeed the case, the rotation of the velocity vector with height could be used to estimate horizontal heat advection to possibly constrain heat budgets in hydrothermal regions.

3.6 Implications for larval dispersal

The transport of planktonic larvae by bottom currents plays a key role in the dispersal potential of vent species that have limited mobility, yet are constantly faced with the challenge of colonizing new sites due to the ephemeral, unpredictable, and highly variable nature of hydrothermal vent systems. Since the highest abundances of these larvae are found close to the bottom and to their vent source communities (Mullineaux and France, 1995) and hydrothermal venting is largely concentrated within the axial valley of the Endeavour Ridge, characterizing the flow patterns in the valley is central to understanding larval dispersal mechanisms and pathways. In addition, it has been suggested that transport by near bottom currents may be a more prevalent larval pathway than entrainment into rising plumes and dispersal within the neutrally-buoyant plume, which is only favored during periods of slack tide (Kim and Mullineaux, 1998).

The findings of the present study regarding currents in the axial valley of the Endeavour Ridge provide evidence that would support near-bottom larval dispersal. First, the vertical structure of the currents results in estimates for lateral displacements that are largest within the bottom 20 m (larger than 10 km in four days), for both the Easter Island and central valley sites (Figure 3.10). This means that larvae, found in abundant numbers close to the bottom, find themselves in relatively large flows and need not rise too high to encounter the strongest flows within the valley. Second, even though the bottom-most record-mean flows are predominantly along-valley, they gradually acquire an across-valley component with height, resulting in the spiraling of the progressive vectors seen in Figure 3.10 (more so at Easter Island than at the central valley). The spiraling with height of the prevailing currents implies that, if the larvae are able to change their position in the vertical, whether by actively adjusting their buoyancy, or passively being entrained into rising plumes or lifted by topographically-induced upwelling, they have the opportunity of being trans-

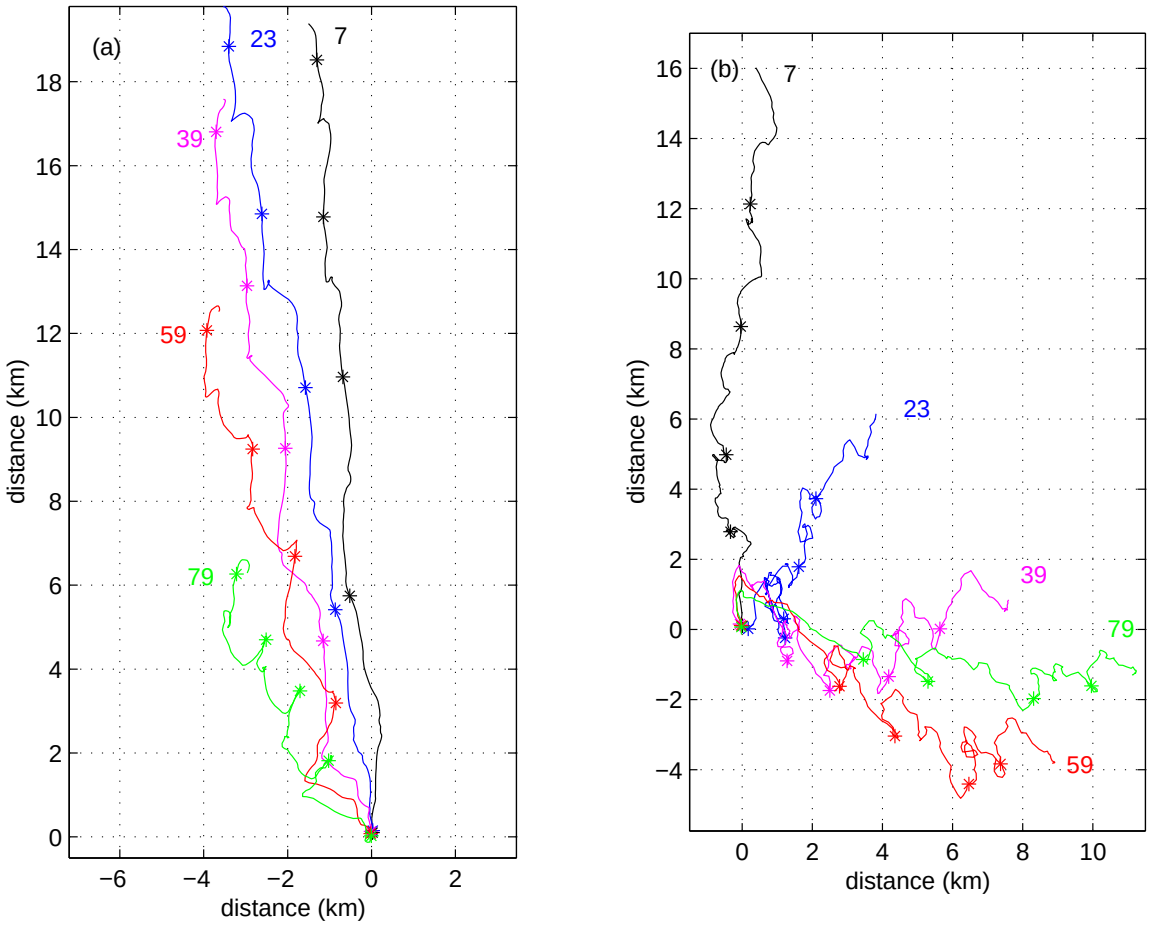

Figure 3.10: Progressive vector diagrams for the ADCP records projected onto across- and along-valley coordinates at (a) the central valley and (b) Easter Island. Stars mark intervals of 1 day. The altitude in meters above the bottom of each record is indicated.

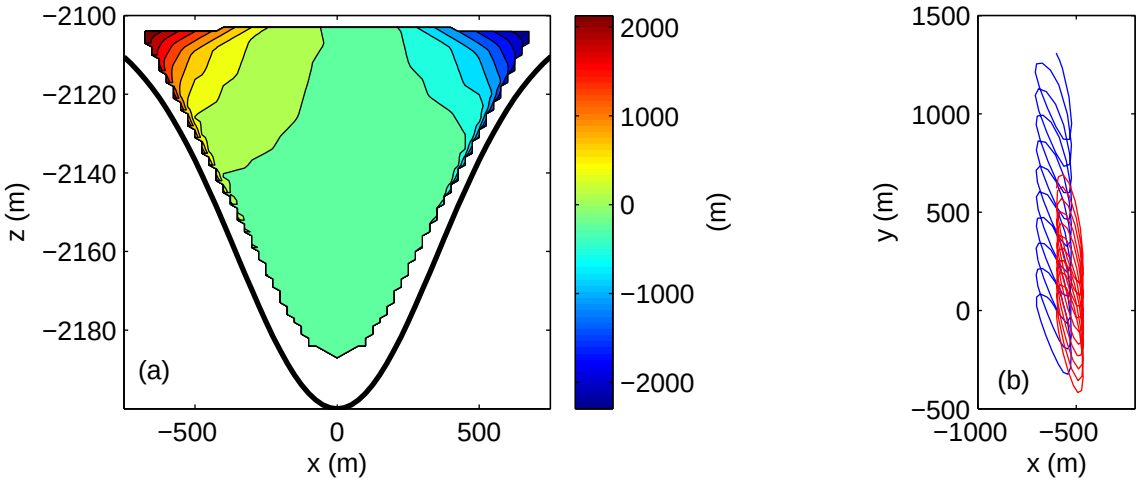

Figure 3.11: (a) Along-valley displacement (in meters) after 10 diurnal tidal cycles of particles released in the valley at peak tide, for the model solution shown in Figure 3.9(a). (b) Trajectories of particles released at $x = -600$ m and $y = 0$ m during peak (blue) and slack (red) tide for the same model solutions.

ported in different directions and potentially cover more terrain, thereby increasing their chances of colonization of suitable habitats.

Thus far, the discussion has focused on the role of the prevailing flow in the transport of larvae. However, oscillatory currents can also lead to net transport if they vary spatially. Such is the case for both observations (Figure 3.2) and model solutions (Figure 3.6) for the diurnal tidal currents, which exhibit strong vertical shear. At the same time, tidal currents impinging on topography can induce vertical velocities. For the case shown in Figure 3.5, vertical motions can uplift isopycnals up to 20 m in the valley. The vertical velocity field displaces particles downward (upward), where they encounter stronger (weaker) along-valley flow, leading to incomplete closure of particle trajectories, analogous to Stokes drift. This mechanism can be illustrated by calculating the Lagrangian trajectories of particles released in the valley using velocities from the model of section 4. The resulting net displacements in the along-valley direction after 10 days are shown in Figure 3.11. The displacements are largest

in regions of both strongest vertical shear (i.e., higher up in the valley) and strong vertical velocities (i.e., valley walls). On the eastern (western) side of the valley, the net transport is southward (northward), a consequence of the phase relation between the vertical velocity and the along-valley tidal velocity. These residual flows are a result of tidal rectification involving a nonlinear interaction between vertical velocity and vertical shear of the oscillatory flow. It is therefore distinct from barotropic tidal rectification (Zimmerman, 1980; Robinson, 1981), which does not account for vertical shear. The largest residual flows (0.002 m/s) generated by this baroclinic tidal rectification are an order of magnitude weaker than the oscillatory tidal flows. Therefore, neglecting this nonlinear effect in the model of section 4 is reasonable. Even though these residual flows are also weak compared to the observed low-frequency flow in the axial valley, they can potentially contribute to dispersal of larvae since tides are a continuous forcing.

Lateral variability of oscillatory flows within the axial valley is likely (for example, owing to local topography or buoyant sources) and can result in open trajectories with a net displacement, similar to the case described above for the vertically sheared tidal flows. Regardless of whether the oscillatory flows vary laterally or vertically, the magnitude of the resulting net displacement is dependent on the phase of the tide at the time of particle release, as seen in Figure 3.11(b). Although speculative, vent organisms could have developed adaptations to make their larvae release synchronous with the tidal cycle, so as to achieve maximum or minimum net displacement, depending on whether dispersal or retention is the best strategy to ensure succession.

In contrast to plume dispersal, where larvae can be exposed to cross-axis flows above the ridge that may transport them into the inhospitable abyss, dispersal within the valley appears to be a less risky pathway. The mechanisms proposed in this section suggest that larval dispersal over multiple kilometers within the axial valley is, from the hydrodynamical point of view, very plausible. The high potential for dispersal that exists within the axial valley is consistent with the findings of uniformly

high abundance of larvae within the Endeavour Segment (Metaxas, 2004). Larvae might not reach sites as distant as through neutrally-buoyant plume dispersal, but the retention of larvae within the axial valley, where the vent fields are found, could ensure a constant supply of recruits to maintain locally established populations.

3.7 Conclusions

Using a 2-D quasi-analytical model for subinertial motions in a stratified, narrow valley, the present study has shown that across-valley flows diminish with depth. The weakened along-valley Coriolis force that results cannot fully balance pressure-gradient forces directed parallel to the valley axis, so that along-valley flows are directly accelerated and intensified with depth. Alignment of the flow with the along-valley direction yields a velocity vector that spirals with depth. Spiraling is commonly associated with Ekman dynamics or geostrophic advection of density, however, the rotation of the velocity vector described above is distinct from these phenomena, since it is not a consequence of friction or heat advection.

The basic properties of the model solution—intensification of along-valley and reduction of across-valley flow with depth—are evident in the vertical structure of observed subinertial flows at a site located in the middle of the axial valley of the Endeavour Ridge. If the physics of the model are applicable in the axial valley, a likely scenario given the fundamental nature of the mechanism, the observed baroclinic, along-valley pressure gradients would directly drive prevailing currents that flow down the along-valley density gradient. Such down-gradient mean currents are observed in the Endeavour axial valley and have also been measured in rift valleys of the Mid-Atlantic Ridge (e.g., Thurnherr et al., 2002; Ferron et al., 1998), indicating that the dynamics described by the model may be generalizable to subinertial flows in other submarine valleys at some distance from their controlling sills. More specifically, any roughly 2-dimensional concave topographic feature (valley, channel, cleft, canyon, trench, etc.) with a geometry, latitude and stratification such that the internal Rossby

radius of deformation is larger than its wall-to-wall width, and where oscillatory currents have periods less than the local inertial period, is likely to create a shadow zone to cross-flow over a significant portion of its cross-sectional area.

A second flow measurement site in the axial valley located within an active hydrothermal vent field and adjacent to the axial valley wall exhibits a vertical structure that does not clearly resemble the model solution. However, the record-mean flow does show a very strong vertical shear in direction and magnitude. Regardless of the physics responsible, these vertical shears and bottom-intensified flows have profound ramifications for the transport of hydrothermal fluid and the dispersal of vent organisms.

In axial valleys, attention has been given to the circulation associated with hydrothermal plumes. The present model, supported by limited observations, suggests that in the absence of plumes currents within the axial valley are far from stagnant and also do not simply reflect the barotropic tide. While hydrothermal plume dynamics add considerable complexity to the picture, the interaction of subinertial background currents with topography alone creates a dynamic and depth-dependent flow environment.

Chapter 4

HYDROGRAPHY AND FLOW IN THE AXIAL VALLEY

4.1 Introduction

In the previous chapters, point measurements and single profiles of currents were used to investigate the processes that control one-dimensional mixing in the bottom boundary layer and two-dimensional flow-topography interactions within the axial valley of a hydrothermally active ridge segment. In this chapter, high-resolution cross- and along-valley sections of temperature, salinity, light transmission, and velocity are used to explore the fully three-dimensional dynamical relations between the flow and hydrography from the plume scale ($\sim$ 100 m) to inter-vent field scale ($\sim$ 2 km).

The dynamics of the oceanic circulation in the axial valley and above the ridge are controlled by various physical processes, including hydrothermal venting, tidal currents, flow-topography interaction, and enhanced mixing. Hydrothermal vents are one energy source for the flow in the valley. Buoyant hydrothermal effluent rises through the stratified water column of the deep ocean, entraining fluid as it ascends. The convergence of fluid into the narrow stem of the rising plume, dilutes the hydrothermal fluid, reducing its buoyancy, and drives a cyclonic circulation about its core (Speer and Marshall, 1995). At some height above the bottom, the buoyancy of the plume equals the buoyancy of the surrounding background fluid. At this level of neutral buoyancy, the hydrothermal effluent diverges, spreading laterally and developing an anticyclonic circulation. This idealized process applies to a single plume in the absence of background current. The entrainment and modification of the background water caused by multiple plumes from different vent fields located along the axial valley can lead to variations in water-column properties over inter-vent field lengthscales.

If inter-vent density gradients are created by such a process, then pressure gradients will be induced that can drive horizontal flows, in analogy with the dynamics of the sea-breeze (Thomson et al., 2005). As described in the previous chapter, the flow that would be induced by such pressure gradients should be greatly influenced by the topography of the ridge and valley. The tides are also an energy source for the flow in the valley and can induce circulations of comparable or greater magnitude than the buoyancy driven hydrothermal flow, which consequently complicate interpretations of the velocity observations. Characterizing the flow and hydrography and assessing the dominant physical processes involved in driving the circulation in the axial valley is the goal of the observational analysis in this chapter. Knowledge of these flow quantities is important for the transport of heat, chemicals, and larvae of vent species, and hence motivates the study.

The observations examined here were made in a 3-km long portion of the Endeavour Segment and cover a depth range that spans the hydrothermally influenced layer (bottom 300 m), from the rise height of high temperature plumes down through the 100-m deep axial valley (figure 4.1). This valley section includes the major vent fields of Main Endeavour and High Rise, which are 2 km distant. These are large vent fields with multiple high-temperature sources each. Between them are a couple smaller fields, Clam Bed and Raven, each with one high-temperature vent and broad areas of diffuse venting. This data set was obtained using a towed CTD/lowered-ADCP (LADCP) package, and hence consists of co-located, synchronous velocity and density measurements. This is in contrast to previous observations made at the Endeavour Segment that typically use single-point current meter data with towed hydrographic measurements to estimate advective heat fluxes from vent fields (e.g. Baker and Massoth, 1987; Thomson et al., 1992; Veirs et al., 2006). Evidence of entrainment and convergent flow around the core of rising plumes has been elusive in previous studies, perhaps owing to their coarse resolution or lack of velocity data. The fine horizontal resolution of the towed profiles ($\sim$100 m) presented in this chapter allows for flow

structures in the near-field of both actively rising and laterally spreading plumes to be captured. In addition, the combined velocity and hydrography along the axial valley provides a unique data set that can be used to quantitatively test models for pressure-driven, along-valley flows.

This chapter is organized as follows. Section 4.2, details the methods of data collection and processing. Section 4.3, describes the hydrographic observations, which are then interpreted in the context of a model of a buoyant plume, presented in Section 4.4. In Section 4.5 sections of velocity are considered. Section 4.6 concludes the chapter.

4.2 Data collection and processing

A Seabird 911-plus CTD-rosette system, which included a 25-cm pathlength Wetlabs CStar transmissometer and an optical backscatter sensor, was employed to collect hydrographic and optical data over the Endeavour Ridge axial valley. The instrument package was towed behind the ship, traveling at a speed of ∼0.2 knots (0.1 m/s), and cycled through the bottom 300 m of the water column at ∼0.5 m/s, yielding a horizontal resolution between casts that ranges from 40 to 200 m, although is typically between 100 and 150 m. Each downcast/upcast pair was completed in ∼20 mins.

The towyos were conducted on tracks along and across the ridge axis, which is oriented 20° east of north. The tracks are shown in figure 4.1 on a bathymetric map of the axial valley at Endeavour Segment, between the large active hydrothermal vent fields of High Rise and Main Endeavour. Towyo surveys 2 and 3 ran across the valley over the vent fields of Clam Bed and High Rise, respectively. The tows started over the vent field, proceeded westbound, then turned back to head eastbound, and finally returned westbound to the starting location, so that water samples could be collected in the hydrothermal plume during the ascent. Each of these surveys lasted a total of 4.8 hours. Towyo survey 4a ran southbound and along-valley from High Rise to Clam Bed in 1.3 hours, while 4b ran eastbound across the valley over Clam Bed for 1.8

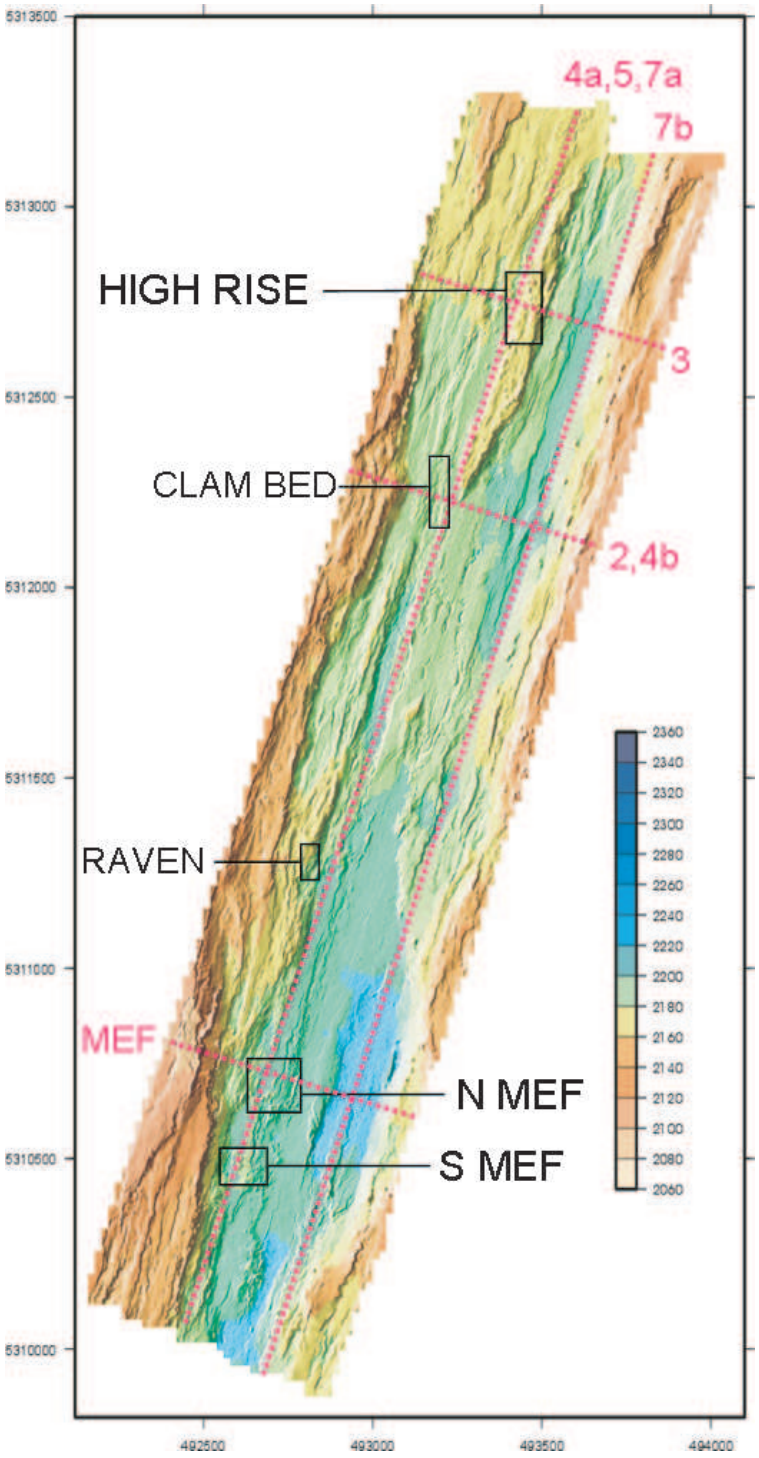

Figure 4.1: Location of the towyo transects on a swath bathymetry map of the axial valley (adapted from Johnson et al. (2002)). Towyo surveys 4a, 5 and 7a were conducted on an along-valley line that runs over the major vent fields, indicated on the map; 7b on a parallel line 260 m to the east; 3 across-valley over High Rise; 2 and 4b across-valley over Clam Bed; and MEF across the valley over North MEF.

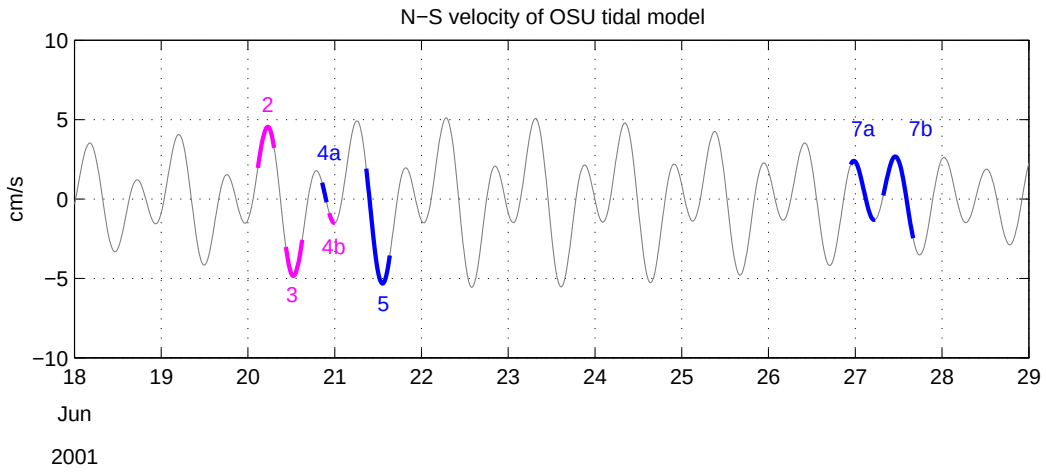

Figure 4.2: Time series of north-south velocity from an inverse tidal model indicating the time intervals when the 2001 towyo surveys were conducted.

hours. Eight hours later, towyo survey 5 ran along-valley and northbound from Main Endeavour to south of Clam Bed, for 6.5 hours. Five days later, towyo survey 7a ran southbound along-valley from High Rise to MEF for 7 hours, returning northbound as 7b along a line 260 m to the east, for 8.6 hours. Towyo survey MEF was conducted across-valley and eastbound over MEF in July 2003. Times and durations for the 2001 towyo surveys are indicated on a time plot of north-south velocity (figure 4.2) derived from an inverse barotropic tidal model (Egbert et al., 1994; Egbert and Erofeeva, 2002) used in previous chapters.

Long baseline acoustic navigation provided position fixes for the CTD-rosette package every 20 s. The tracks obtained were smoothed with a median filter. To produce the transects of water properties, physical data was merged with navigation data and binned on a 5-m grid. Salinity spiking is common at levels where temperature inversions are detected due to the different response times of the temperature and conductivity sensors, but is usually improved by the depth-averaging. Temperature (salinity) anomaly was calculated by subtracting the measured temperature (salinity) from the corresponding value of an off-axis background cast on the same σ_2 surface.

On an isopycnal, temperature and salinity anomalies are proportional to each other because of the quasi-linear local equation of state. Although the temperature and salinity sensors used in the 2001 and 2003 cruises were different, they appear well inter-calibrated. This is not the case for light transmission data, which is plotted with a different scale for the 2003 transect over MEF; however, optical properties are only considered here in relative terms to define hydrothermal plumes.

A self-contained 300-kHz broadband RDI Workhorse Sentinel ADCP was mounted downward-looking on the rosette's frame. The ADCP recorded single-ping acoustic beam velocities and backscatter levels continuously at 2-s intervals, in 4-m bins. Due to the low levels of acoustic scatterers in the deep water, data was usable only in the first 19 bins ($\sim$80 m). Beam velocity data were rotated to Earth coordinates using tilt, roll, heading and magnetic declination values before subtracting the rosette's frame velocity from them to yield water velocity. Velocity data underwent manufacturer's standard quality control during acquisition, but were further screened during processing by rejecting data with an error velocity greater than 0.20 m/s. All velocities measured in a vertical interval of 10 m were averaged together for each downcast-upcast pair, and the new averaged profiles were merged with the navigation data to produce transects of velocity. Although the tilt and roll of the rosette frame were small (typically less than 2°), failure to correct for these inclination angles before subtracting the frame velocity from the ADCP measured velocity introduces an error in the horizontal water velocities that can be up to 2 cm/s, although is generally 1 cm/s or less and is expected to be minimized by averaging the down- and upcast pairs. An additional source of error in the velocity measurements may stem from a bias in the ADCP magnetic compass readings induced by the the steel components of the CTD-rosette frame (Joyce, 1989; Münchow et al., 1995; Hautala et al., 2001) and that is not trivial to determine without bottom-tracking. Despite this potential uncertainty, comparison of the lowered-ADCP and shipboard ADCP velocity data in the top 400 m of the water column (figure 4.3) is very satisfactory. Furthermore, the

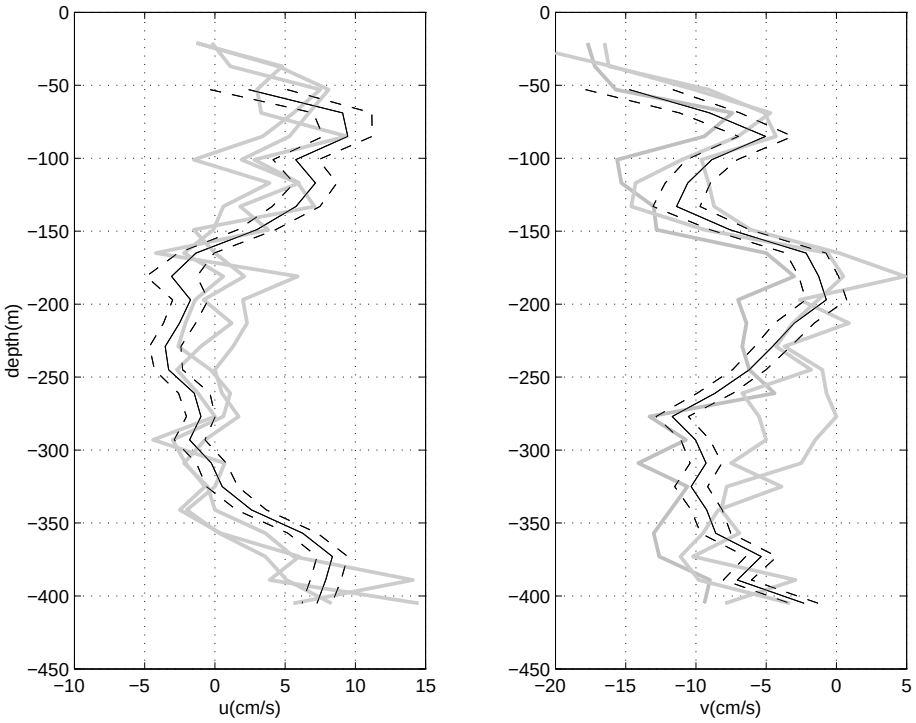

Figure 4.3: Comparison of towed and shipboard ADCP velocity data. The panel on the left (right) shows the east-west (north-south) velocity component. The three profiles shown in thick gray lines correspond to the 150-kHZ RDI shipboard ADCP and are ensemble-averages during the time interval in which the LADCP (data shown in black thin line with error bars) profiled the top 400 m.

focus of this presentation are robust features in the velocity data, i.e., features that have large velocities, with errors less than 4 cm/s and that appear in more than one cast.

4.3 Hydrography and tracer fields

4.3.1 Background density gradient

Although mapped at different times and phases of the tide, along and across-axis transects of temperature, salinity and density, as well as a near-bottom hydrographic survey conducted over several tidal cycles in years 2000 and 2001 (Skebo et al., 2006;

Johnson et al., 2002), consistently show denser water towards the south (figures 4.4i, k, m) and the east (figures 4.4a, c, g) of the axial valley. The only transect where this trend is not clear is over the Main Endeavour Field (figure 4.4o), perhaps due to the location of the vents on the western wall and the strong influence of the rising plumes on the hydrography. The along- and across-valley density gradient was already described in Chapter 3 of this thesis in the context of its dynamical implications for subinertial flows in the valley. This subject will be further discussed when describing the velocity measurements (section 4.5).

4.3.2 Hydrothermal influence

Superimposed on the background density gradient, the lower 300 m of the water column over our study area is characterized by extreme deformation of isopycnal surfaces caused by buoyant plumes of hydrothermal effluent that rise over the active vent fields, equilibrated plumes that spread laterally at levels between 100-300 mab and coherent vortices of plume fluid. These three features, in that order, reflect the different stages that the hydrothermal effluent undergoes once it is discharged into the stratified water column of the deep ocean and are discussed below in detail.

Rising plumes

Rising plumes in the hydrographic sections can be identified by relatively small (a few to a few tens of meters), sharp and intermittent inversions in temperature and density as the sensors slice through them. The intermittency of these observations could be the result of cutting through several individual plumes, but could also attest to the spatial heterogeneity or 'patchiness' observed in individual or merging buoyant plumes (Lupton, 1995; Rona et al., 2002; Bemis et al., 2002; Veirs et al., 2006).

As the hot hydrothermal effluent rises through the stably stratified deep Pacific Ocean, it entrains and mixes with a substantial volume of background water, which is cold and salty, and dilutes the vent fluid by factors of $10^4 - 10^5$ (Lupton, 1995).

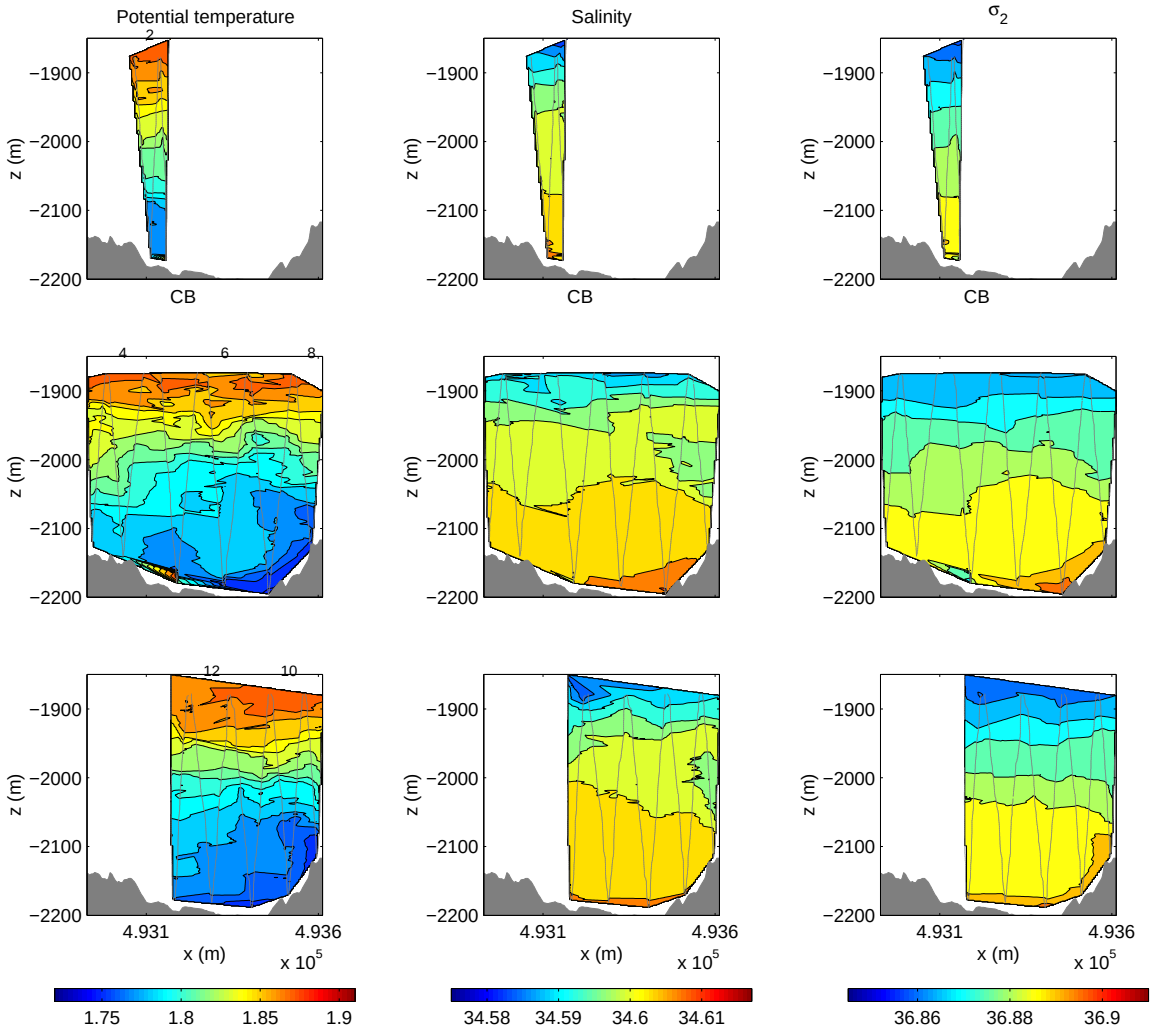

Figure 4.4a: The potential temperature (°C), salinity (psu), and density (kg m^{-3}) for towyo survey 2. The survey started over the center of the axial valley and headed westward (upper panels), crossed the valley eastbound (middle panels), and returned westbound to the point of origin (lower panels). Contour intervals are 0.01°C, 0.0035 psu and 0.005 kg m^{-3}. The cast numbers for each down/upcast pair are specified at the top of the potential temperature sections. The location of Clam Bed is indicated in the upper panels.

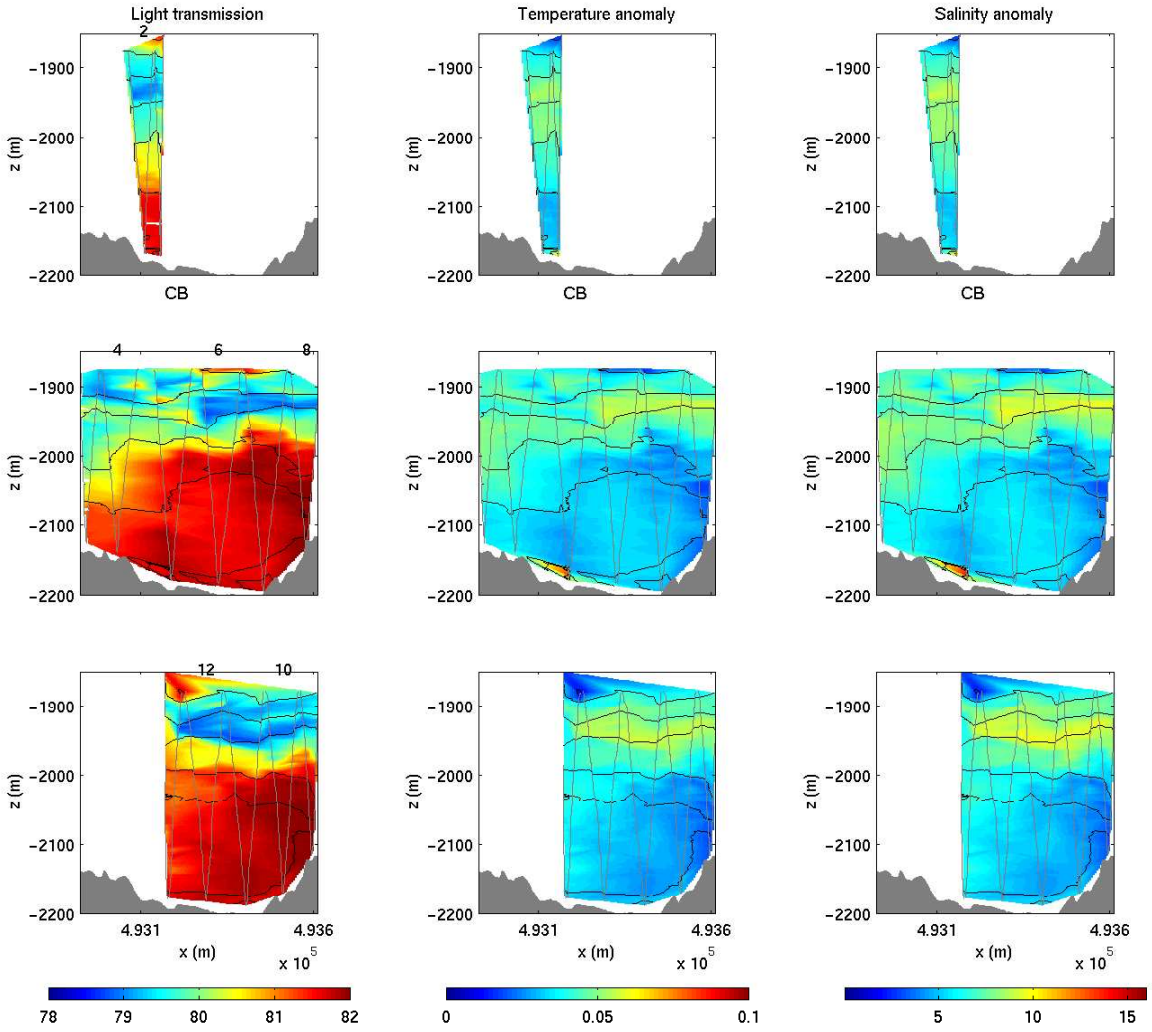

Figure 4.4b: Same as in figure 4.4a, but for the light transmission (%), temperature anomaly (°C), and salinity anomaly (psu).

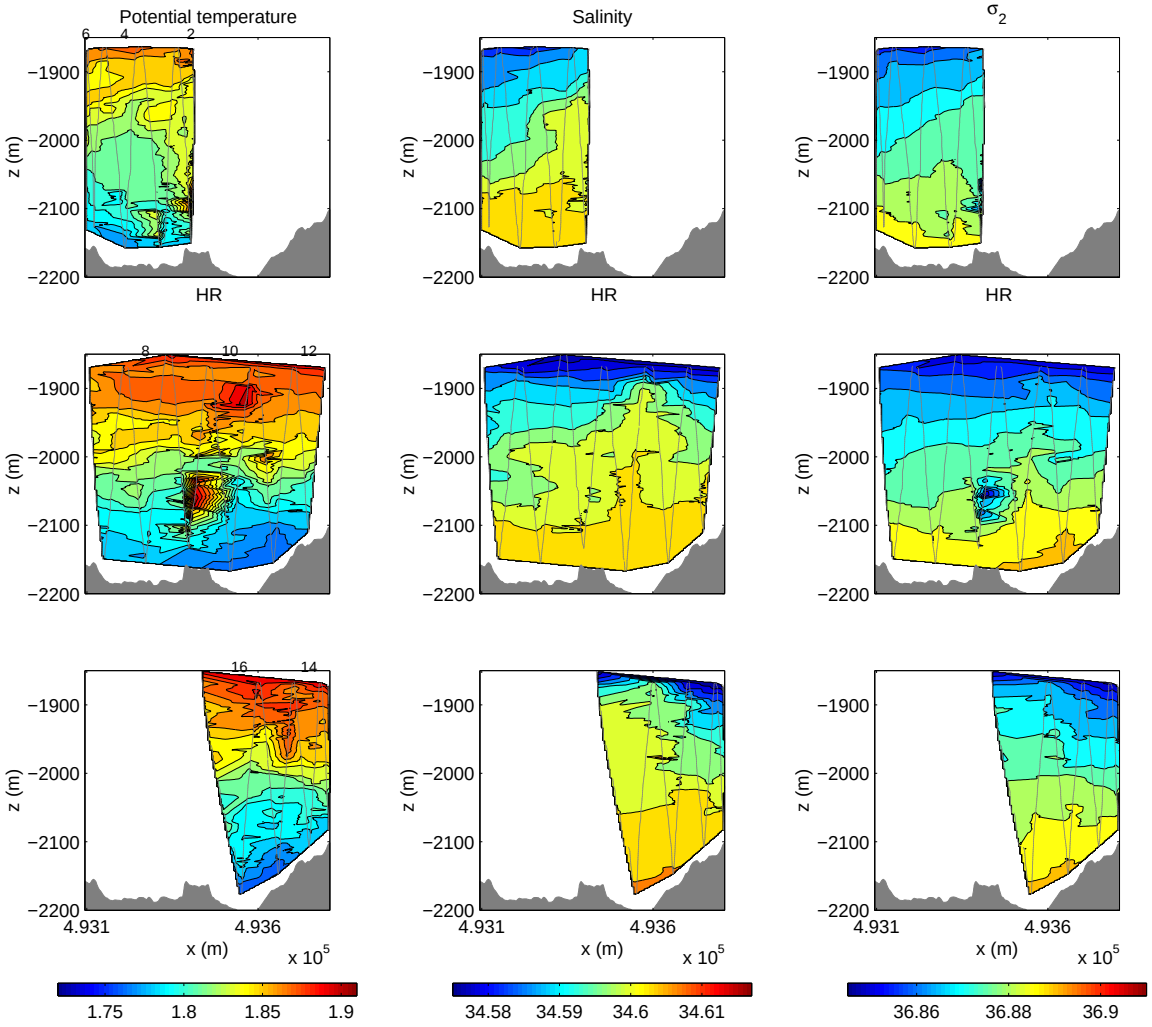

Figure 4.4c: Same as in figure 4.4a, but for towyo survey 3, over High Rise. The location of High Rise is indicated in the upper panels.

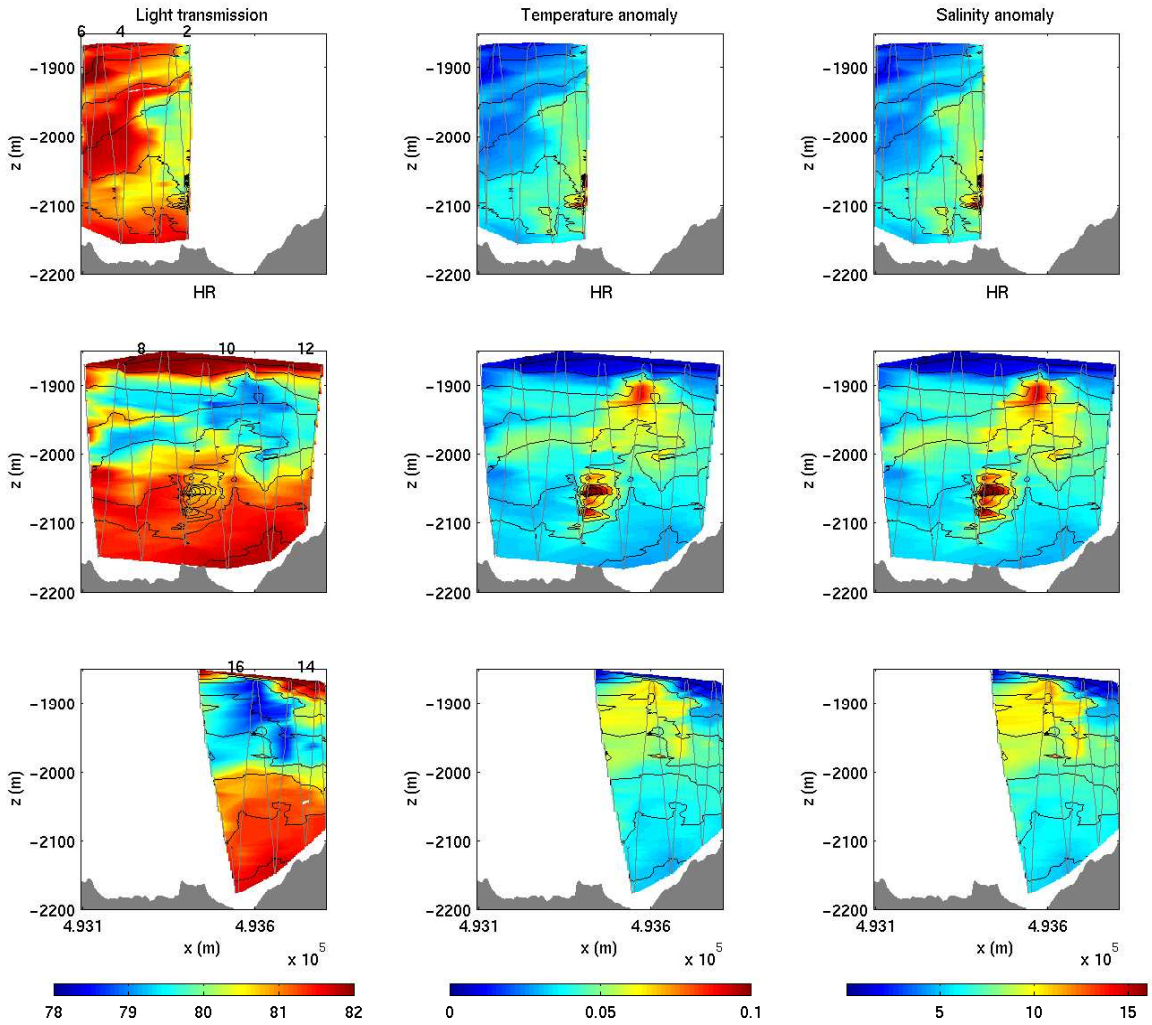

Figure 4.4d: Same as in figure 4.4c, but for the light transmission (%), temperature anomaly (°C), and salinity anomaly (psu).

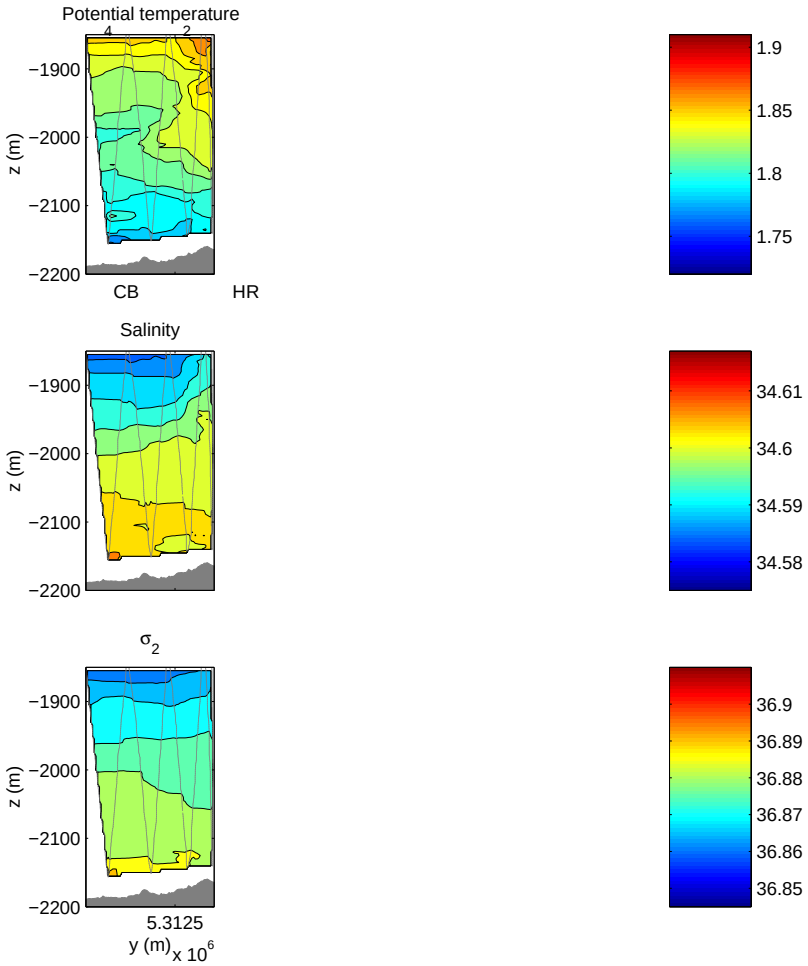

Figure 4.4e: The potential temperature (°C), salinity (psu), and density (kg m^{-3}) for towyo survey 4a southbound from High Rise to Clam Bed.

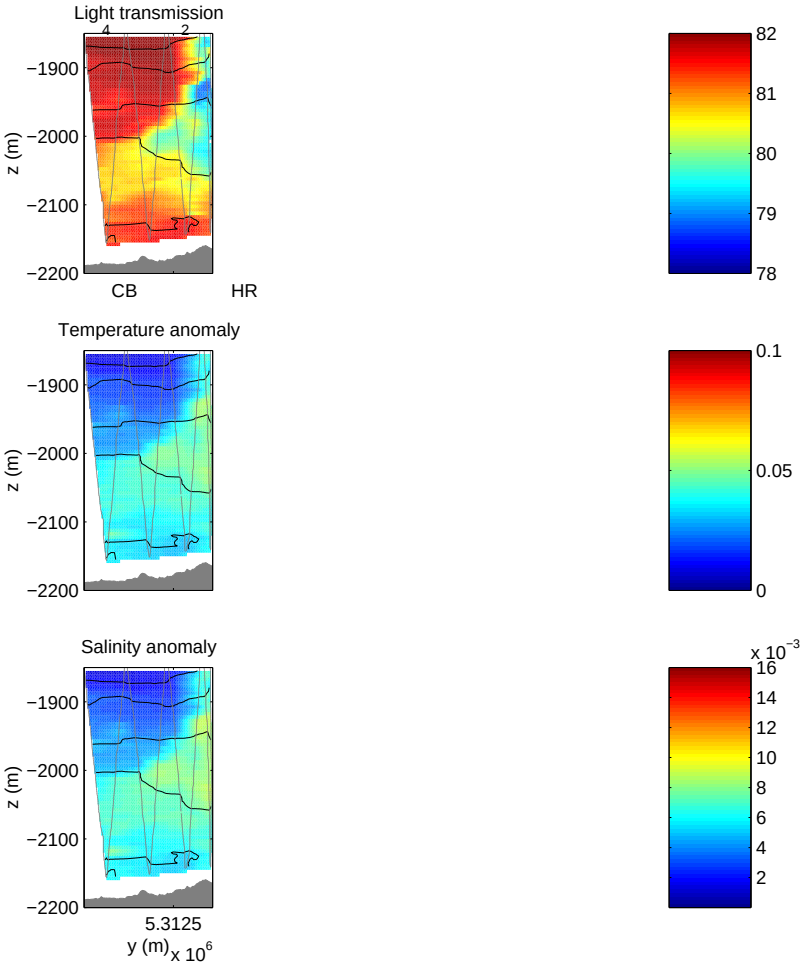

Figure 4.4f: Same as in figure 4.4e, but for the light transmission (%), temperature anomaly (°C), and salinity anomaly (psu).

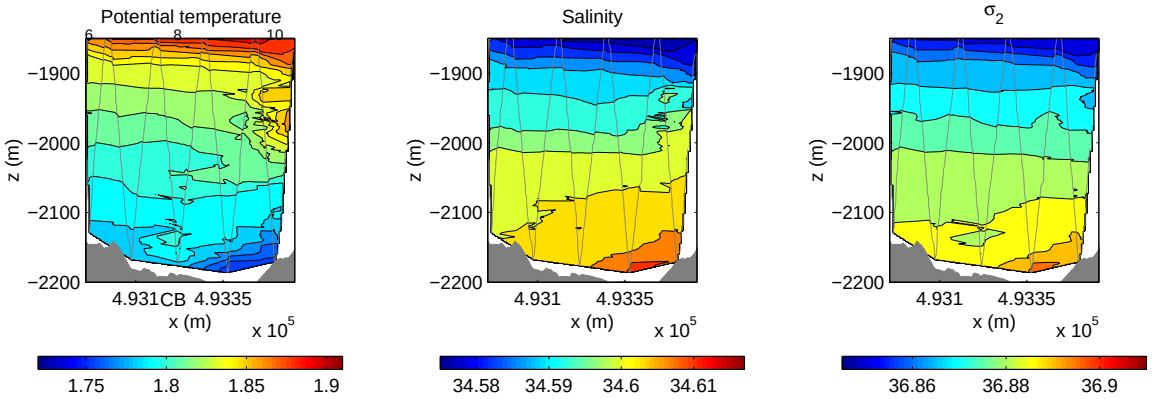

Figure 4.4g: The potential temperature (°C), salinity (psu), and density (kg m^{-3}) for towyo survey 4b across the valley eastbound over Clam Bed.

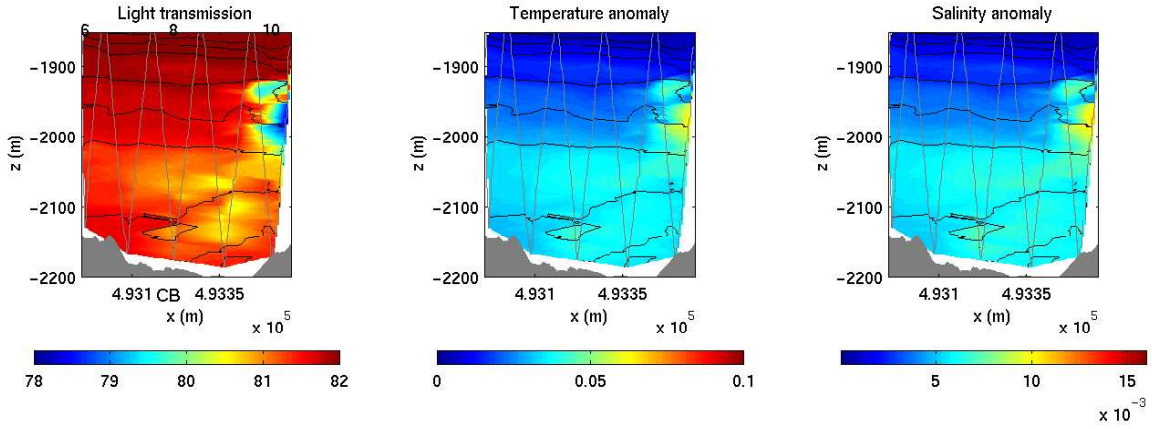

Figure 4.4h: Same as in figure 4.4g, but for the light transmission (%), temperature anomaly (°C), and salinity anomaly (psu).

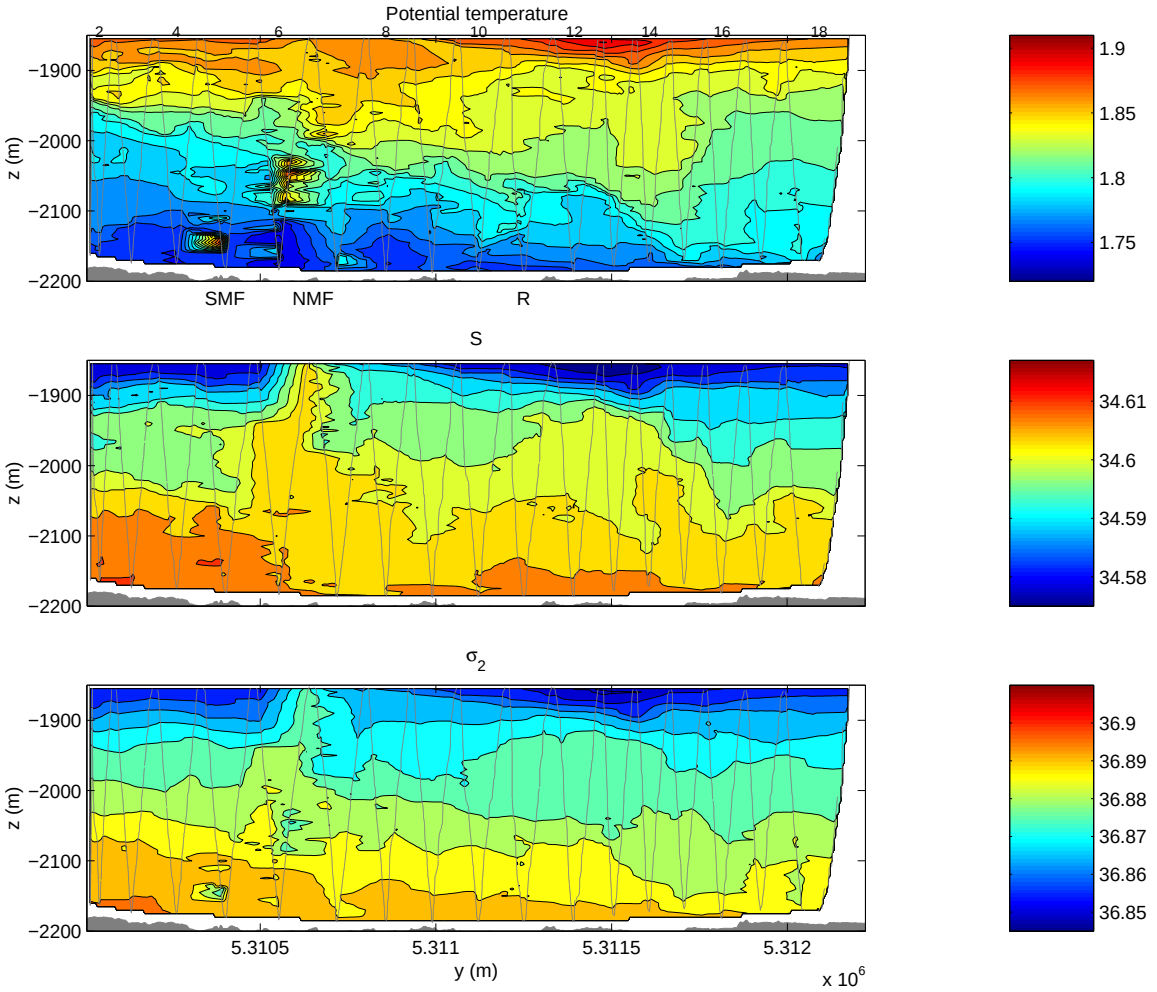

Figure 4.4i: The potential temperature (°C), salinity (psu), and density (kg m^{-3}) for towyo survey 5 northbound from MEF to Clam Bed. Location of fields are indicated in the top panel.

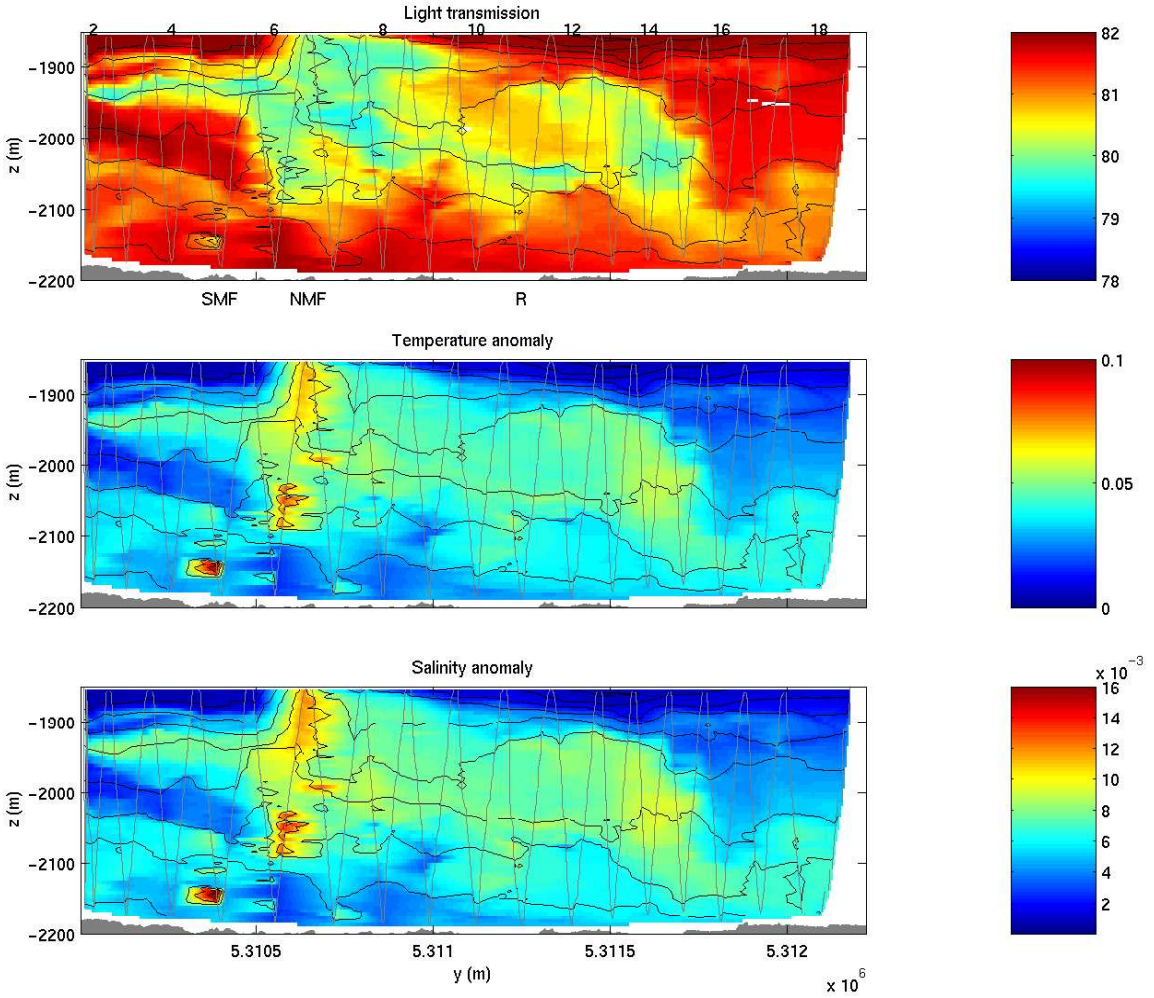

Figure 4.4j: Same as in figure 4.4i, but for the light transmission (%), temperature anomaly (°C), and salinity anomaly (psu).

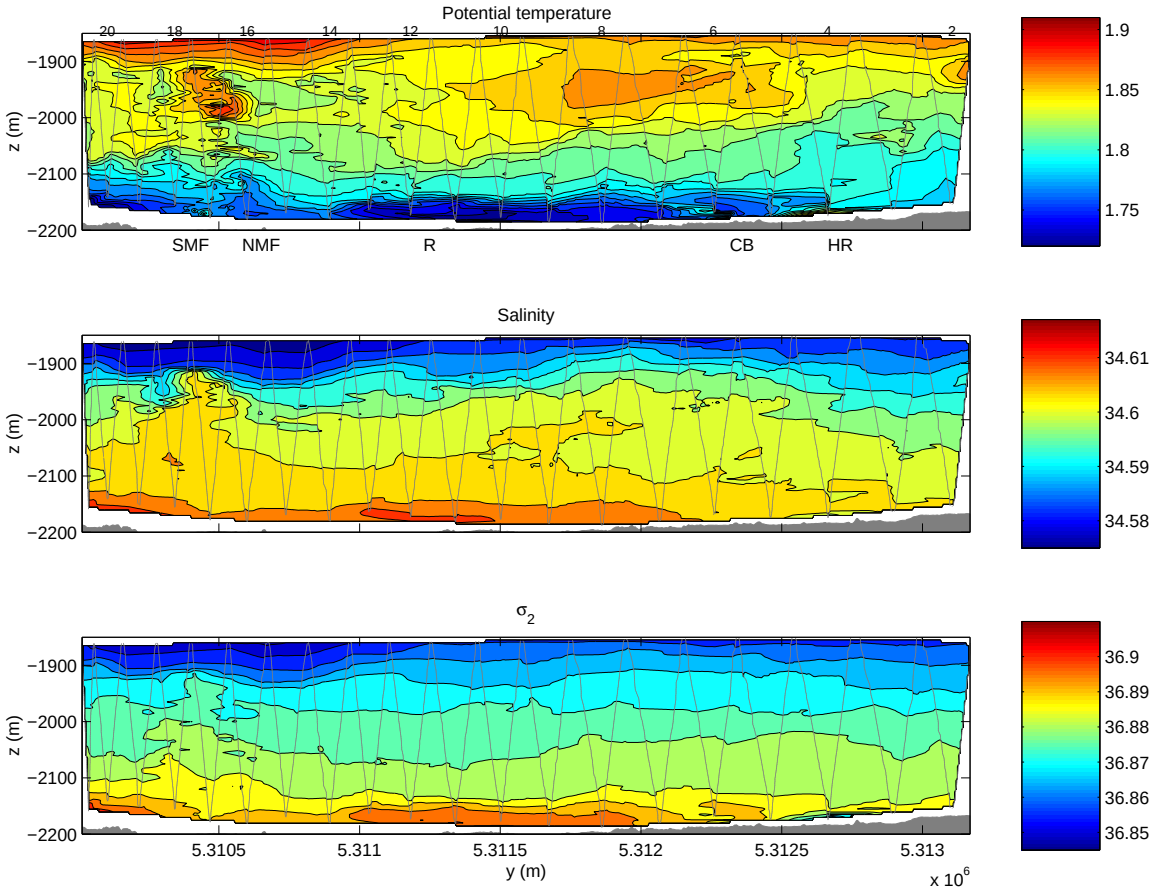

Figure 4.4k: Same as in figure 4.4i, but for towyo survey 7a southbound from High Rise to MEF.

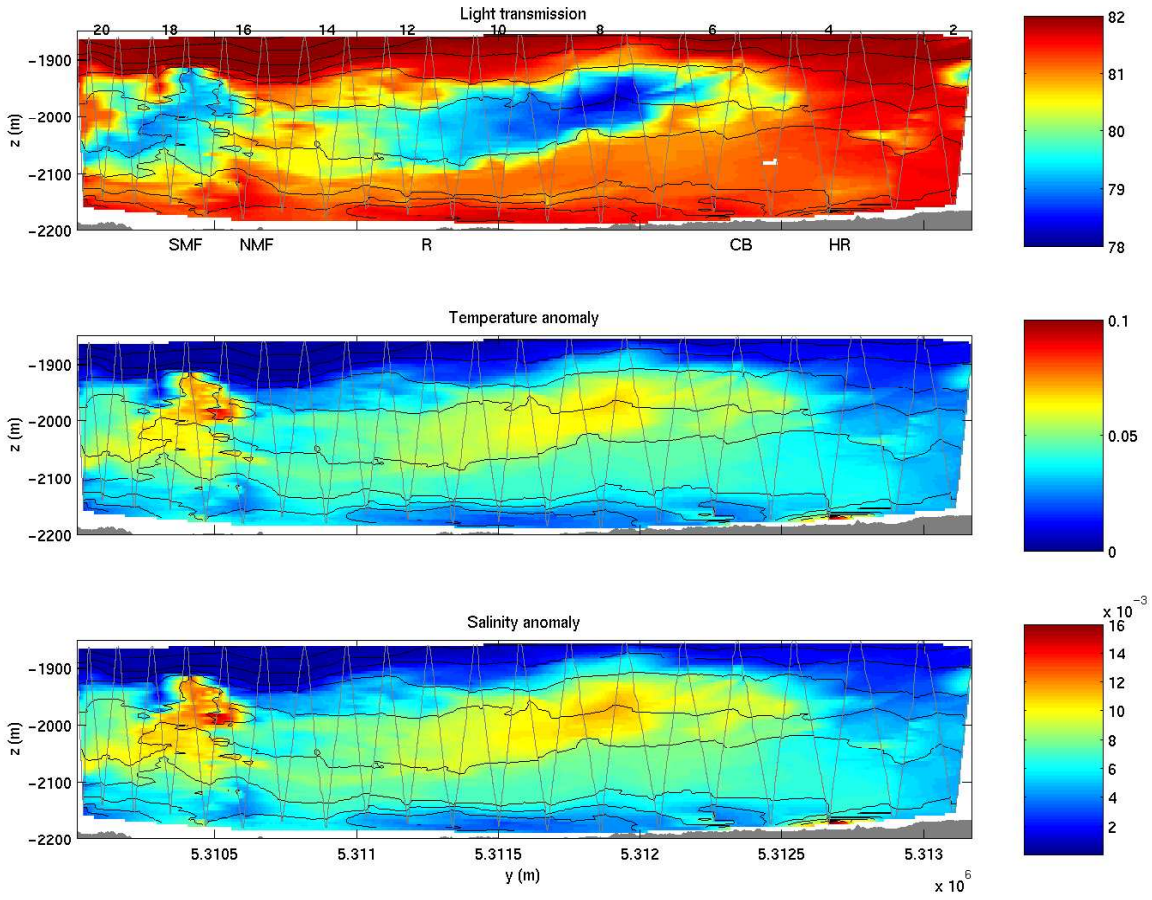

Figure 4.4l: Same as in figure 4.4k, but for the light transmission (%), temperature anomaly (°C), and salinity anomaly (psu).

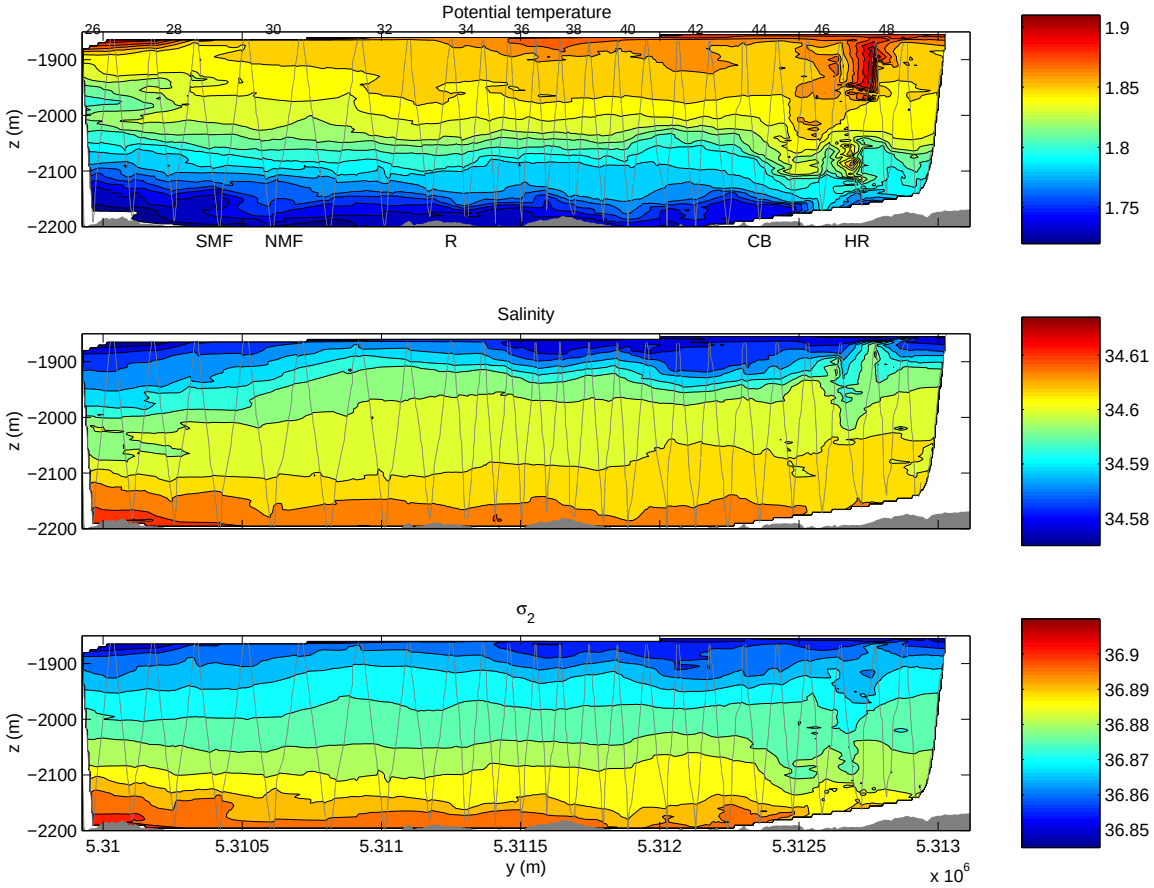

Figure 4.4m: Same as in figure 4.4i, but for towyo survey 7b northbound along a line on the eastern valley wall. The y-locations of the vent fields are indicated in the top panel.

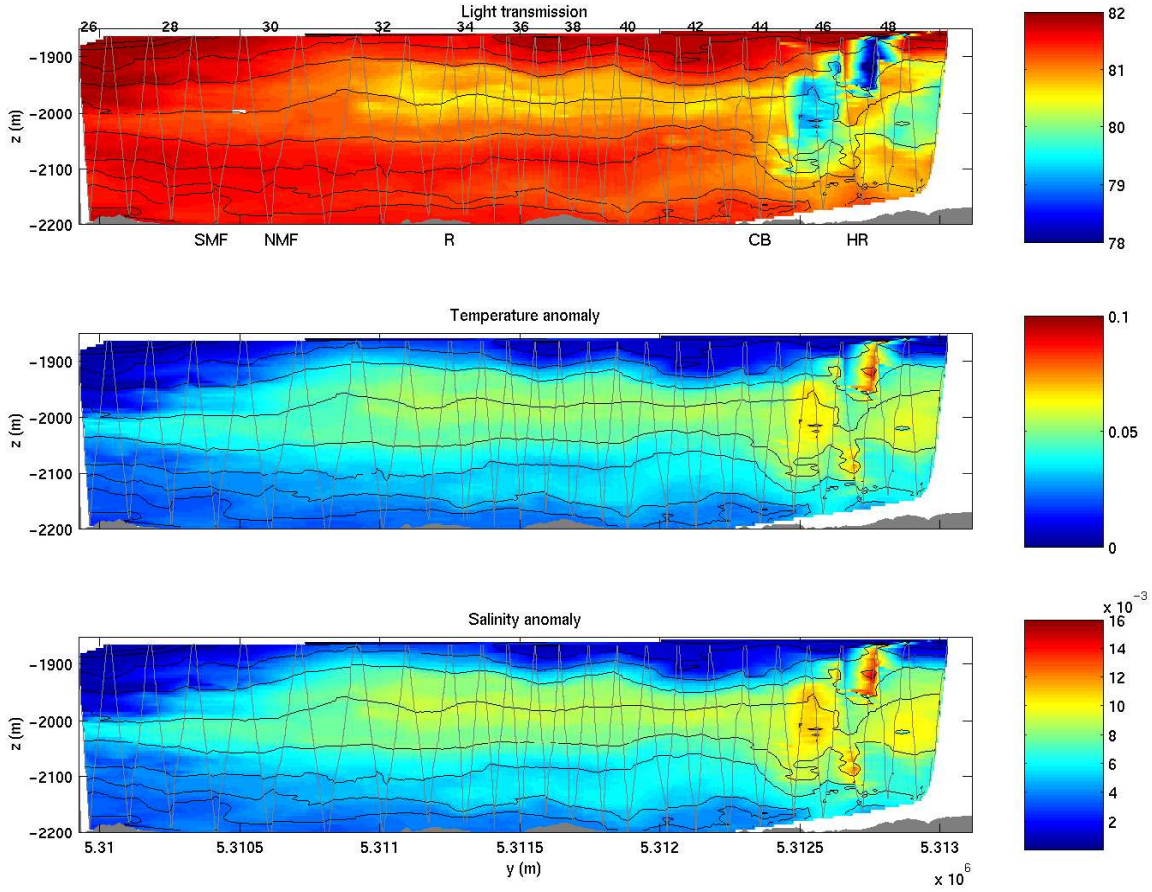

Figure 4.4n: Same as in figure 4.4m, but for the light transmission (%), temperature anomaly (°C), and salinity anomaly (psu).

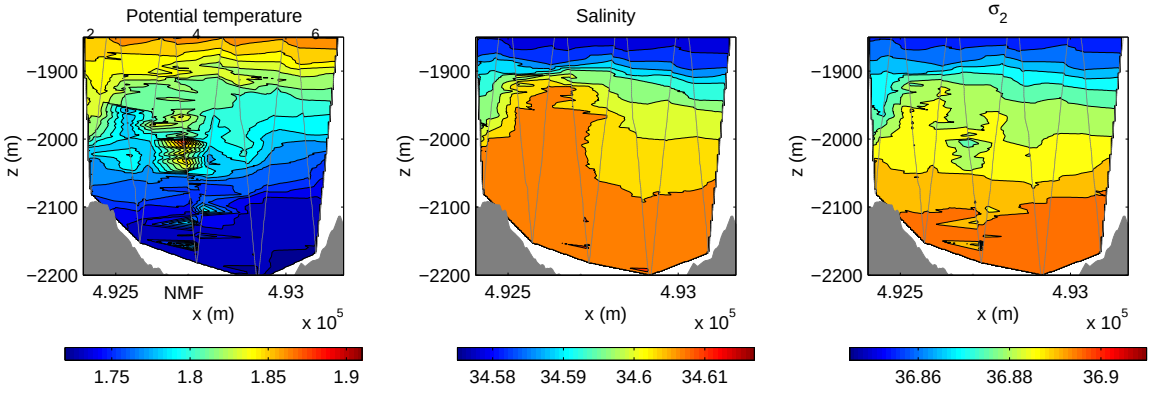

Figure 4.4o: The potential temperature (°C), salinity (psu), and density (kg m^{-3}) or a towyo survey conducted across-valley eastbound over MEF in 2003.

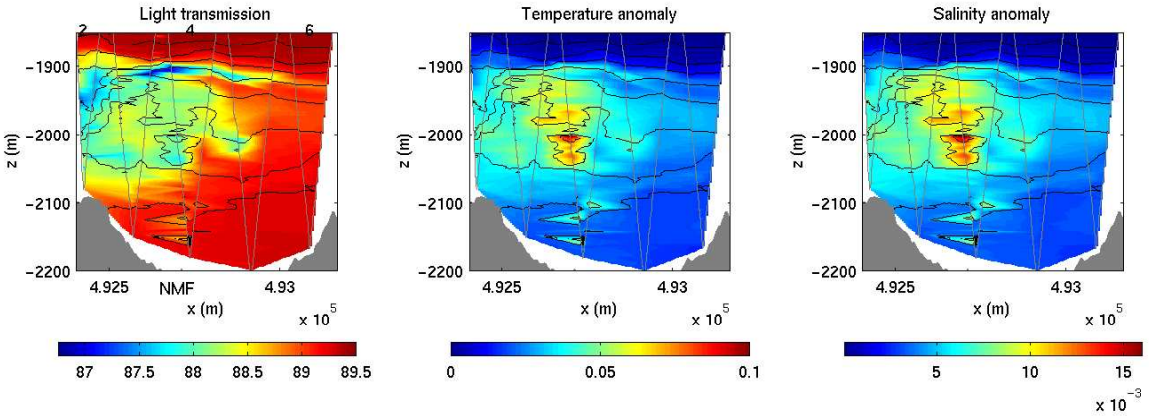

Figure 4.4p: Same as in figure 4.4o, but for the light transmission (%), temperature anomaly (°C), and salinity anomaly (psu).

This entrainment is clearly observed in the salinity and density sections over Main Endeavour field (figures 4.4i, k, o) and, to a lesser extent, over High Rise (figures 4.4c, e). The entrainment of denser water reduces the buoyancy of the plume, which eventually reaches a level where it has the same density as the background water. Due to its momentum, the rising plume overshoots the level of neutral buoyancy until, decelerated by its negative buoyancy, it reaches its maximum rise height. The very pronounced uplifting (~ 100 m) of isopycnals seen in figure 4.4i at the top of the plume over North Main Endeavour Field (NMF) may be evidence of such overshooting.

Scaling arguments and laboratory experiments (Turner, 1973) have established that with no background flow the maximum rise height of a buoyant plume is a function of the source buoyancy flux $B_o = (g\alpha H_s)/(\rho_o c_p)$ (where g is the acceleration of gravity; α is the thermal expansion coefficient; ρ_o is the reference density; c_p is the specific heat capacity; H_s is the source heat flux; and where the contribution of salinity to B_o, much smaller than that of temperature, has been neglected) and the ambient stratification through the buoyancy frequency, N:

$$z^* = 5B_o^{1/4}\ N^{-3/4}. \tag{4.1}$$

In the presence of a background flow of strength U, the rise height of the plume is reduced and scales as $z^* \sim (B_o/UN^2)^{1/3}$ (Turner, 1973).

Maximum vertical extensions of buoyant plumes as seen in the sections of hydrographic and tracer fields lie in a depth range between 1950 m to less than 1850 m. The MEF plume alluded to above and seen in figure 4.4i rises to a level 350 mab (1850 m depth). This large rise height may be the result of a strong source buoyancy and weak background stratification (these factors will be further analyzed in section 4.4), combined with the lack of ambient currents, as this plume was sampled at slack tide (see beginning of this towyo survey in figure 4.2). On the other hand, the plume sampled over MEF during towyo survey 7 (figure 4.4k) does not appear to rise as high. One reason could be the fact that it was sampled during southward tidal flow (see end of towyo survey 7a in figure 4.2). However, the discrepancy could be also explained by a weaker buoyancy source, temporal variability associated with internal gravity waves (Rudnicki and German, 2002), or not having sampled the rising plume straight through its core.

Figures 4.5 and 4.6 show hydrocasts that sliced through rising plumes over Main Endeavour and High Rise fields, respectively. The profiles give a sense of the dimension of the overturns (density inversions) in the plume, which can be as large as few tens of meters. In the θ-S relation the mixing manifests itself as a cluster of points along a line connecting two end-points (source or plume water and background water). In figure 4.5 there are two apparent mixing lines observed in rising plume water, one nearly vertical and one nearly horizontal, indicating mixing in temperature and salinity, respectively. During the positively buoyant stage, the plume mixes mainly in temperature (e.g., cast 506u between -2025 m and -2090 m). Past the level of neutral buoyancy it mixes in salinity (e.g., cast 507d between -1850 m to -1950 m, where unstable density gradients are largely caused by salinity inversions). The nearly uniform high salinity from -1850 m to -2000 m seems to indicate that cast 506u is in the core of the plume, while the consecutive cast (507d), which shows a strong mixing in salinity

at those depths (forming the horizontal mixing line), would be on the perimeter of the plume. This interpretation is supported by the fact that, as seen in laboratory experiments of buoyant plumes (Wang and Law, 2002), mixing occurs on the edges, and that steady buoyant plume theory predicts a diameter of $\sim$ 100 m at this height (see section 4.4), larger than the inter-cast distance. So it seems plausible that we are sampling different portions of the same plume.

Although a horizontal θ-S relationship is found above equilibrated plumes transitioning to background water, a single mixing line is observed in the limited number of casts that sliced through rising plumes over High Rise (figure 4.6). In contrast to the observations over MEF, the tilt of the mixing line denotes a lower-salinity source (see section 4.4 for justification). Using linear fits to the observed mixing lines, the inferred source salinity is 22 psu for High Rise and 32 psu in MEF, assuming a source temperature of 350 °C. Interestingly, the source salinities are thought to generally decrease from north to south (M. Lilley, pers. comm.), although there is a range in values within any given vent field. For example, Kelley et al. (2002) cite ranges in chlorinity of 40-505 mmol/kg for MEF and 420-587 mmol/kg for High Rise. Therefore, it is possible we might have been sampling particularly low salinity effluent over High Rise, or particularly salty effluent over MEF. Alternatively, source chemistry is known to change following magmatic events (Lilley et al., 2003) so values of source salinities could have changed in either vent field since the last published measurements. Another difference between the rising plumes from the two vent fields is that the positive buoyancy anomalies are stronger in High Rise. This could imply that the buoyancy fluxes are larger over High Rise than MEF, although our sample size is rather small to confirm this.

Laterally spreading equilibrated plumes

At the level of neutral buoyancy of the hydrothermal plumes, the diluted effluent spreads laterally due to gravitational adjustment and may also be advected by back-

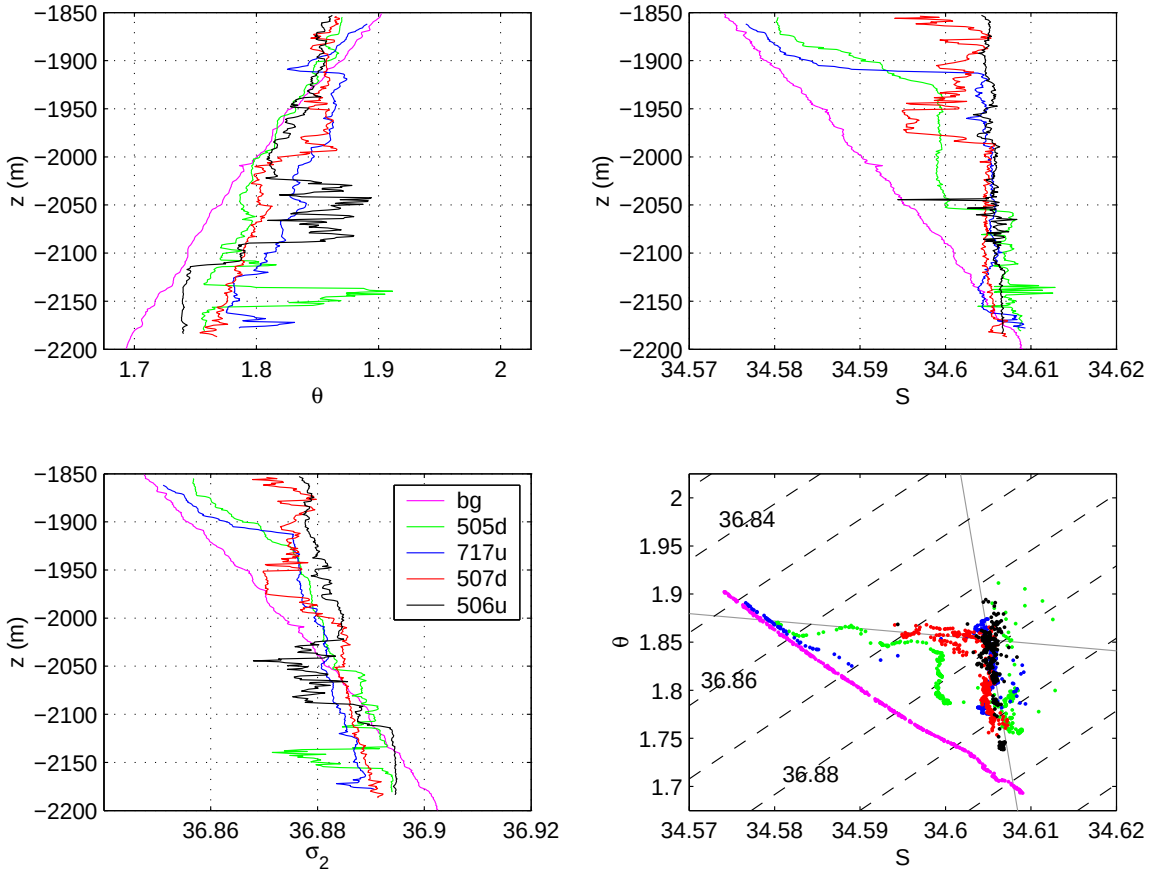

Figure 4.5: Profiles of potential temperature (upper left), salinity (upper right) and density (lower left), and θ-S relation (lower right) for casts that slice through rising plumes over MEF. A linear fit (gray line) to the points corresponding to density inversions is drawn on the θ-S plot, indicating a mixing line between vent fluid and background water. Up- or downcast numbers shown in the legend are preceded by the corresponding survey number (hundreds). An off-axis background cast is plotted in magenta.

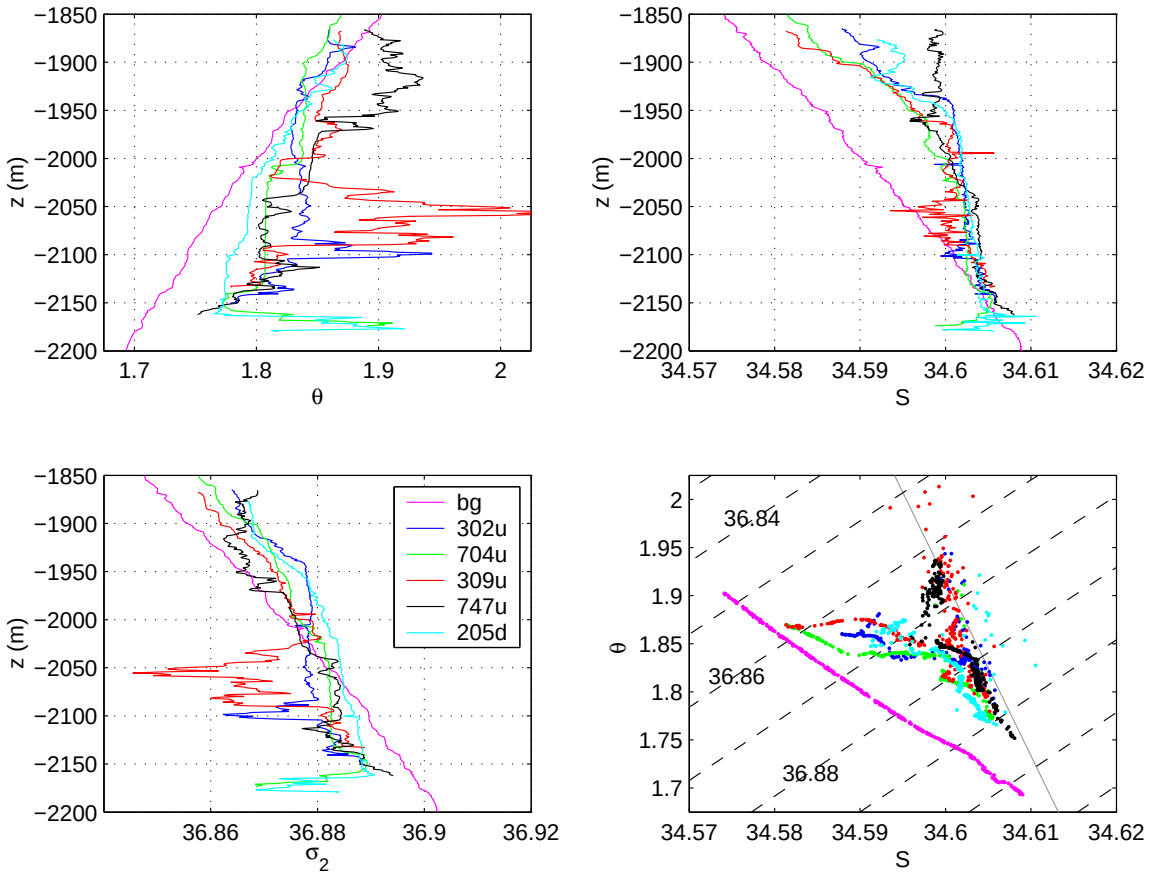

Figure 4.6: Same as figure 4.5, but for casts taken over High Rise.

ground currents. The hydrothermal effluent in the deep Pacific Ocean is easily identified by its positive temperature and salinity anomalies (Speer and Rona, 1989), which can be used, together with light transmission or optical backscatter, as tracers (figure 4.4). Lateral spreading often manifests itself as thin lenses in the transects (for example, south of MEF in towyo survey 5 or west of High Rise in towyo survey 3). Such a feature is shown in detail in figure 4.7. Although there exist both temperature and salinity inversions, they compensate each other, a signature of an equilibrated plume. These thermohaline intrusions lead to large along-isopycnal excursions in θ-S space, that are correlated with decreased levels of light transmission. The multiple lenses in the vertical could be a consequence of the plume (or plume mixture) variability in source buoyancy flux and or background currents present during the rising stage of the plume, which as discussed previously, affect the rise height.

Repeated across-valley transects over Clam Bed reveal variability in the spreading effluent over tidal time scales (figures 4.4b, e). Hydrothermal fluid seen in figure 4.4b seems to originate from High Rise, 300 m to the north, since even though the tidal flow is northward during the transect, a tracer field advected by tides will lag the tidal velocity by one quarter cycle. These observations illustrate how the neutrally buoyant plume is affected by tidal advection within distances from a vent field that are less than a tidal excursion ($\sim$500 m).

Mesoscale eddies

After an inertial period, the neutrally buoyant spreading plume feels the earth's rotation and acquires an anticyclonic circulation. Laboratory experiments have shown that this plume vortex becomes unstable when its radius is approximately one Rossby radius and breaks into vortex pairs that propagate away from the source region (Helfrich and Battisti, 1991). These features were found to have an aspect ratio $H/L \sim f/N$. The bolus seen in the center of towyo survey 7a forms a coherent structure that retains diluted hydrothermal fluid and has an aspect ratio

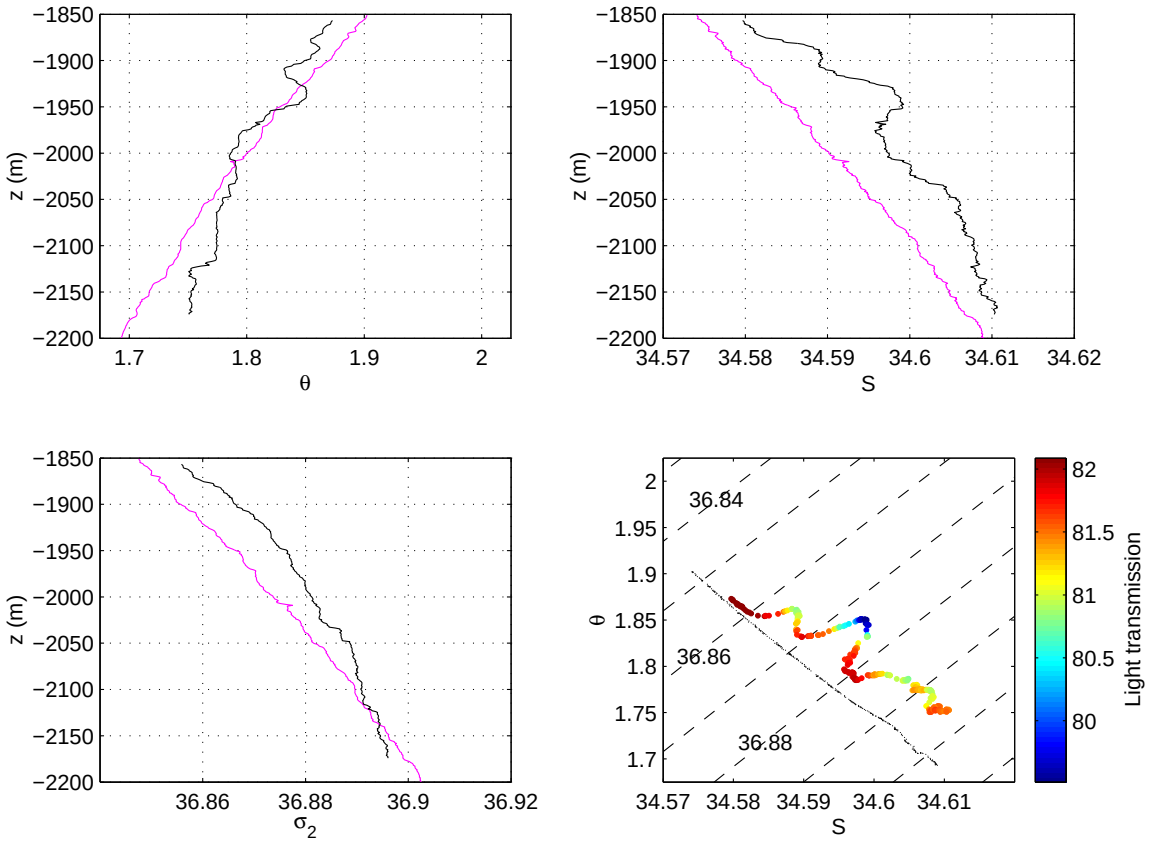

Figure 4.7: Potential temperature (upper left), salinity (upper right) and density (lower left) profiles, and θ-S relation (lower right) for 503d, south of MEF, illustrating thermohaline intrusions. An off-axis background cast is plotted in magenta on the profiles and in black on the θ-S relation.

$H/L \sim 100$ m/1000 m ~ 0.1, which is comparable to $f/N \sim 10^{-4}$ s^{-1}/10^{-3} s^{-1} (figure 4.4l), suggesting it could be a plume vortex. Similar features suggestive of plume vortices are also evident in the temperature anomaly and light attenuation fields observed by Thomson et al. (1992) and Baker and Massoth (1987) at Endeavour.

An intriguing question is from which vent field this bolus originated. An illuminating way to address this question is to calculate the "spice" (Veronis, 1972)

$$\tau = \rho_o(\beta S + \alpha\theta), \tag{4.2}$$

where α is the thermal expansion coefficient and β is the coefficient of haline contraction, on the isopycnal surface that slices through the core of the bolus. Spice variations do not affect the density but instead provide information on the origin of water masses with unique θ-S relations. Warm water of hydrothermal origin has in general elevated values of spice, but are there sufficient spice variations from individual vent fields so that the spice can be used to distinguish the different vents' effluent? Based on the mixing line calculation described above, the water originating from MEF is saltier than that in the High Rise plumes, suggesting that the water from MEF should be "spicier" than that from High Rise. Plotted in figure 4.8 is τ on the isopycnal surface that intersects the center of the bolus ($\sigma_2 = 36.877$ kg m^{-3}). The figure illustrates that the spice is consistently larger over the MEF than over High Rise. The spice in the core of the bolus (line 7a, $y = 5311800$ m) is less than τ near the MEF and similar to τ near High Rise. Therefore, two scenarios emerge as candidates for explaining the origin of the water in the bolus. If the water in the core of the bolus has not undergone any mixing, then the water could have originated at High Rise. The second scenario is that the water mixed while coalescing on the equilibrium isopycnal to form the bolus and hence the spice has been modified. If this were the case, then the water would most likely have originated near MEF, since mixing of high-τ MEF waters with low-τ background waters would result in the water

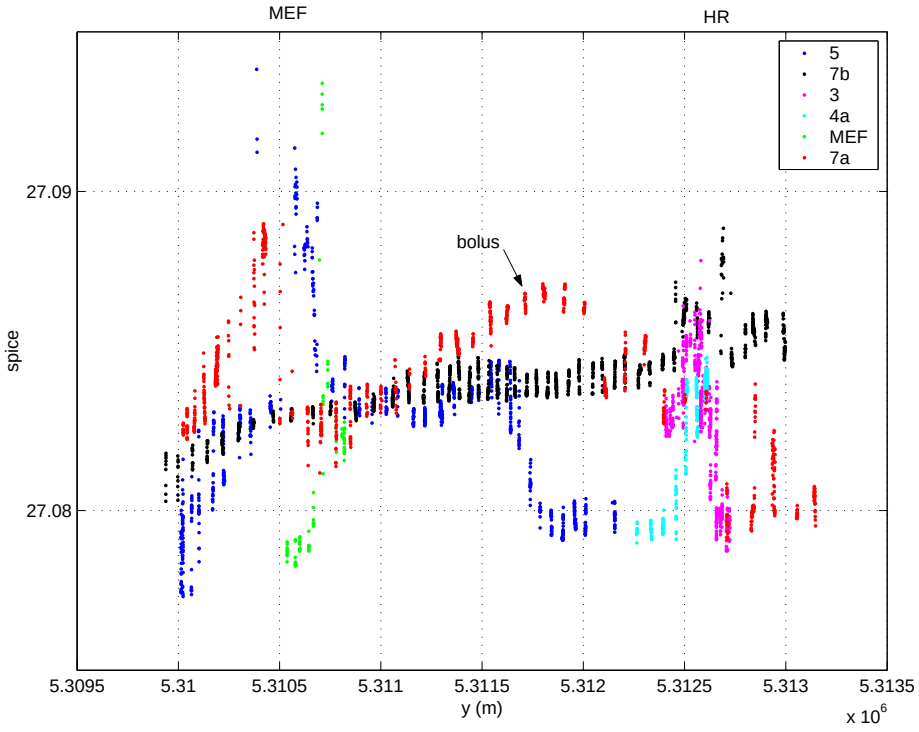

Figure 4.8: Spice on $\sigma_2 = 36.877$ kg m^{-3} as a function of y-distance for all towyo surveys except the cross-valley surveys over Clam Bed. The y-locations of the vent fields of MEF and High Rise are indicated at the top of the plot.

with intermediate spice values similar to what is observed in the bolus. Reduction of spice can occur due to lateral isopycnal mixing, turbulence, and double diffusion (Schmitt, 1999). The evidence of thermohaline intrusions (figure 4.7) suggests that isopycnal mixing of spice is active near the vents. In these intrusions, the presence of warm, salty water over relatively fresh, cold water provides the right conditions for double diffusion. However, the delicate process of double diffusion could be overwhelmed by the high levels of turbulence surrounding the rising plumes. Regardless of whether spice is mixed laterally, through turbulence, or via double diffusion, it is likely that the spice in the bolus has been mixed and thus is a signature of MEF effluent.

4.4 Comparison of observations to a model of a steady buoyant plume

The standard model for buoyant plumes, first derived by Morton et al. (1956) and adapted by Speer and Rona (1989) to include the effects of salinity and temperature, solves for the vertical structure of the vertical velocity (W) and tracers (θ, S) averaged over the cross-sectional area A of an axially symmetric, steady plume. The model equations are derived by applying the principles of conservation of mass, salinity, heat, and momentum and assuming that the entrainment velocity is proportional to W:

$$\begin{aligned} \frac{d}{dz}AW &= EA^{1/2}W \\ \frac{d}{dz}SAW &= E\overline{S}A^{1/2}W \\ \frac{d}{dz}\theta AW &= E\overline{\theta}A^{1/2}W \\ \frac{d}{dz}AW^2 &= -\frac{g}{\rho_o}(\rho-\overline{\rho})A, \end{aligned} \tag{4.3}$$

where g is the acceleration due to gravity, $\overline{\theta}(z)$ and $\overline{S}(z)$ are the profiles of the temperature and salinity of the background water surrounding the plume, and $E = 0.255$ is the entrainment coefficient.

The plume model was solved numerically for a vertical velocity, temperature, heat flux, and salinity at the source of 1 m s^{-1}, 350 °C, 10 MW, and 34 psu respectively (all typical values for a black smoker at MEF, Veirs (2003); Bemis et al. (1993)), and for an idealized background temperature/salinity profile derived from a polynomial fit to profile data taken off-axis, ($\overline{\theta}_{or}$, $\overline{S}_{or}$):

$$\begin{aligned} \overline{\theta}_{or} &= 1.68 + 5.98\times10^{-4}z \\ \overline{S}_{or} &= 34.610 - 1.02\times10^{-4}z. \end{aligned}$$

A linearized equation of state was used following (Speer and Rona, 1989).

The general properties of the solution to the steady plume model are illustrated in figure 4.9. Direct comparison of model to observed profiles is not appropriate because

the casts are likely slicing through different parts of a plume or several plumes and plumes in the field are very patchy (Lupton, 1995; Rona et al., 2002; Bemis et al., 2002). In contrast, the model solution is a steady, one-dimensional plume whose properties represent an average over the cross-sectional area. A proper direct comparison would entail sampling the rising plume repeatedly at several levels ideally closer to the vent (e.g., Little et al. (1987); Bemis et al. (1993)), to obtain statistically significant spatially and temporally averaged plume properties. Nevertheless, a qualitative examination of the model is helpful in interpreting our observations and understanding the processes that set the properties of rising plumes, such as rise height and θ-S relation. To this end, the sensitivity of the model to the relevant parameters involved is also examined below.

As seen in figure 4.9(a), the radius of the plume expands with height as fluid is entrained from the sides, reaching values of ~ 50 m at the level of maximum rise height of the plume. At this level, located where $W = 0$ (figure 4.9(b)), the model calculation terminates. The difference between the density of the plume and the background fluid $\Delta\rho = \rho - \overline{\rho}$ is less than zero over much of the plume height (figure 4.9(e)), reflecting the plume's positive buoyancy, but crosses zero at a level of neutral buoyancy beneath the total rise height of the plume. Due to its upward momentum, the plume overshoots this equilibrium point, and continues to rise until, decelerated by its negative buoyancy, it reaches its maximum height. Evidence of such overshooting is apparent in some of the hydrographic sections, most prominently in towyo survey 5 over north MEF (figure 4.4i). Past the first tens of meters, the salinity in the model plume is greater than that of the ambient environment due to the entrainment of the saltier, near-bottom water (figure 4.9(d)). This positive salinity anomaly is consistent with the rising plumes observed over the MEF (figure 4.5). In θ-S space, the plume solution takes on a "hockey-stick" shape with a nearly vertical mixing line, for depths below the level of neutral buoyancy where the warm water is diluted, and a more horizontal mixing line at the top of the plume, where the positive salinity anomaly is weakened

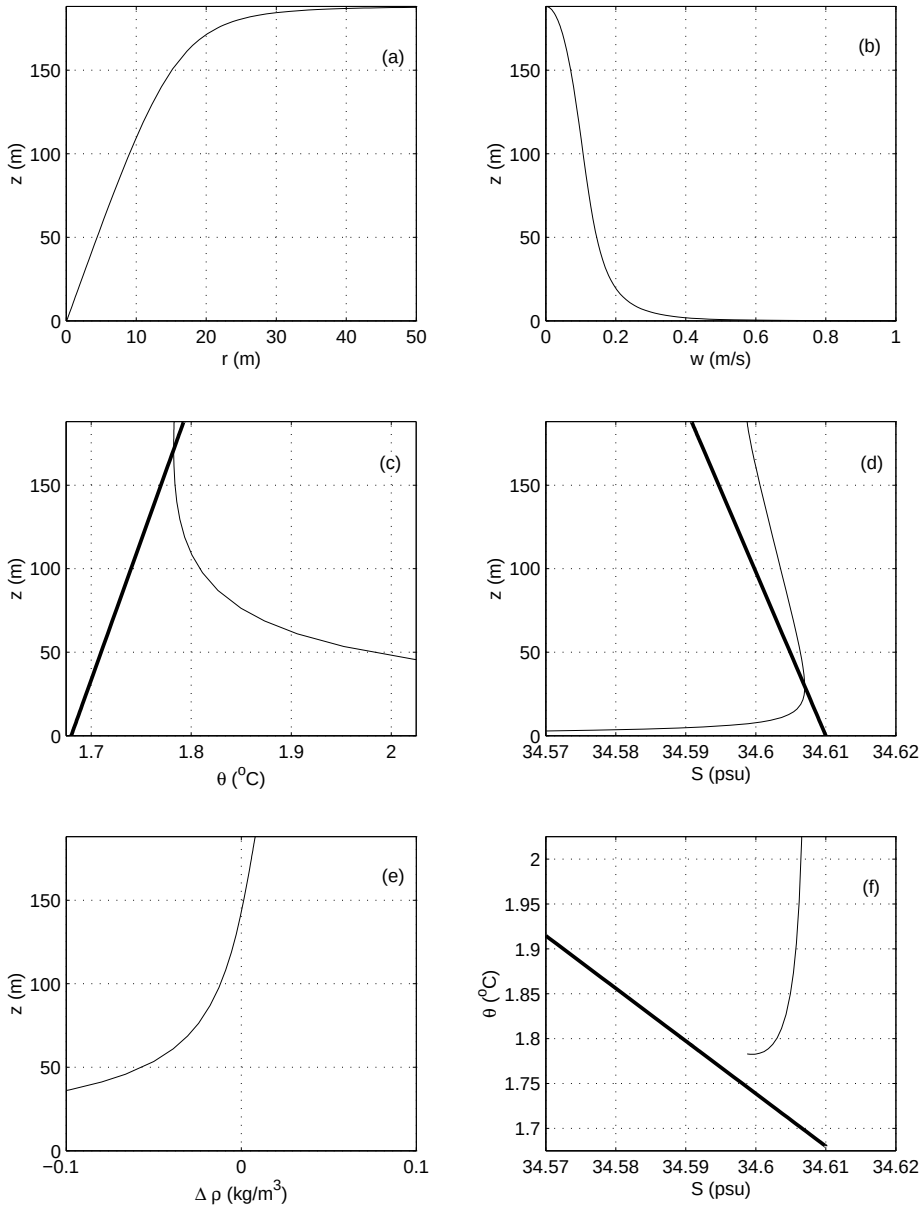

Figure 4.9: The radius (a), vertical velocity (b), temperature (c), salinity (d), density difference between the plume and background (e), and θ-S relation (f) for the steady-plume model solution for case 1. The thick black lines denote background quantities.

Table 4.1: Parameters for steady-plume model calculations.

	H_s (MW)	S_s (psu)	background
case 1	10	34	$\overline{\theta}_{or}$, $\overline{S}_{or}$
case 2	10	20	$\overline{\theta}_{or}$, $\overline{S}_{or}$
case 3	10	34	$\overline{\theta}_{v1}$, $\overline{S}_{v1}$
case 4	10	34	$\overline{\theta}_{v2}$, $\overline{S}_{v2}$
case 5	50	34	$\overline{\theta}_{v1}$, $\overline{S}_{v1}$

4.9(f)). This structure arises because the entrainment fluxes of heat/salinity are proportional to the differences in temperature/salinity between plume and background. Below the equilibration depth, entrainment reduces mostly the temperature of the plume since the plume salinity is relatively close to background values; at the top, plume temperature is close to background values, but salinity is significantly different from background (4.9(c) and (d)), so it mixes predominantly in salinity. The bottom of the hockey-stick marks the point where the model calculation terminates; above this level, the θ-S curve would rejoin background water lying above the equilibrated plume. The two-step mixing process described above is similar to what is observed over MEF (figure 4.5). Notice however, that the nearly horizontal mixing line at the top of cast 507d was absent in the adjacent cast 506u, suggesting that significant lateral variation was present in the rising plume, thus making a direct comparison of the observations with the one-dimensional steady plume model solutions difficult.

To test the sensitivity of the solution to the properties of the ambient environment and source parameters, the model was run again for the combinations of source heat flux (H_s), source salinity (S_s), and background profile listed on table 4.1, where ($\overline{\theta}_{v1}$, $\overline{S}_{v1}$) is an idealized background derived from fitting a polynomial to the data from

cast 510, taken in the valley close to MEF but away from actively rising plumes,

$$\begin{aligned} \overline{\theta}_{v1} &= 1.75 + 5.3 \times 10^{-4} z - 6.0 \times 10^{-7} z^2 \\ \overline{S}_{v1} &= 34.606 + 1.6 \times 10^{-5} z - 2.1 \times 10^{-7} z^2, \end{aligned}$$

and ($\overline{\theta}_{v2}$,$\overline{S}_{v2}$) is a second idealized background in the valley, derived from fitting a polynomial to the data from a full-depth cast taken in the High Rise area before towyo survey 7a,

$$\begin{aligned} \overline{\theta}_{v2} &= 1.78 + 2.8 \times 10^{-4} z - 1.6 \times 10^{-7} z^2 \\ \overline{S}_{v2} &= 34.605 - 3.8 \times 10^{-5} z - 9.0 \times 10^{-8} z^2. \end{aligned}$$

The results of the sensitivity study are highlighted in figure 4.10. Changing the source salinity to 20 psu (the lowest observed in south MEF, Veirs (2003)) does little to affect the rise height of the plume, but dramatically alters the orientation of the mixing line in θ-S space (figure 4.10a, b). Comparing the observed θ-S structure of the MEF and High Rise plumes (figures 4.5 and 4.6) reveals a similar variation in mixing line orientation, supporting the inference that the plumes sampled over High Rise originate from less saline sources than those over MEF. Plumes rising through an ambient environment characteristic of valley versus off-axis waters reach greater heights (figure 4.10c), since the stratification is weaker in the valley. A less stratified valley profile is more representative of the actual background water that the sampled plumes entrain. There is also a difference in the background water that is being entrained by buoyant plumes at the southern and northern ends of the valley (see backgrounds plotted in 4.10d). The water entrained at MEF is saltier (and denser) because the bottom is deeper than at High Rise and because there is a southward horizontal density gradient along the valley as well. While the background used in case 4 (more representative of High Rise background conditions) results in a plume of less salinity than in case 3 (MEF background), in spite of having the same source salinity, it does not change the plume's inclination in θ-S space. This suggests that

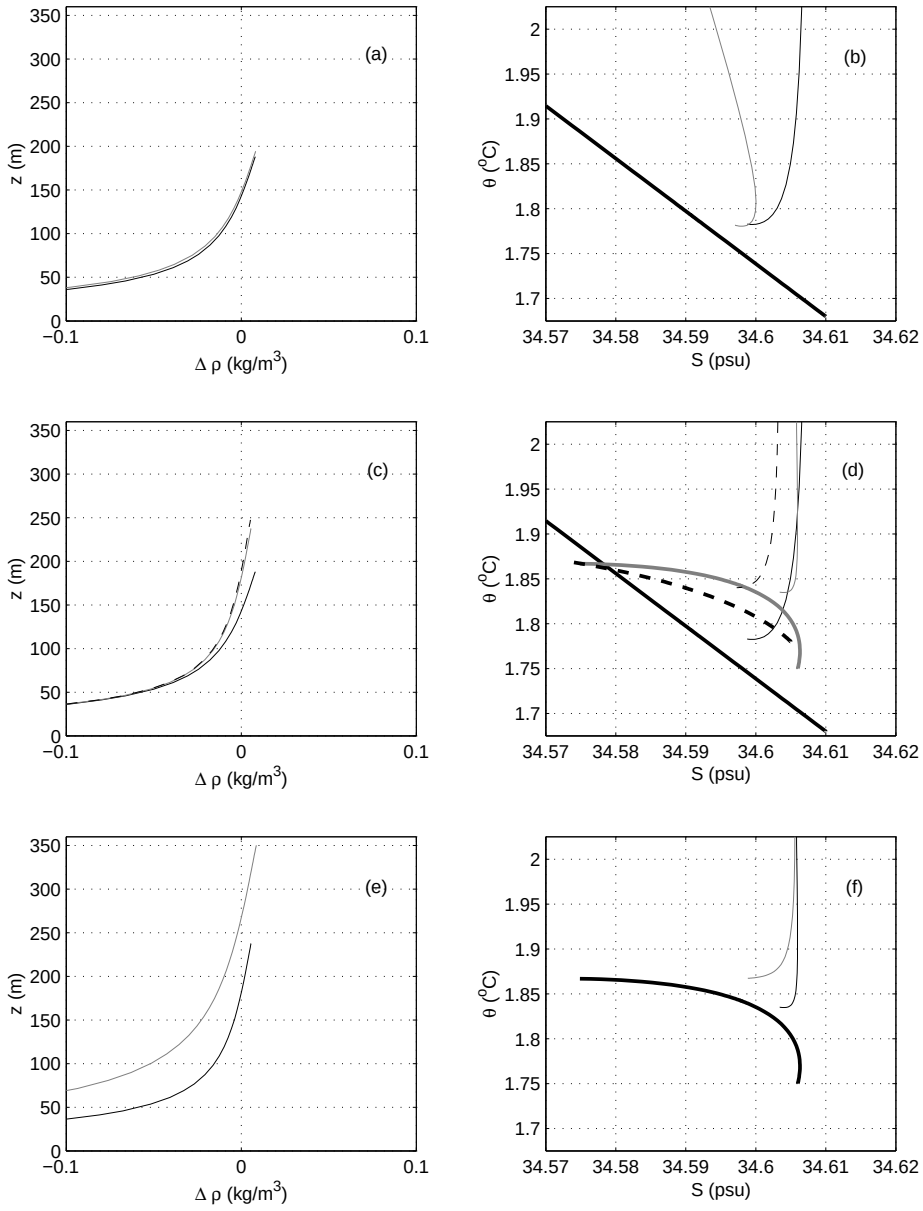

Figure 4.10: Sensitivity of the steady-plume model to the source salinity (a-b), case 1 (black) versus case 2 (gray); the background temperature/salinity profiles (c-d), case 1 (black) versus case 3 (gray) versus case 4 (dash); and the source heat flux (e-f), case 3 (black) versus case 5 (gray). The density difference between the plume and the background and the θ-S relation is plotted in the left and right panels, respectively. The thick lines denote background quantities.

the plumes sampled over High Rise (see casts 309u, 747u and 302u in figure 4.6) must stem from lower salinity sources, since the background itself never reaches the extreme low salinity values found in these plumes.

Finally, increasing the source heat flux elevates the rise height ($z^* \sim 350$ m), increases the overshooting to 100 m, and also leads to warmer water ($\theta \sim 1.87$) at the top of the plume (figure 4.10e, f). Based on this sensitivity study, the properties of the plume for case 5 are most similar to those observed in the MEF rising plume seen in figure 4.4i, suggesting that the heat flux of the vent from which the plume emanated, neglecting the effects of background flow, is closer to 50 MW rather than 10 MW. A value of 50 MW is more representative of the maximum heat flux for a single black smoker than the median value of 9 MW per vent measured by Bemis et al. (1993) in the MEF .

4.5 Quasi-synoptic velocity sections

In addition to the hydrographic and optical data, velocity data were collected simultaneously with an ADCP in the bottom 300 m of the water column during the along- and across-axis towyo surveys (except for the MEF survey in 2003, for which there is no velocity data). Figures 4.11a-f show transects of along- and across axis flow.

Tidal flows

The predominant temporal variability of the flow in this region is semidiurnal tidal. Because the towyo surveys took up to 8 hours to complete, the velocity transects do not provide a synoptic picture of along- and across-valley flow. This is especially evident in the sections corresponding to the longest surveys, 7a and 7b. As seen in the time-series of north-south velocity from an inverse barotropic tidal model (figure 4.2), towyo survey 7a (figure 4.11e) started at peak northward tide, went through slack tide half-way through the survey (cast 14, according to the model) and ended at peak southward tide. It should be noted that, while there is a reasonable correspon-

dence in the phasing of the north-south component from the tidal model and tidal predictions derived from actual measured velocities at 25 mab, the peak amplitudes do not necessarily agree (e.g. figure 2.5). Therefore, the times of slack/peak tides seen in the time-series are representative of actual tidal flows observed, but the absolute magnitudes at peak tides should be viewed with caution. Towyo survey 7b (figure 4.11f), going northbound from MEF to High Rise, started shortly after slack tide with increasing northward tidal flow that peaked in cast 35, according to the model, went to slack (cast 44) and ended with southward tidal flow.

Temporal variability also needs to be considered in viewing transects taken on the same track but at different phases of the tide. A clear example is the more synoptic across-axis towyo surveys taken over Clam Bed (figures 4.11a and c). Towyo survey 2 (middle panels in figure, in particular) coincided with a period of peaking northward flow in the tidal model (figure 4.2), whereas survey 4b was conducted under strong southward flow, a picture which corresponds quite well with the measured along- and across valley flow.

Plume-related flow above the ridge crest

At a distance from hydrothermal plumes, the flow is relatively uniform in the vertical, at least above the ridge. This is the case for the sections over Clam Bed mentioned above, and the south and central part of towyo survey 7b (figure 4.11f). In these sections, the tidal flow direction above the ridge is either northwest or southeast, consistent with the polarization of the M_2 tide in the region. Above the ridge crest, the strongest shears in velocity seem to be associated with plumes. For example, cross-valley flow in the cross-section over High Rise (figure 4.11b right column, middle panel) shows a convergent flow around a rising plume, and divergent flow above it, at the laterally spreading plume level. The strength of this convergence/divergence is $\Delta u/\Delta x \sim 10^{-3}\mathrm{s}^{-1}$. Another example is the flow feature seen in the middle of the across-valley velocity section for towyo survey 5 (figure 4.11d), that seems associated

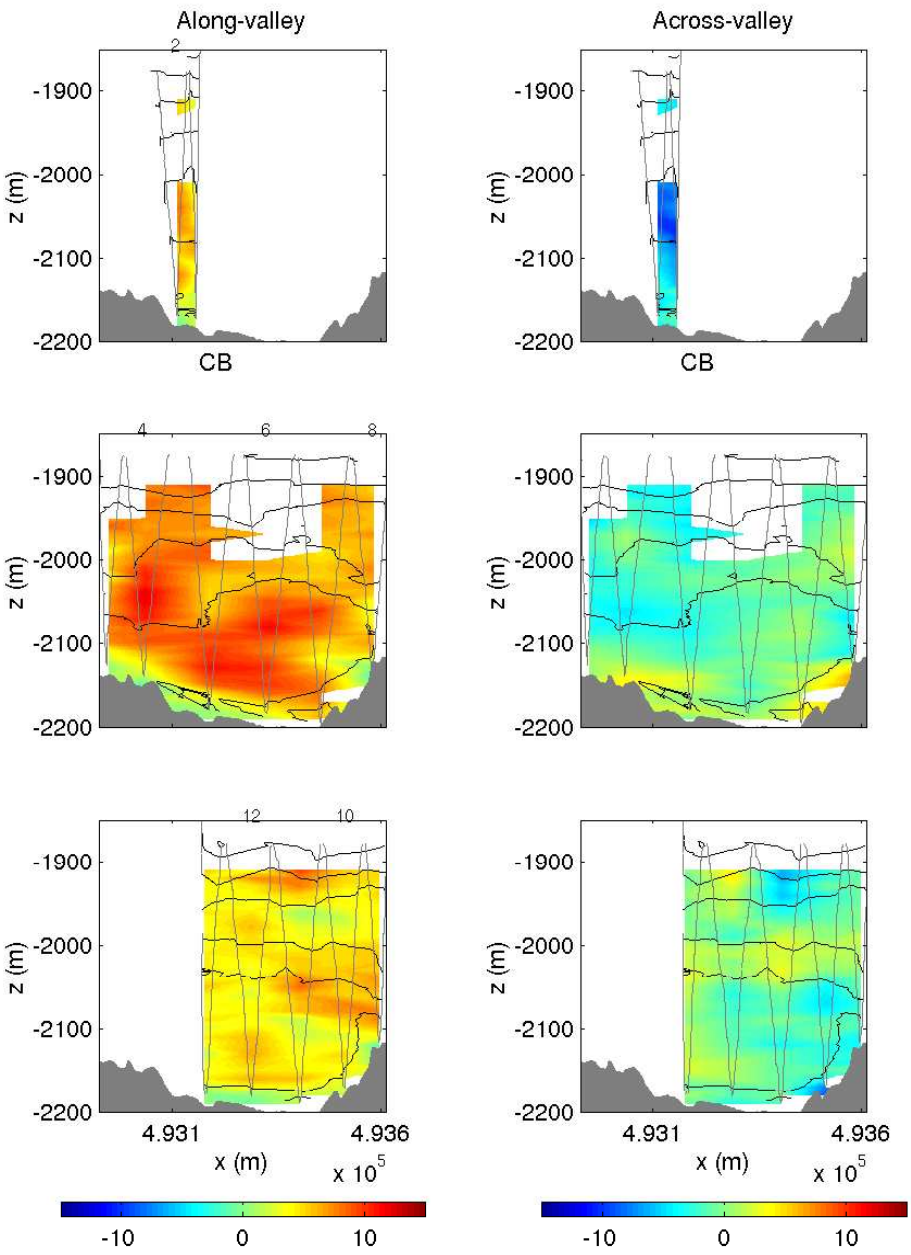

Figure 4.11a: Along- (left panels) and across-valley (right panels) velocity for towyo survey 2. The survey started over the center of the axial valley and headed westward (upper panels), crossed the valley eastbound (middle panels), and returned westbound to the point of origin (lower panels). Black contours correspond to the same sigma-2 surfaces as in figure 4.4a. The cast numbers for each down/upcast pair are specified at the top of the potential temperature sections. The location of Clam Bed is indicated in the upper panels.

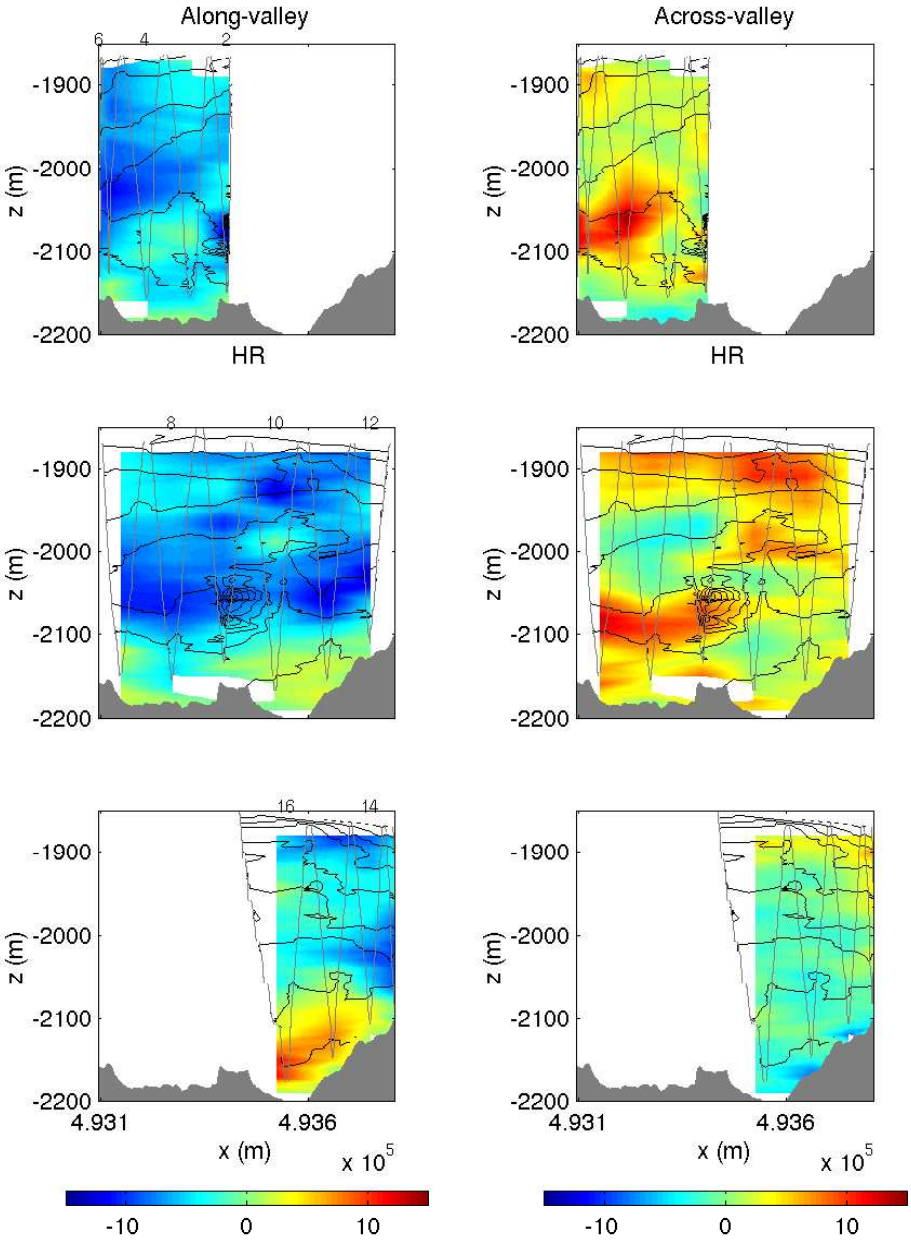

Figure 4.11b: Same as in figure 4.11a, but for towyo survey 3, over High Rise. The location of High Rise is indicated in the upper panels.

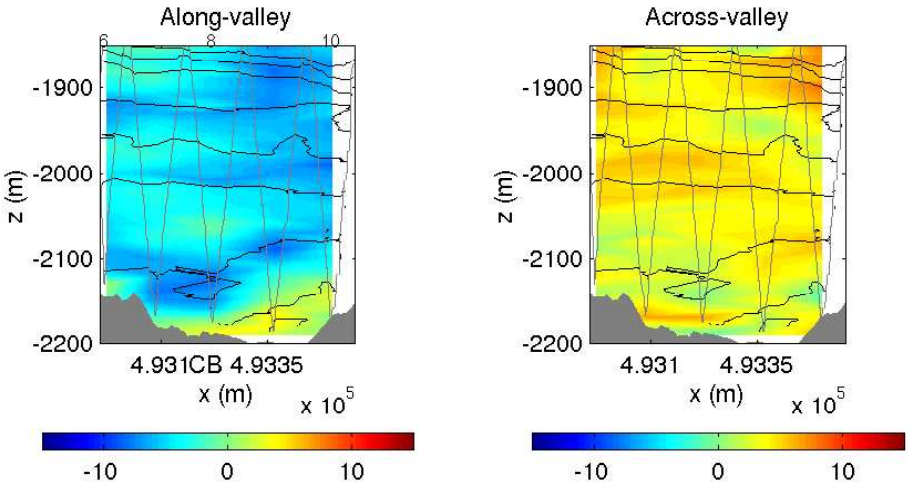

Figure 4.11c: Along- (left panel) and across-valley (right panel) velocity for towyo survey 4b across the valley eastbound over Clam Bed.

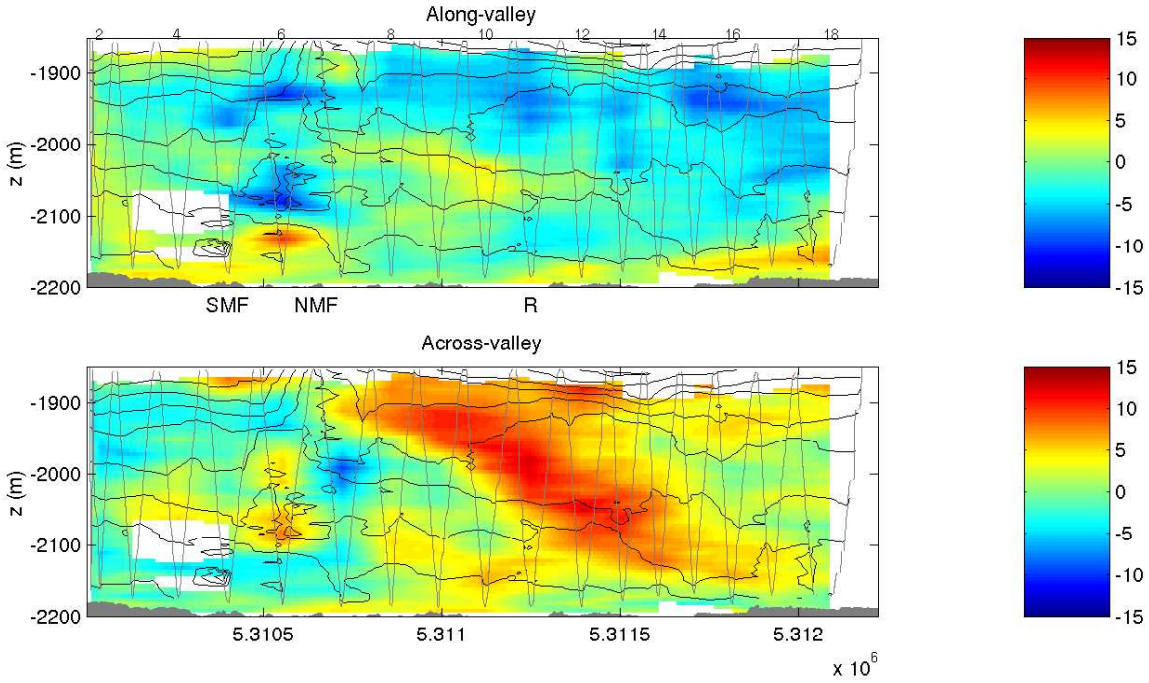

Figure 4.11d: Along- (upper panel) and across-valley (lower panel) velocity for towyo survey 5 northbound from MEF to Clam Bed. Location of fields are indicated in the top panel.

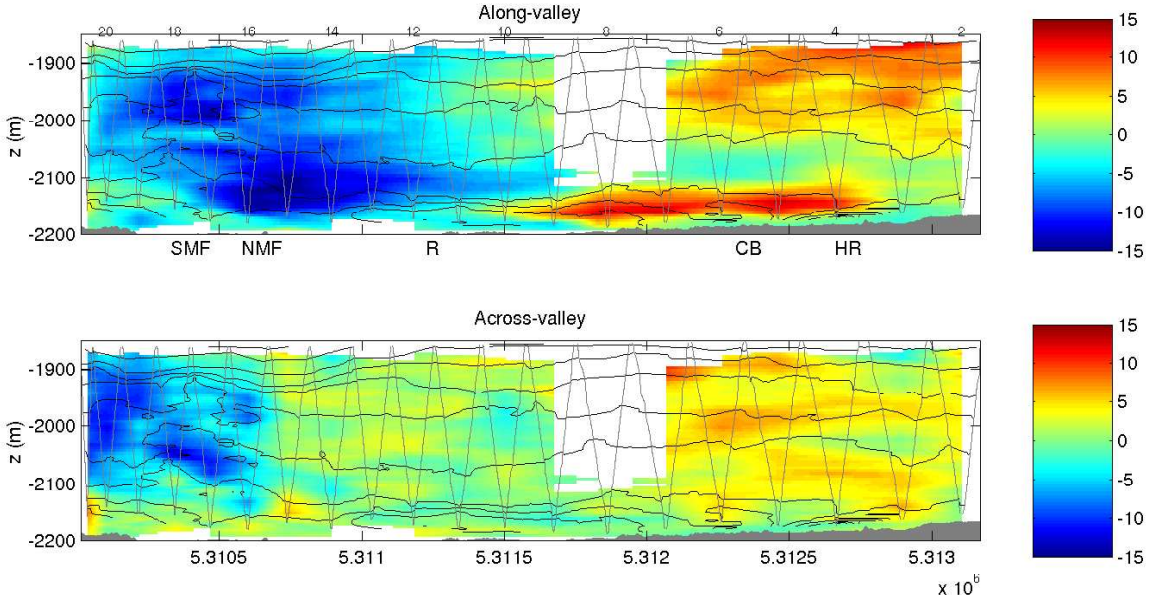

Figure 4.11e: Same as in figure 4.4d, but for towyo survey 7a southbound from High Rise to MEF.

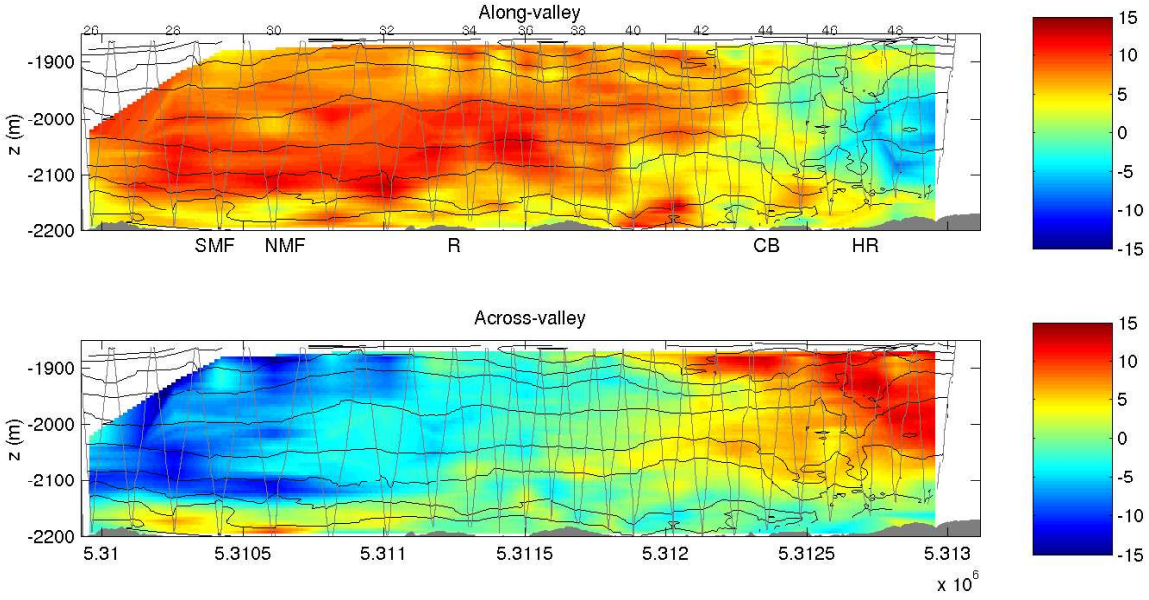

Figure 4.11f: Same as in figure 4.11d, but for towyo survey 7b northbound along a line on the eastern valley wall. The y-locations of the vent fields are indicated in the top panel.

with hydrothermal effluent observed in the tracer fields (figure 4.4j).

Especially noteworthy in this across-valley velocity section, is the strong cyclonic vorticity ($-\Delta u/\Delta y \sim 10^{-3}$ s^{-1}) around the rising plume over MEF. Theory of a buoyancy-forced baroclinic vortex predicts the development of a cyclonic circulation around the stem of the rising plume as absolute vorticity is stretched by the convergent, entrainment velocity (Speer, 1989). The horizontal scale for this cyclonic flow is given by $l_c = (B_o f^{-3})^{1/4}$ (Speer and Marshall, 1995). For the 50 MW source heat flux estimated for this plume (section 4.4), $l_c \sim 330$ m, which is consistent with the dimensions of the flow feature observed. If this is indeed a plume-induced cyclonic vortex, it is natural to wonder why such a feature is not observed in other sections with rising plumes. It is possible that other transects did not slice exactly through the middle of the rising plume (this would be the case for the High Rise plume in 7b and perhaps the MEF plume in 7a), that a strong background flow affected the spin-up of the cyclone (towyo 5 sampled the rising plume at slack) or that the cyclonic circulation had not yet fully developed (perhaps the case for the High Rise plume in towyo 3).

Regarding the anticyclonic circulation associated with the laterally spreading plume and plume vortices, there is a question of whether it can be distinguished from the tidal flow. The azimuthal flow in the vortex scales as fr, where r is the radius of the vortex (Speer and Marshall, 1995). This would yield velocities of ~ 5 cm/s for a 500 m radius that could be masked by strong tidal flows. Ideally, measurements of velocity in the vortex over several tidal periods would be necessary to average out the tides. Nevertheless, it is worth noting that the northwest/southeast polarization expected for the semidiurnal tidal flow above the ridge, and observed in other sections taken at a distance from vents, seems to be disrupted in towyo survey 7a (figure 4.11e). This could be related to the bolus of hydrothermal fluid present in the tracer fields. It is possible that if this feature is a vortex, its anticyclonic circulation would be counteracting the cross-valley tidal flows.

Flow in the valley

The flows observed in the ∼100-m deep axial valley are not always representative of flows above the ridge crest depth (-2100 m). In particular, two across-valley sections over High Rise and Clam Bed (surveys 3 and 4b, respectively) show southward tidal flow above the crest, but a strong northward flow on the eastern half of the valley (the section for towyo 2 over Clam Bed shows a strong, northward flow throughout the water column). The flow in the valley is associated with a strong across-valley density gradient, with denser water on the east. An analytical theory presented in Chapter 3 postulates that along-valley subinertial flows in the narrow axial valley are in geostrophic balance but the across-valley flows are not. Therefore the vertical shear in the along-valley flow should be in thermal-wind balance and can be estimated from the across-valley density gradient. Given the lateral density gradient observed in the section from towyo survey 3 (figure 4.4c), $\Delta\rho/\Delta x \sim 5 \times 10^{-3}$ kg m^{-3}/100 m, the geostrophic shear would be $\sim 5 \times 10^{-3}$ s^{-1}. This shear is consistent with the shear observed in the along-valley velocity transect for survey 3 (figure 4.11b, bottom panel). The vertical shear estimated from the record-mean velocity measured by the ADCP further south the valley (Figure 3.3) is $\sim 5 \times 10^{-3}$, one order of magnitude weaker; this could be related to a weaker cross-valley density gradient in the south (see for example the density section over the Main Endeavour Field, figure 4.4o). This apparent along-valley variation in vertical shear and cross-valley density gradients reiterates the three-dimensional nature of the circulation in the valley.

An interesting feature in the along-axis flow for towyo survey 7a (figure 4.11e) is the large positive velocity in the northern part of the valley (bottom 100 m) and strong shear above it, that is associated to a pronounced along-valley density gradient. This suggests that this flow is driven by the along-valley baroclinic pressure gradient resulting from the density structure.

4.6 Discussion

High-resolution hydrographic and velocity sections obtained using a towed CTD-LADCP package reveal a complex picture for flow in the hydrothermally-influenced layer within and above the axial valley of the Endeavour Segment of the Juan de Fuca Ridge. These observations confirm some previous notions of plume-driven circulation and flow within the valley, while also providing new insights.

At the resolution employed, sections of hydrography and tracer fields show a high degree of spatial variability (patchiness) crossing not only rising but also laterally spreading hydrothermal plumes. Temporal variability in this highly dynamic environment is apparent in repeated transects at different times and is in part related to plumes being wafted by the background flow, which is largely modulated by the semidiurnal tide. In the vertical, high-temperature effluent rises to and equilibrates at different levels depending on their buoyancy source, creating a series of thermohaline intrusions of varied thicknesses. Low-temperature effluent, which only rises a couple of tens of meters, is difficult to differentiate in these sections due to its small temperature anomaly and lack of particles, and because the survey extends to within 10 m off the bottom at most. The temporal and spatial variability of hydrothermal plumes, in particular in their rising phase, makes the measurement of their properties challenging, requiring high spatial resolution and repeated surveys.

Plume-driven flow is observable in the velocity sections by convergent flow and cyclonic vorticity around the stem of rising plumes and by lateral spreading and flow divergence, at the level of neutral buoyancy. The estimated plume-related cyclonic vorticity in towyo survey 5 (figure 4.11d) is $\sim 10^{-3}$ s^{-1}, about an order of magnitude larger than the Coriolis parameter. The plume vortex therefore has a Rossby number approaching 10 and its vorticity can be ascribed to along-valley shear in the cross-valley velocity. This quasi-synoptic, high-resolution observation of the plume vortex differs from the plume-driven flow measured at scales of 1 km from the source and over

a 3-month period by Joyce et al. (1998) in the southern Juan de Fuca Ridge, which is characterized by a Rossby number less than 0.1 and an along-valley flow sheared in the cross-valley direction. Because of the weak contribution of laterally sheared cross-valley flow in their vorticity estimation, these authors conclude that the flow observed was nearly two-dimensional, aligned along-valley and can best be described by a model for hydrothermal circulation driven by a line source of buoyancy aligned along-valley (Speer, 1989). The observations of plume driven circulation presented in this chapter show considerable variation in the along- and across-valley direction and thus are far from two-dimensional. Therefore, a more appropriate model for these fully three-dimensional flows would involve point rather than line sources of buoyancy and would allow for the influence of nonlinear, high Rossby number dynamics, in the vein of the numerical simulations of buoyant plumes by Speer and Marshall (1995) and Lavelle (1997).

A bolus of hydrothermal effluent suggestive of an anticyclonic plume vortex was observed on an along-valley hydrographic section through the middle of the valley. Anticyclonic plume vortices that form at the level of neutral buoyancy are part of a class of eddies known as submesoscale coherent vortices (SCVs) (D'Asaro et al., 1994), which are characterized by anomalously weak stratification, anticyclonic circulation, and water properties that are distinct and isolated from those of the surrounding water (McWilliams, 1985). Examples of SCVs include "meddies", vortices of Mediterranean water found in the Atlantic (e.g. Prater and Sanford, 1994), and megaplumes, lenses of large volumes of hydrothermal effluent that result from underwater volcanic eruptions (D'Asaro et al., 1994). A linear relation between the Burger and Rossby numbers of SCVs has been found experimentally and in observations (Hedstrom and Armi, 1988; D'Asaro et al., 1994). From the hydrography, the Burger number of the observed bolus is $N^2H^2/f^2L^2 \sim 1$, so if it were dynamically similar to an SVC it would follow that its Rossby number $Ro = 2V/(Lf) \sim 1$, yielding a plume vortex velocity $V \sim 5$ cm s^{-1}, consistent with the scaling discussed in section 4.5. Such a weak velocity would be

difficult to discern from the > 10 cm s^{-1} tidal flow measured at Endeavour Segment. These results suggest that, to adequately measure the velocity of an anticyclonic plume vortex of this size, filtering of the tidal flow would be necessary, which would involve the acquisition and averaging of multiple velocity sections taken at different phases of the tides.

On the inter-vent field scale, and within the axial valley, along-valley density gradients were observed, with denser water on the southern end of the valley. In analogy with the dynamics of the sea-breeze, Thomson et al. (2005) proposed that the northward flow observed in the valley could be driven by pressure gradients set up by variations in the density field caused by hydrothermal activity. In Chapter 4, it was shown that such northward flow, if subinertial, should also be accompanied by across-valley density gradients owing to the constraints of rotation and topography. Indeed, denser water was observed to the east of the valley, balancing a thermal wind shear that scales with the observed vertical shear in the along-valley flow. While this dynamical explanation for the northward mean flow is plausible, thermodynamic rationalizations for the cause of the along-valley density gradients are ambiguous.

Variations in buoyancy fluxes from different hydrothermal vent fields could give rise to lateral density gradients, with the less dense water being found over the vents with higher buoyancy output. With this simple thermodynamic model in mind, the stronger positive buoyancy anomalies (and presumably stronger buoyancy fluxes) observed near the High Rise versus Main Endeavour fields, would result in a southward density gradient, in the same direction as what is observed. Interestingly, the numerical simulations of flow at Endeavour Segment by Thomson et al. (2005) achieve a northward along-valley flow (presumably associated with a southward density gradient) with enhanced buoyancy fluxes at the southern rather than northern end of the valley. The key feature that may explain the along-valley density gradient in their model is the along-valley bottom slope in combination with vertical mixing driven by hydrothermal activity. In the deeper southern end, the hydrothermal plumes will

entrain denser water than in the north, resulting in a southward density gradient, despite the higher source heat fluxes implemented for the southern vent fields. If on the other hand, source buoyancy fluxes were larger in High Rise than in Main Endeavour, as the observations presented here suggest, it is possible that both the contrast in buoyancy fluxes and differential entrainment as described above, contribute to the measured southward density gradient.

Both near-bottom flows (whether tidally-driven or related to along-valley density gradients) and buoyant plumes have been implicated in the dispersal of vent organisms in their larval stage. Entrainment into the high temperature rising hydrothermal effluent and transport within the equilibrated plume or anticyclonic vortices at levels above the valley has been proposed as a larval dispersal mechanism (Kim et al., 1994). This is supported by observations of increased abundances of vent larvae in versus away from plumes (Mullineaux et al., 1995). Evidence of entrainment around rising plumes over Main Endeavour and High Rise is seen in the velocity sections presented here in the form of strong convergent flows. In addition, a lenticular feature retaining hydrothermal effluent observed in the hydrography along one of the sections could be a plume vortex. Plume-dispersal can be a long-range dispersal pathway as topographic barriers can be avoided and flows are largest above the ridge. On the other hand, episodes of cross-axis flows at these levels could displace the larvae off-axis (Mullineaux et al., 2002).

However, plume-dispersal is not essential for long-distance transport of larvae. This is the case for the densely populated Galapagos vents where no black smokers are found (Van Dover, 2000). The importance of near-bottom flows in larval dispersal has been emphasized by Kim and Mullineaux (1998) and in previous chapters, and further supported by the fact that the largest abundances of vent larvae are found close to the bottom (Mullineaux et al., 2005). In medium and slow spreading ridges in particular, axial valleys can constrain the larval transport and act as channels for dispersal. Thomson et al. (2003) have proposed a closed-cell circulation at the

Endeavour Segment where larvae would be taken northward within the valley and returned southward at levels above the ridge, thereby favoring colonization of vent communities at the segment scale. The velocity observations presented here suggest that, during southward tidal flow, the valley itself can be a two-way dispersal corridor, with northward flow on the east and southward flow on the west (see figure 4.11c). A similar flow pattern is seen in the model by Thomson et al. (2005) that can be ascribed to hydrothermal forcing alone as this model does not include tides. The advantage of a dispersal pathway within the valley is that it completely avoids the more risky levels above the ridge while maintaining a supply of larvae to the vent communities along the segment.

Chapter 5

CONCLUSIONS

This dissertation has examined, from a predominantly observational point of view, the flow and hydrography at the Endeavour Segment of the Juan de Fuca Ridge at vertical levels spanning the rise height of high temperature plumes down through the axial valley and into the bottom boundary layer.

5.1 Review of Chapter 2

Chapter 2 is concerned with the variability of currents and the turbulent fluxes of heat and momentum in the bottom boundary layer of the axial valley. To this end, point velocity and temperature data at 0.5 mab were collected near diffuse vents over periods of 4 days to 8 months and analyzed.

Within the bottom meter of the water column, the direction and magnitude of record-mean current and tidal ellipses show a very high degree of spatial heterogeneity owing to the influence of small-scale local topography and diffuse vents. Temporal variability occurs at a variety of expected periodicities, including tidal, inertial and 4-day variations. Semidiurnal tidal and 4-day frequencies coincide with the strongest peaks in velocity spectra. Diurnal tidal and, especially, inertial currents present a weaker variability, while nonlinear wave interactions, resulting in spectral peaks at the sum of the M_2 and inertial frequencies and at the second harmonic of the semidiurnal tide, are often significant.

The turbulent bottom boundary layer in regions of diffuse hydrothermal venting is quite different from a typical, stably stratified deep oceanic boundary layer. Turbulent kinetic energy budgets calculated from the data reveal that vertical shear of

the prevailing current and buoyancy both make significant contributions to the generation of turbulence. At most sites, modulation of the prevailing current by the semidiurnal tide creates a shifting balance between mechanical and buoyant production terms. Extreme bottom roughness of the fractured basalt seafloor and mounds of vent organisms, along with contributions from buoyancy, lead to very high values of friction velocity, and observed dissipation values that can reach levels found in highly turbulent estuarine regions.

The variability in currents and turbulent fields in the near-bottom boundary layer revealed by these measurements presents a highly dynamic environment for the vent organisms that reside there and for their larvae, which tend to be concentrated very near the seafloor. The vertical flux of larvae in the bottom boundary layer depends on processes that are tidally modulated like turbulent mixing or advection by buoyant plumes. Away from areas of hydrothermal activity where turbulence is exclusively mechanically generated, slack tide is a period of reduced mixing in which settling of larvae is potentially favored. Over areas of diffuse vents, however, buoyancy driven turbulence could compensate for the reduction of mechanical mixing during slack tide, making the upward transport of larvae less dependent on the tides. The horizontal currents that modulate these vertical fluxes also transport larvae directly. The high degree of spatial variability of these flows can translate into net displacements by virtue of tidal rectification. This near-bottom transport can also affect other aspects of the biology of vent organisms by regulating the delivery of nutrients or chemicals, while the enhanced near-bottom turbulence may play a role in feeding and reproduction.

5.2 Review of Chapter 3

Velocity measurements with high vertical resolution, and a two-dimensional inviscid linear quasianalytic model for subinertial oscillatory flows, were used to analyze the vertical structure of flow in the axial valley. At a site away from hydrothermal vents,

observed semidiurnal flows are independent of depth, rectilinear and parallel to the valley axis, while subinertial flows are intensified and re-aligned along-valley toward the bottom up until 20 mab. Within the bottom 20 m, a depth range consistent with the thickness of the turbulent Ekman layer estimated from bottom boundary layer friction velocities, the velocity decreases with depth. The flow structure outside of the Ekman layer is consistent with solutions from the inviscid model, which show attenuation of subinertial across-valley flow with depth. This cross-flow attenuation is most pronounced for valleys with widths less than the internal Rossby radius of deformation. Reduction of across-valley flow with depth results in a weakened Coriolis force that cannot fully balance the along-valley pressure-gradient force. The resulting force imbalance yields a directly accelerated bottom-intensified along-valley flow.

The importance of this physical process at other mid-ocean ridge valleys (and other concave submarine topographic features, in general) depends in part on their geometry. A factor that plays a major role in setting the geometry of median rift-valleys is the rate of spreading of the ridge, with faster rates yielding valleys with smoother topography. Therefore, one might expect that stagnation of cross-valley flow is weaker for ridges with faster spreading rates, such as the East Pacific Rise. However, the key dynamical parameter that sets the degree of stagnation is the ratio of valley width to Rossby radius, so that the ambient stratification and the latitude of the ridge must also be considered. These physics could in particular be at play in the large rift-valley of the Mid-Atlantic Ridge, at some distance from controlling sills.

If active, the mechanism described by the model provides a dynamic background environment for the axial valley to which hydrothermal venting and semidiurnal tides would add complexity. Indeed, a second flow measurement site in the axial valley located within an active hydrothermal vent field and adjacent to the axial valley wall exhibits a vertical structure that does not clearly resemble the model solution, suggesting that this record is dominated by other effects from the local steep and irregular topography and/or buoyant plumes. Additionally, the mechanism is specific

to subinertial flows and hence excludes the semidiurnal tidal motions that are highly energetic in the axial valley. Interaction of the barotropic semidiurnal tide with topography in a stratified fluid will drive internal tides. To help in interpreting the vertical and lateral variability in the observed semidiurnal tidal motions, it would be of interest to model internal tide generation within the axial valley. Numerical modeling studies of the internal tides have mainly focused on the generation of baroclinic tidal motions at convex submarine features such as ridges and seamounts (e.g. Holloway and Merrifield, 1999; Lavelle et al., 2004), Modeling the internal tides in the narrow concave axial valley has not been done and could be the topic of future research.

The strong vertical shears and spiraling flows observed within the axial valley for diurnal tidal and lower-frequency flows have important implications in the transport of hydrothermal vent fluid and the dispersal of larvae of vent organisms by bottom currents. The model solutions show that vertical shear in diurnal along-valley flow combined with vertical displacements near the valley walls result in a down-valley Stokes drift. While this drift is weaker than the observed record-mean along-valley flows, it can potentially contribute to dispersal of larvae since tides are a continuous forcing.

5.3 Review of Chapter 4

In Chapter 4, high resolution cross- and along-valley sections of flow and hydrography in the bottom 300 m were presented. The hydrographic sections reveal gradients in temperature, salinity and density gradients with colder, saltier, and denser water to the south and east. Coincident with the along-valley density gradient is a bottom-intensified, northward along-valley current. The vertical shear of this current scales with the thermal wind shear derived from the cross-valley density gradient, and the flow is aligned with the baroclinic pressure gradient associated with the along-valley density gradient, consistent with the model presented in Chapter 3. Both the density gradient and along-valley flow are observed in repeated sections taken at different

times. Given the fact that advection of density by the northward flow would tend to flatten isopycnals and eliminate the density gradient, the persistence of these features requires explanation. A similar down-gradient flow was observed in the rift valley of the Mid-Atlantic Ridge (Thurnherr et al., 2002). Using an inverse calculation based on the density equation, Thurnherr (2006) showed that enhanced vertical mixing provides a mechanism for balancing lateral advection in this region. Perhaps an analogous balance is found in the axial valley. Such mixing could also drive viscous forces that would tend to balance the baroclinic pressure gradient force. Alternatively, vertical advection of momentum, or lateral friction along the valley sidewalls could counteract the pressure gradient and maintain the steady state momentum balance necessary for the persistence of the along-valley current on long timescales.

Hydrothermal plumes in their rising, laterally spreading, and equilibrated stages are observed in the sections. Rising plumes are evidenced by density inversions, convergent flow surrounding their cores, and cyclonic vorticity of magnitude 10 times the Coriolis parameter. From the limited number of rising plumes that were detected in the towyo surveys over each vent field, it appears that plume source salinity and buoyancy anomalies vary from north to south, as plumes over the High Rise field are fresher and more buoyant than those over MEF. The most prominent plume from all the sections is found over MEF. The source heat flux for this plume is estimated to be 50 MW based on a sensitivity study using the Speer and Rona (1989) plume model. This value is at the upper limit of what has been measured at MEF black smokers (Bemis et al., 1993). Considerable temporal and spatial variability in the maximum vertical extent of the plumes is evident in repeated sections, and is likely caused by tidal advection and the inherent intermittency of the plumes themselves. Near the level of neutral buoyancy, thin layers of thermohaline intrusions with water mass properties characteristic of hydrothermal effluent are seen to emanate from regions of rising plumes. On a particular cross-valley section over High Rise, divergent flow is found on one of these layers, suggestive of active lateral spreading. Models for

hydrothermal plumes predict that during their equilibrated stage, this lateral spreading is arrested by rotation and an anticyclonic plume vortex filled with hydrothermal effluent forms (Speer, 1989; Helfrich and Battisti, 1991; Speer and Marshall, 1995). A bolus of hydrothermal effluent $\sim$ 1.5 km in diameter suggestive of such a plume vortex is observed on one of the sections. Whether this feature is truly a plume vortex is difficult to discern from velocity measurements due to the strong tidal motions that could have easily masked the relatively weak anticyclonic circulation thought to characterize a vortex of the same dimensions as the bolus.

5.4 Future work

Among the unresolved questions raised in this dissertation and that need further investigation are: what causes the along-valley density gradient, and, what forces balance the along-valley pressure gradient? Regarding the first question, two causes have been discussed in this thesis: one, differential entrainment associated with the sloping valley bottom and two, along-valley variations in the buoyancy output of the different vent fields. To assess the relative contributions of these two mechanisms, numerical experiments of an idealized axial valley heated from below (in the vein of Thomson et al. (2005)) could be performed with variable bottom slope and contrasting along-valley buoyancy inputs. These simulations could also be useful in addressing the second question regarding force balances. Terms in the momentum equations could be diagnosed from the numerics to see which processes (vertical mixing of momentum, lateral friction, bottom drag, or vertical advection of momentum) balances the baroclinic pressure gradient. Both of these questions could also be addressed observationally using microstructure measurements to estimate diapycnal mixing and frictional forces and then comparing these terms to the inferred lateral advection of density and pressure gradients, respectively.

Another important outstanding question that this thesis was not able to resolve, for lack of appropriate data, concerns the entrainment of low-temperature effluent

from diffuse sources into the high-temperature buoyant plumes. This question could be best approached by releasing tracers into the low-temperature effluent in the vicinity of a black smoker, followed by a systematic towyo survey of the associated high-temperature plume. A further issue that could be addressed with such a dye-release experiment relates to the predominance of dispersal within the valley by near-bottom currents or dispersal above the crest in the high-temperature plume. It would also be interesting to follow a water parcel originating from a diffuse hydrothermal vent patch located away from high temperature sources, for example, in Clam Bed, and ascertain the fate of this plume of low-temperature effluent.

This thesis has considered larvae as essentially passive particles at the mercy of the flows. Questions relating larvae dispersal should ultimately involve field work with sampling of actual organisms. One of the difficulties this presents is obtaining large enough biological samples for statistical significance at time intervals that are relevant to the physical processes that govern the hydrodynamics in the near-bottom of the axial valley; perhaps, optical larvae counters exist or will be developed to help overcome this problem. Although biological factors on larval dispersal cannot be disregarded, passive transport in water currents is often a good first-order approximation. The goal of this thesis has been to characterize flows in the near-bottom of the axial valley, an important region for the dispersal of larvae that tend to concentrate there. Much remains to be investigated, but this first incursion into the dynamics of near-bottom flows unveils a valley that, far from stagnant, is a rather complex and dynamic environment for the dispersal of larvae and diffuse hydrothermal fluid (and associated heat and chemicals) in general.

BIBLIOGRAPHY

Allen, S. E. and Thomson, R. E. (1993). Bottom-trapped subinertial motions over mid-ocean ridges in a stratified rotating fluid. *J. Phys. Oceanogr.*, 23:566–581.

Baker, E. T., Lavelle, J. W., Feely, R. A., Massoth, G. J., Walker, S. L., and Lupton, J. E. (1989). Episodic venting of hydrothermal fluids from the Juan de Fuca Ridge. *J. Geophys. Res.*, 94:9237–9250.

Baker, E. T. and Massoth, G. J. (1987). Characteristics of hydrothermal plumes from two vent fields on the Juan de Fuca Ridge, northeast Pacific Ocean. *Earth Planet. Sci. Lett.*, 85:59–73.

Bemis, K. G., Rona, P. A., Jackson, D., Jones, C., Silver, D., and Mitsuzawa, K. (2002). A comparison of black smoker hydrothermal plume behavior at Monolith vent and at Clam Acres vent field: Dependence on source configuration. *Marine Geophys. Res.*, 23:81–96.

Bemis, K. G., Von Herzen, R. P., and Mottl, M. J. (1993). Geothermal heat flux from hydrothermal plumes on the Juan de Fuca Ridge. *J. Geophys. Res.*, 98:6351–6365.

Brainerd, K. E. and Gregg, M. C. (1993). Diurnal restratification and turbulence in the oceanic surface mixed layer 2. Modeling. *J. Geophys. Res.*, 98:22657–22664.

Bryden, H. L. (1976). Horizontal advection of temperature for low-frequency motions. *Deep-Sea Res.*, 23:1165–1174.

Butman, C. A. (1996). Larval settlement of soft-sediment invertebrates: some predictions based on an analysis of near-bottom velocity profiles. In Nihoul, J. C. J., editor, *Marine interfaces ecohydrodynamics, Oceanography Series*, volume 42, pages 487–513. Elsevier.

Cannon, G. A. and Pashinski, D. J. (1990). Circulation near Axial Seamount. *J. Geophys. Res.*, 95:12,823–12,828.

Cannon, G. A. and Pashinski, D. J. (1997). Variations in mean currents affecting hydrothermal plumes on the Juan de Fuca Ridge. *J. Geophys. Res.*, 102:24965–24976.

Cannon, G. A., Pashinski, D. J., and Lemon, M. R. (1991). Middepth flow near hydrothermal venting sites. *J. Geophys. Res.*, 96:12,815–12,831.

Cannon, G. A. and Thomson, R. E. (1996). Characteristics of 4-day oscillations trapped by the Juan de Fuca Ridge. *Geophys. Res. Lett.*, 23:1613–1616.

Chelton, D. B., Esbensen, S. K., Schlax, M. G., Thum, N., Freilich, M. H., Wentz, F. J., Gentemann, C. L., McPhaden, M. J., and Schopf, P. S. (2001). Observations of coupling between surface wind stress and sea surface temperature in the eastern Tropical Pacific. *J. Climate*, 14:1479–1498.

Chevaldonne, P., Jovillet, D., Vangriesheim, A., and Desbruyeres, D. (1997). Hydrothermal-vent alvinellid polychaete dispersal in the eastern Pacific, 1. Influence of vent site distribution, bottom currents, and biological patterns. *Limnol. Oceanogr.*, 42:67–80.

Crimaldi, J. P., Thompson, J. K., Rosman, J. H., Lowe, R. J., and Koseff, J. R. (2002). Hydrodynamics of larval settlement: The influence of turbulent stress events at potential recruitment sites. *Limnol. Oceanogr.*, 47:1137–1151.

D'Asaro, E., Walker, S., and Baker, E. T. (1994). Structure of two hydrothermal megaplumes. *J. Geophys. Res.*, 99:20,361–20,373.

Delaney, J. R., Robigou, V., McDuff, R. E., and Tivey, M. K. (1992). Geology of a vigorous hydrothermal system on the Endeavour Segment, Juan de Fuca Ridge. *J. Geophys. Res.*, 97(19):19663–19682.

Dillon, T. M., Moum, J. N., Chereskin, T. K., and Caldwell, D. R. (1989). Zonal momentum balance at the equator. *J. Phys. Oceanogr.*, 19:561–570.

Dyer, A. J. (1974). A review of flux-profile relationships. *Boundary-Layer Meteorol.*, 7:363–372.

Egbert, G. D., Bennett, A., and Foreman, M. (1994). TOPEX/Poseidon tides estimated using a global inverse model. *J. Geophys. Res.*, 99:24821–24852.

Egbert, G. D. and Erofeeva, S. (2002). Efficient inverse modeling of barotropic ocean tides. *J. Atmos. Oceanic Technol.*, 19:183–204.

Emery, W. J. and Thomson, R. E. (1998). *Data analysis methods in physical oceanography*. Pergamon Elsevier Science, 1st edition. 634 pp.

Ferron, B., Mercier, H., Speer, K., Gargett, A., and Polzin, K. (1998). Mixing in the Romanche Fracture Zone. *J. Phys. Oceanogr.*, 28:1929–1945.

Finelli, C. M. and Wethey, D. S. (2003). Behavior of oyster (*Crassostrea virginica*) larvae in flume boundary layer flows. *Mar. Biol.*, 143:703–711.

Foreman, M. G. G. (1978). *Manual for tidal currents analysis and prediction. Pacific Marine Science Report 78-6.* Institute of Ocean Sciences, Sidney, BC. 70 pp.

Franks, S. E. R. (1992). *Temporal and spatial variability in the Endeavour Ridge neutrally buoyant hydrothermal plume: Patterns, forcing and biogeochemical implications.* PhD thesis, Oregon State University.

Fuchs, H. L., Mullineaux, L. S., and Solow, A. R. (2004). Sinking behavior of gastropod larvae (*Ilyanassa obsoleta*) in turbulence. *Limnol. Oceanogr.*, 49:1937–1948.

Garcia Berdeal, I., Hautala, S. L., Thomas, L. N., and Johnson, H. P. (2006). Vertical structure of time-dependent currents in a mid-ocean ridge axial valley. *Deep-Sea Res. I*, 53:367–386.

Gill, A. E. (1982). *Atmosphere-ocean dynamics.* Academic Press, Inc., San Diego. 662 pp.

Gonella, J. (1972). A rotary-component method for analyzing meteorological and oceanographic vector time series. *Deep-Sea Res.*, 19:833–846.

Grassle, J. P., Snelgrove, P. V. R., and Butman, C. A. (1993). Larval habitat choice in still water and flume flows by the opportunistic bivalve *Mulinia lateralis. Neth, J. of Sea Res.*, 30:33–44.

Gross, T. F. and Nowell, A. R. M. (1985). Spectral scaling in a tidal boundary layer. *J. Phys. Oceanogr.*, 15:496–508.

Gross, T. F., Werner, F. E., and Eckman, J. E. (1992). Numerical modeling of larval settlement in turbulent bottom boundary layers. *J. Mar. Res.*, 50:611–642.

Hadfield, M. G. and Koehl, M. A. R. (2004). Rapid behavioral responses of an invertebrate larvae to dissolved settlement. *Biol. Bull.*, 207:28–43.

Hautala, S. L. and Riser, S. C. (1993). A nonconservative β-spiral determination of the deep circulation in the eastern South Pacific. *J. Phys. Oceanogr.*, 23:1975–2000.

Hautala, S. L., Sprintall, J., Potemra, J. T., Chong, J. C., Pandoe, W., Bray, N., and Gani Ilahude, A. (2001). Velocity structure and transport of the Indonesian Throughflow in the major straits restricting flow into the Indian Ocean. *J. Geophys. Res.*, 106:19,527–19,546.

Hedstrom, K. and Armi, L. (1988). An experimental study of homogeneous lenses in a stratified rotating fluid. *J. Fluid Mech.*, 191:535–556.

Helfrich, K. R. and Battisti, T. (1991). Experiments on baroclinic vortex shedding from hydrothermal plumes. *J. Geophys. Res.*, 96:12,511–12,518.

Holloway, P. E. and Merrifield, M. A. (1999). Internal tide generation by seamounts, ridges and islands. *J. Geophys. Res.*, 104:25,937–25,951.

Johnson, H. P., Hautala, S. L., Tivey, M. A., Jones, C. D., Voight, J., Pruis, M., Garcia-Berdeal, I., Gilbert, L. A., Bjorklund, T., Fredericks, W., Holand, J., Tsurumi, M., Kurakawa, T., Nakamura, K., O'Connell, K., Thomas, L., Bolton, S., and Turner, J. (2002). Survey studies hydrothermal circulation on the northern Juan de Fuca Ridge. *Eos Trans. AGU*, 83(8):73–79.

Johnson, H. P. and Holmes, M. L. (1989). Evolution in plate tectonics: The Juan de Fuca Ridge. In Winterer, E. L., Hussong, D. M., and Decker, R. W., editors, *The geology of North America. The Eastern Pacific Ocean and Hawaii*, volume N, pages 73–91. Geol. Soc. of Am., Boulder, CO.

Joyce, T. M. (1989). On in situ "calibration" of shipboard ADCPs. *J. Atmos. Oceanic Technol.*, 6:169–172.

Joyce, T. M., Cannon, G. A., Pashinski, D., Helfrich, K. R., and Harrington, S. A. (1998). Vertical and temporal vorticity observations at Juan de Fuca Ridge: hydrothermal signatures. *Geophys. Res. Lett.*, 25:1741–1744.

Kelley, D. S., Baross, J. A., and Delaney, J. R. (2002). Volcanoes, fluids, and life at mid-ocean ridge spreading centers. *Annu. Rev. Earth Planet. Sci.*, 30:385–491.

Kim, S. L. and Mullineaux, L. S. (1998). Distribution and near-bottom transport of larvae and other plankton at hydrothermal vents. *Deep-Sea Res. II*, 45:423–440.

Kim, S. L., Mullineaux, L. S., and Helfrich, K. R. (1994). Larval dispersal via entrainment into hydrothermal vent plumes. *J. Geophys. Res.*, 99:12,655–12,665.

Koehl, M. A. R. and Powell, T. M. (1994). Turbulent transport of larvae near wave-swep rocky shores: Does water motion overwhelm larval sinking? In Wilson, W. H., Stricker, S. A., and Shinn, G. L., editors, *Reproduction and Development of Marine Invertebrates*, pages 261–274. The Johns Hopkins University Press, Baltimore, MD.

Large, W. G. and Pond, S. (1981). Open ocean momentum flux measurements in moderate to strong winds. *J. Phys. Oceanogr.*, 11:324–336.

Lavelle, J. W. (1997). Buoyancy-driven plumes in rotating, stratified cross flows: Plume dependence on rotation, turbulent mixing, and cross-flow strength. *J. Geophys. Res.*, 102:3405–3420.

Lavelle, J. W. and Cannon, G. A. (2001). On subinertial oscillations trapped by the Juan de Fuca Ridge, northeast Pacific. *J. Geophys. Res.*, 106:31,099–31,116.

Lavelle, J. W., Lozovatsky, I. D., and IV, D. C. S. (2004). Tidally induced turbulent mixing at Irving Seamount–Modeling and measurements. *Geophys. Res. Lett.*, 31. L10308, doi:10.1029/2004GL019706.

Lilley, M. D., Butterfield, D. A., Lupton, J. E., and Olson, E. J. (2003). Magmatic events can produce rapid changes in hydrothermal vent chemistry. *Nature*, 422:878–881.

Little, S. A., Stolzenbach, K. D., and Grassle, F. J. (1988). Tidal current effects on temperature in diffuse hydrothermal flow: Guaymas Basin. *Geophys. Res. Lett.*, 15:1491–1494.

Little, S. A., Stolzenbach, K. D., and Von Herzen, R. P. (1987). Measurements of plume flow from a hydrothermal vent field. *J. Geophys. Res.*, 92:2587–2596.

Lupton, J. E. (1995). Hydrothermal plumes: Near and far field. In Humphris, S. E., Zierenberg, R. A., Mullineaux, L. S., and Thomson, R. E., editors, *Seafloor Hydrothermal Systems: Physical, Chemical, Biological, and Geological Interactions*, pages 317–346. Washington, DC: American Geophysical Union.

Lupton, J. E., Delaney, J. R., Johnson, H. P., and Tivey, M. K. (1985). Entrainment and vertical transport of deep-ocean water by buoyant hydrothermal plumes. *Nature*, 316:621–623.

Mahrt, L., Vickers, D., Sun, J., Jensen, N. O., Jorgensen, H., Pardyjak, E., and Fernando, H. (2001). Determination of the surface drag coefficient. *Boundary-Layer Meteorol.*, 99:249–276.

Marsh, G. A., Mullineaux, L. S., Young, C. M., and Manahan, D. T. (2001). Larval dispersal potential of the tubeworm *Riftia pachyptila* at deep-sea hydrothermal vents. *Nature*, 411:77–80.

Marshall, J. and Schott, F. (1999). Open-ocean convection: observations, theory, and models. *Reviews of Geophysics*, 37:1–64.

McCreary, J. P. (1981). A linear stratified ocean model of the coastal undercurrent. *Phil. Trans. R. Soc. Lond. A*, 302:385–413.

McPhee, M. G. (1998). An inertial-disspation method for estimating turbulent flux in buoyancy-driven, convective boundary layers. *J. Geophys. Res.*, 103:3249–3255.

McPhee, M. G. and Stanton, T. P. (1996). Turbulence in the statically unstable oceanic boundary layer under Artic leads. *J. Geophys. Res.*, 101:6409–6428.

McWilliams, J. C. (1985). Submesoscale coherent vortices in the ocean. *Rev. Geophys.*, 23:165–182.

Metaxas, A. (2004). Spatial and temporal patterns in larval supply at hydrothermal vents in the northeast Pacific Ocean. *Limnol. Oceanogr.*, 49:1949–1956.

Mihaly, S. F., Thomson, R. E., and Rabinovich, A. B. (1998). Evidence for non-linear interaction between internal waves of inertial and semidiurnal frequency. *Geophys. Res. Lett.*, 25:1205–1208.

Morton, B. R., Taylor, G. I., and Turner, J. S. (1956). Turbulent gravitational convection from maintained and instantaneous sources. *Proc. R. Soc. Lond., Ser. A.*, 234:1–23.

Mullineaux, L. S. and France, S. C. (1995). Dispersal mechanisms of deep-sea hydrothermal vent fauna. In Humphris, S. E., Zierenberg, R. A., Mullineaux, L. S., and Thomson, R. E., editors, *Seafloor Hydrothermal Systems: Physical, Chemical, Biological, and Geological Interactions*, pages 408–424. Washington, DC: American Geophysical Union.

Mullineaux, L. S., Mills, S. W., Sweetman, A. K., Beaudreau, A. H., Metaxas, A., and Hunt, H. L. (2005). Vertical, lateral and temporal structure in larval distributions at hydrothermal vents. *Mar. Ecol. Prog. Ser.*, 293:1–16.

Mullineaux, L. S., Speer, K. G., Thurnherr, A. M., Maltrud, M. E., and Vangriesheim, A. (2002). Implications of cross-axis flow for larval dispersal along mid-ocean ridges. *Cah. Biol. Mar.*, 43:281–284.

Mullineaux, L. S., Wiebe, P. H., and Baker, E. T. (1995). Larvae of benthic invertebrates in hydrothermal vent plumes over Juan de Fuca Ridge. *Mar. Biol.*, 122:585–596.

Münchow, A., Coughran, C. S., Hendershott, M. C., and Winant, C. D. (1995). Performance and calibration of an Acoustic Doppler Current Profiler towed below the surface. *J. Atmos. Oceanic Technol.*, 12:435–444.

Pawlowicz, R., Beardsley, B., and Lentz, S. (2002). Classical tidal harmonic analysis including error estimates in MATLAB using TTIDE. *Computers and Geosciences*, 28:929–937.

Philander, S. G. (1990). *El Niño, La Niña, and the Southern Oscillation*. Academic Press, San Diego, CA.

Prater, M. D. and Sanford, T. B. (1994). A Meddy off Cape St. Vincent. Part I: Description. *J. Phys. Oceanogr.*, 24:1572–1586.

Pruis, M. J. (2004). *Energy and volume flux into the deep ocean: examining diffuse hydrothermal systems*. PhD thesis, University of Washington. http://www.nwra.com/resumes/pruis/pruis_dissertation_2004.pdf.

Pruis, M. J., Hautala, S. L., Garcia Berdeal, I., Johnson, H. P., and Bjorklund, T. (2006). Diffuse hydrothermal venting into the turbulent bottom boundary layer on Endeavour Segment, Juan de Fuca Ridge. I. The mean flux of heat from the upper crust. Submitted to Deep Sea Res. I.

Reidenbach, M. A., Monismith, S. G., Koseff, J. R., Yahel, G., and Genin, A. (2005). Boundary layer turbulence and flow structure over a fringing coral reef. *Limnol. Oceanogr.* Submitted.

Robigou, V., Delaney, J. R., and Stakes, D. S. (1993). Large massive sulfide deposits in a newly discovered active hydrothermal system, the High Rise field, Endeavour Segment, Juan de Fuca Ridge. *Geophys. Res. Lett.*, 20:1887–1890.

Robinson, I. S. (1981). Tidal vorticity and residual circulation. *Deep-Sea Res.*, 28:195–212.

Rona, P. and Trivett, A. (1992). Discrete and diffuse heat transfer at ASHES vent field, Axial Volcano, Juan de Fuca Ridge. *Earth Planet. Sci. Lett.*, 109:57–71.

Rona, P. A., Bemis, K. G., Silver, D., and Jones, C. D. (2002). Acoustic imaging, visualization, and quantification of buoyant hydrothermal plumes in the ocean. *Marine Geophys. Res.*, 23:147–168.

Rudnicki, M. D. and German, C. R. (2002). Temporal variability of the hydrothermal plume above the Kairei vent field, 25°S, Central Indian Ocean. *Geochem. Geophys. Geosyst.*, 3. doi:10.1029/2001GC000240.

Schmitt, R. W. (1999). Spice and the Demon. *Science*, 283:498–499.

Schott, F. and Stommel, H. (1978). Beta spirals and absolute velocities in different oceans. *Deep-Sea Res.*, 25:961–1010.

Skebo, K., Tunnicliffe, V., Garcia Berdeal, I., and Johnson, H. P. (2006). Spatial patterns of zooplankton and nekton in a hydrothermally active axial valley on Juan de Fuca Ridge. Deep Sea Res. I, in press.

Speer, K. G. (1989). A forced baroclinic vortex around a hydrothermal plume. *Geophys. Res. Lett.*, 16:461–464.

Speer, K. G. and Marshall, J. (1995). The growth of convective plumes at seafloor hot springs. *J. Mar. Res.*, 53:1025–1057.

Speer, K. G. and Rona, P. A. (1989). A model of an Atlantic and Pacific hydrothermal plume. *J. Geophys. Res.*, 94:6213–6220.

St. Laurent, L. C., M., T. J., and W., S. R. (2001). Buoyancy forcing by turbulence above rough topography in the abyssal Brazil Basin. *J. Phys. Oceanogr.*, 31:3476–3495.

Thomson, R. E., Delaney, J. R., McDuff, R. E., Janecky, D. R., and McClain, J. S. (1992). Physical characteristics of the Endeavour ridge hydrothermal plume during July 1988. *Earth Planet. Sci. Lett.*, 111:141–154.

Thomson, R. E., Mihaly, S. F., Rabinovich, A. B., McDuff, R. E., Veirs, S. R., and Stahr, F. R. (2003). Constrained circulation at Endeavour ridge facilitates colonization by vent larvae. *Nature*, 424:545–549.

Thomson, R. E., Roth, S. E., and Dymond, J. (1990). Near-inertial motions over a mid-ocean ridge: Effects of topography and hydrothermal plumes. *J. Geophys. Res.*, 95:7261–7278.

Thomson, R. E., Subbotina, M. M., and Anisimov, M. V. (2005). Numerical simulation of hydrothermal vent-induced circulation at Endeavour Ridge. *J. Geophys. Res.*, 110. C01004, doi:10.1029/2004JC002337.

Thurnherr, A. M. (2006). Diapycnal mixing associated with an overflow in a deep submarine canyon. *Deep-Sea Res. II*, 53:194–206.

Thurnherr, A. M. and Richards, K. J. (2001). Hydrography and high-temperature heat flux of the Rainbow hydrothermal site (36°14'N, Mid-Atlantic Ridge). *J. Geophys. Res.*, 106:9411–9426.

Thurnherr, A. M., Richards, K. J., German, C. R., Lane-Serff, G. F., and Speer, K. G. (2002). Flow and mixing in the rift valley of the Mid-Atlantic Ridge. *J. Phys. Ocean.*, 132:1763–1778.

Thwaites, F. T. and Williams, A. J. (1996). Development of a modular acoustic velocity sensor. *Proceedings of OCEANS 1996, MTS/IEEE/OES*, 2:607–612.

Thwaites, F. T. and Williams, A. J. (2001). BASS measurements of currents, waves, stress and turbulence in the North Sea bottom-boundary layer. *IEEE J. Oceanic Eng.*, 26:161–170.

Tivey, M. K., Bradley, A. M., Joyce, T. M., and Kadko, D. (2002). Insights into tide-related variability at seafloor hydrothermal vents from time-series temperature measurements. *Earth Planet. Sci. Lett.*, 202:693–707.

Tivey, M. K. and Delaney, J. R. (1985). Sulfide deposits from the Endeavour Segment. *Marine Mining*, 5:165–179.

Tivey, M. K. and Delaney, J. R. (1986). Growth of large sulfide structures on the Endeavour Segment of the Juan de Fuca ridge. *Earth Planet. Sci. Lett.*, 77:303–317.

Tomczak, M. and Godfrey, J. S. (1994). *Regional oceanography: An introduction.* Pergamon Elsevier Science, 1st edition. 422 pp.

Trivett, D. A. and Williams, A. J. (1994). Effluent from diffuse hydrothermal venting. 2. Measurements of plumes from diffuse hydrothermal vents at the southern Juan de Fuca Ridge. *J. Geophys. Res.*, 99:18417–18432.

Turner, J. S. (1973). *Buoyancy effects in fluids*. Cambridge University Press, New York. 367 pp.

Van Dover, C. L. (2000). *The ecology of deep-sea hysrothermal vents*. Princeton University Press. 424 pp.

Veirs, S. R. (2003). *Heat flux and hydrography at a submarine volcano: Observations and models of the Main Endeavour vent field in the northeast Pacific*. PhD thesis, University of Washington. http://www2.ocean.washington.edu/flowmow/pubs/srv-thesis.pdf.

Veirs, S. R., McDuff, R. E., Lilley, M. D., and Delaney, J. R. (1999). Locating hydrothermal vents by detecting buoyant, advected plumes. *J. Geophys. Res.*, 104:29239–29247.

Veirs, S. R., McDuff, R. E., and Stahr, F. R. (2006). Magnitude and variance of near-bottom horizontal heat flux at Main Endeavour hydrothermal vent field. *Geochem. Geophys. Geosyst.*, 7. Q02004, doi:10.1029/2005GC000952.

Veronis, G. (1972). On the properties of seawater defined by temperature, salinity and pressure. *J. Mar. Res.*, 30:227–255.

Wallace, J. M., Mitchell, T. P., and Deser, C. (1989). The influence of sea surface temperature on surface wind in the eastern equatorial Pacific: Seasonal and interannual variability. *J. Climate*, 2:1492–1499.

Wang, H. and Law, A. W. (2002). Second-order integral model for a round turbulent buoyant jet. *J. Fluid Mech.*, 459:397–428.

Weatherly, G. L., Blumsack, S., and Bird, A. A. (1980). On the effects of diurnal tidal currents in determining the thickness of the turbulent Ekman bottom boundary layer. *J. Phys. Oceanogr.*, 10:297–300.

Williams, A. J. (2001). Acoustic current meter zero offset drift. *Proceedings of OCEANS 2001, MTS/IEEE/OES*, 2:916–921.

Williams, A. J. (2002). Intercomparison of MAVS with VACM, VMCM, FSI 2-D, and Aanderaa RCM 11 current meters from a mooring. *Proceedings of OCEANS 2002, MTS/IEEE/OES*, 2:730–735.

Yu, X. and McPhaden, M. J. (1999). Dynamical analysis of seasonal and interannual variability in the Equatorial Pacific. *J. Phys. Oceanogr.*, 29:2350–2369.

Zimmerman, J. T. F. (1980). Vorticity transfer by tidal currents over an irregular topography. *J. Mar. Res.*, 38:601–630.

Appendix A

MAVS HEADING CORRECTION

Table A.1: Heading corrections for the MAVS deployments

S/N	Depl.	Year	Heading MAVS	Heading JASON	Offset
10054	MF1	2000	237	243[b]	-6
10051	B1	2000	348	350[b]	-2
10058	MF2	2000	101	121[b]	-20*
10055	MF3	2000	055	055[b]	0
10064	MF4	2000	143[b] 139[c]	160[b] 160[c]	-17*
10060	MF5	2000	122[b] 121[c]	140[c]	-19*
10048	MF6	2000/1	082	093[b] 091[c]	-11
10047	B2	2000/1	168[b] 155[c]	165[b] 155[c]	0
10063	CB1	2000/1	180[b] 186[c]	206[b] 180[c]	6
10057	CB2	2000/1	354[b] 004[c]	006[b] 012[c]	-12,-8
10062	CB3	2000/1	322[b] 326[c]	343[b] 339[c]	-21*,-13
10052	CB4	2000/1	155[b] 158[c]	147[b] 156[c]	8,2
10058	CB5	2001	232[b] 233[c]	260[b]	-28*
10050	CB6	2001	234[b] 237[c]	225[b]	9
10063	CB7	2001	147[b] 149[c]	$\sim$ 160[d]	-12
10049	CB8	2001	326[b,e]	010[b]	-44*
10056	HR1	2001	318[b] 311[c]	330[b]	-12
10055	CB9	2001	244[b] 236[c]	284[b]	-40*
10054	MF7	2001	055[b,e]	060[b]	-5
10053	MF8	2001	129[b,e]	141[b]	-12
10059	B3	2001	197[b] 195[c]	210[b]	-13
10060	R1	2001	032	090[b]	-58*
10065	R2	2001	103[b] 101[c]	114[b]	-11
10050	HR2	2001	120[b] 118[c]	138[b] 135[c]	-17*
10057	HR3	2001	258[b] 255[c]	253[b]	5
10061	MF9	2001/2	084	135[b]	-51*
10058	R3	2001/2	043	065[b]	-22*
10058	MF10	2001/2	119	163[b]	-44*
10054	CV	2002	321	285[d]	35*
10050	MF11	2002	164	N/A**	
10059	MF12	2002	131	090-100[d]	35*
10055	MF13	2002/3	178	191[c]	-17*
10060	MF14	2003	173	176[b]	-3

[a]From cruise log except where otherwise noted; [b]beginning of deployment; [c]end of deployment; [d]from frame grabs; [e]fell during deployment; *heading corrected; **heading consistent with what is seen in framegrabs

Appendix B

SOLUTION METHOD OF QUASIANALYTIC MODEL

Equation 3.9 was solved by transforming to a coordinate system that follows the topography, i.e. $(x, z) \rightarrow (x, \sigma(x, z))$ with $\sigma = z/h$, and results in the following governing equation for the streamfunction

$$\left[\frac{(f^2-\omega^2)}{h^2} + \frac{N^2\sigma^2}{h^2}\left(\frac{dh}{dx}\right)^2\right]\frac{\partial^2\psi}{\partial\sigma^2} + N^2\frac{\partial^2\psi}{\partial x^2} - 2N^2\left(\frac{\sigma}{h}\frac{dh}{dx}\right)\frac{\partial^2\psi}{\partial x\partial\sigma}$$
$$+ \quad N^2\frac{\sigma}{h}\left[\frac{2}{h}\left(\frac{dh}{dx}\right)^2 - \frac{d^2h}{dx^2}\right]\frac{\partial\psi}{\partial\sigma} = 0. \tag{B.1}$$

In making this coordinate transformation, the bottom boundary condition (3.10) is greatly simplified

$$\psi = U\delta h \quad \text{at} \quad \sigma = -1, \tag{B.2}$$

where $\delta h = h(x) - H$; the upper boundary condition remains the same, $\psi = 0$ at $\sigma = 0$. The form of the topography and the bottom boundary condition (B.2) set the lateral boundary conditions. Far from the ridge or valley, $\delta h \rightarrow 0$, so that $\psi \rightarrow 0$ as $x \rightarrow \pm\infty$.

In this coordinate system, the problem is amenable to numerical solution using finite-differencing. Discretizing (B.1) on a grid in (x, σ) space converts the differential equation to a matrix equation

$$\mathbf{A}\boldsymbol{\psi} = \mathbf{b}, \tag{B.3}$$

where the elements of $\mathbf{A}$ that act on grid points on the boundary are equal to one and otherwise are the second-order finite-difference approximation to the differential operator that acts on ψ in (B.1), $\boldsymbol{\psi}$ is the gridded and vectorized streamfunction, and $\mathbf{b}$ is a vector that contains boundary condition information for elements on the

boundary and is zero for all other elements. The width L_x of the domain for the numerical calculation is finite, i.e. $-L_x/2 < x < L_x/2$, but is chosen such that $\delta h|_{x=\pm L_x/2} \ll \max|\delta h|$, so that the lateral boundary conditions on the streamfunction can be approximated as $\psi = 0$ at $x = \pm L_x/2$. The matrix equation (B.3) was solved using a MATLAB algorithm that employs a minimum residual iterative method.

CURRICULUM VITAE
IRENE GARCIA BERDEAL

EDUCATION

Ph.D. University of Washington 2006

Physical Oceanography

Advisor: Susan L. Hautala

M.S. University of Washington 2000

Physical Oceanography

Advisors: Barbara M. Hickey and Mitsuhiro Kawase

B.S. Universidad de Cadiz, Spain 1996

Oceanography

RESEARCH INTERESTS

Influence of hydrodynamics on the dispersal of marine organisms, biophysical interactions, coastal oceanography, coastal ocean buoyant discharges, hydrothermal plumes, hydrothermal vents, flow-topography interaction.

HONORS

1997-1999 Graduate fellowship, Fundacion Barrie, A Coruña, Spain

PUBLICATIONS

Garcia Berdeal, I., S. L. Hautala, L. N. Thomas and H. P. Johnson, 2006. Vertical structure of time-dependent currents in a mid-ocean ridge axial valley, *Deep Sea Sea Research I*, 53:367-386.

Garcia Berdeal, I., B. M. Hickey and M. Kawase, 2002. Influence of wind stress and ambient flow on a high discharge river plume, *J. Geophys. Res.* 107(C9),3130, doi:10.1029/2001JC000932.